

University of Alberta

DIELECTROPHORETIC MEMBRANE FILTRATION

BY

Shahnawaz H. Molla



A thesis submitted to the Faculty of Graduate Studies and Research in partial fulfillment of the requirements for the degree of **Master of Science**.

Department of Mechanical Engineering

Edmonton, Alberta
Fall 2004



Library and
Archives Canada

Bibliothèque et
Archives Canada

Published Heritage
Branch

Direction du
Patrimoine de l'édition

395 Wellington Street
Ottawa ON K1A 0N4
Canada

395, rue Wellington
Ottawa ON K1A 0N4
Canada

Your file *Votre référence*

ISBN: 0-612-95818-3

Our file *Notre référence*

ISBN: 0-612-95818-3

The author has granted a non-exclusive license allowing the Library and Archives Canada to reproduce, loan, distribute or sell copies of this thesis in microform, paper or electronic formats.

L'auteur a accordé une licence non exclusive permettant à la Bibliothèque et Archives Canada de reproduire, prêter, distribuer ou vendre des copies de cette thèse sous la forme de microfiche/film, de reproduction sur papier ou sur format électronique.

The author retains ownership of the copyright in this thesis. Neither the thesis nor substantial extracts from it may be printed or otherwise reproduced without the author's permission.

L'auteur conserve la propriété du droit d'auteur qui protège cette thèse. Ni la thèse ni des extraits substantiels de celle-ci ne doivent être imprimés ou autrement reproduits sans son autorisation.

In compliance with the Canadian Privacy Act some supporting forms may have been removed from this thesis.

Conformément à la loi canadienne sur la protection de la vie privée, quelques formulaires secondaires ont été enlevés de cette thèse.

While these forms may be included in the document page count, their removal does not represent any loss of content from the thesis.

Bien que ces formulaires aient inclus dans la pagination, il n'y aura aucun contenu manquant.

Canada

To my parents.

Acknowledgements

I would like to take this opportunity to express my gratitude to my supervisor Dr. Subir Bhattacharjee who has been a constant source of inspiration and support under all circumstances, specially for the enormous amount of time he had spent with me explaining the physics behind the problem. I am also grateful for the encouragements and help I have received from everyone in our research group at times when I could not see the light at the end of the tunnel. Special thanks to Prodip for his help with the thesis and Noor for his patient hearing. I am grateful to Dr. Jacob Masliyah and Dr. Geza Szabo for providing the stable emulsions for the experiments. Finally, I would like to thank the great people in the machine shop and the Nanofab who helped with their guidance and experience to develop the experimental setup.

Edmonton, Alberta
August 6, 2004

Shahnawaz H. Molla

Table of Contents

1	Introduction	1
1.1	Background and Overview	1
1.2	Objectives and Scope	2
1.3	Organization of the Thesis	3
2	Dielectrophoresis	5
2.1	Introduction	5
2.2	Governing Principles of AC Dielectrophoresis	7
2.2.1	Electrical forces on particles and fluids	7
2.2.2	Induced dipole	9
2.2.3	Positive and negative dielectrophoresis	10
2.2.4	Effective dipole of particles	11
2.2.5	Dielectrophoresis in an AC field	16
2.2.6	Dielectrophoresis on parallel electrode array	18
2.3	Dielectrophoretic Force Calculation: Analytic Approach	19
2.3.1	Electric field evaluation	20
2.3.2	Force calculation	25
2.4	Results for Electric Field and Dielectrophoretic Force Calculation	27
2.4.1	Electric field and gradients of field intensity	27
2.4.2	Dielectrophoretic force field	28
2.5	Dielectrophoretic Force Calculation: Finite Element Analysis . .	31
2.5.1	Finite element formulation	31
2.5.2	Model description	32
2.5.3	Discretization	33
2.5.4	Finite element solution	35
2.5.5	DEP force estimation and convergence	35
2.6	Summary	38

3	Trajectory Analysis of Crossflow Membrane Filtration	57
3.1	Introduction	57
3.2	Model Description	59
3.3	Trajectory Analysis	60
3.4	Fluid Velocity Field in Crossflow Filtration	64
3.4.1	Crossflow filtration with uniform suction at membrane	65
3.4.2	Velocity components for intermittently permeable membrane	66
3.4.3	Fluid velocity profiles	70
3.5	Trajectory in Dielectrophoretic Membrane Filtration	71
3.5.1	Particle trajectories under uniform suction	72
3.5.2	Particle trajectories under intermittent suction	73
3.6	Summary	74
4	Dielectrophoretic Filtration in Water-in-Oil System	82
4.1	System Description	83
4.2	Simulation Results	85
4.2.1	Droplet migration in an impermeable wall channel	85
4.2.2	Droplet migration during dielectrophoretic membrane filtration	88
4.3	Theoretical Effectiveness	89
4.4	Summary	91
5	Dielectrophoresis in Membrane Fouling Prevention	100
5.1	System Description	102
5.2	Effect of Dielectrophoresis in Fouling Reduction	103
5.3	Implications on Membrane Fouling	105
5.4	Summary	105
6	Experimental Observation	110
6.1	Experimental Setup	111
6.1.1	Crossflow channel	111
6.1.2	Water-in-Heptane emulsion	112
6.2	Electrode Array Fabrication	112
6.2.1	Mask preparation	113
6.2.2	Photolithography	113

6.3	Experimental Procedure	114
6.4	Observation	115
6.5	Relation to Model Prediction	117
6.6	Summary	117
7	Conclusion and Future Work	122
7.1	Concluding Remarks	122
7.2	Future Work	123
	Bibliography	126
	Appendix	135
A		135

List of Figures

2.1	Schematic diagram showing the movement of a charged body (small sphere) and a polarized neutral body (large sphere) in a non-uniform electric field. The dotted lines represent the electric field lines.	39
2.2	(a) Electric field lines around a particle with polarizability higher than the surrounding medium. (b) Electric field lines around a particle with polarizability lower than the surrounding medium.	40
2.3	Schematic diagram showing a dipole in a uniform electric field. F^+ and F^- represent the electrical force acting on the charges due to the electric field.	41
2.4	Schematic diagram showing a dielectric medium with a permittivity, ϵ , under an electric field.	42
2.5	Plot of real part of frequency dependent Clausius-Mossotti factor for latex-in-water system against frequency of the applied ac signal. ϵ_p^* and ϵ_m^* represent the complex permittivity of particles and surrounding medium, respectively. The electrical properties of the particle and medium are listed in table A1 in the appendix.	43
2.6	Schematic diagram of interdigitated electrode array with the region of interest marked by dotted line.	44
2.7	Schematic diagram of applied potential distribution on the electrode plane for stationary wave DEP.	45
2.8	Schematic diagram showing the coordinates and the electrode configuration. a_j and b_j are the leading and trailing edge of the j^{th} electrode. λ_k is the midpoint of k^{th} pair of electrode.	46

2.9	(a) Surface plot showing the electric field gradient in the horizontal direction over the electrode plane. The horizontal and vertical axes in this plot are non-dimensionalized with respect to electrode width, which is $50 \mu\text{m}$ in this case. In this electrode configuration, gap between two consecutive electrodes is equal to the width of each electrode. Applied voltage, $V = 50 \text{ V}$ and frequency, $\omega = 600 \text{ Hz}$. (b) Surface plot showing the electric field gradient in the vertical direction over the electrode plane under same conditions as in the previous case.	47
2.10	Dependence of total DEP force on applied frequency. The horizontal axis in this plot is non-dimensionalized with respect to electrode width, which is $50 \mu\text{m}$ in this case. Gap between electrodes is equal to electrode width. Applied voltage, $V = 50 \text{ V}$	48
2.11	DEP force distribution over the electrode plane. The horizontal and vertical axes in this plot are non-dimensionalized with respect to electrode width, which is $50 \mu\text{m}$ in this case. Gap between electrodes is equal to electrode width. Applied voltage, $V = 50 \text{ V}$ and frequency, $\omega = 600 \text{ Hz}$. The DEP force is non-dimensionalized with respect to electrode width, Boltzmann constant and temperature, <i>i.e.</i> , the non-dimensional force is $F_{DEP}W/kT$	49
2.12	Variation of total DEP force with distance from the electrode plane at different axial locations. The horizontal axis in this plot is non-dimensionalized with respect to electrode width, which is $50 \mu\text{m}$. Gap between electrodes is equal to electrode width. Applied voltage, $V = 50 \text{ V}$ and frequency, $\omega = 600 \text{ Hz}$	50
2.13	Plot showing the dependence of total DEP force near the electrode plane (at $1 \mu\text{m}$ from the electrode plane) on applied voltage. The horizontal axis in this plot is non-dimensionalized with respect to electrode width, ($50 \mu\text{m}$). Gap between electrodes is equal to electrode width. Applied voltage, V varies from 50 V to 250 V . Applied frequency, $\omega = 600 \text{ Hz}$	51

- 2.14 Schematic diagram of the finite element model with boundary conditions. A representative segment of the electrode array is shown here. W and G are the width of the electrodes and gap between two consecutive electrodes on the parallel electrode array, respectively. ϕ is the applied electric potential on different parts of the boundary. $|\phi| = 1$ is scaled potential applied to the electrode surface, scaled with respect to V_0 , amplitude of the applied ac signal. All the lengths are scaled with respect to electrode width (W) and the gap (G) between electrodes is assumed to be equal to the width of electrode. 52
- 2.15 Plot showing norm of total DEP force with variation of number of elements used in the finite element analysis. DEP force evaluation was performed for a geometry shown in Figure 2.14. Norm was calculated over a periodic segment of the electrode array and averaged over 1600 data points evenly distributed on the segment. For each element specification, norm is defined as $(1/N) \sum (1 - F_{num}/F_{anal})^2$, where, N is the number of data points, F_{num} is the numerical value of the DEP force and F_{anal} is the analytic solution at each of the N points on the segment. The analysis was done for a latex-in-water system with applied voltage of 50 V and frequency of 600 Hz. The electrode width and gap are equal to 50 μm 53
- 2.16 Comparison of non-dimensional electric field values from analytic approach and numerical solution. The horizontal axis is non-dimensionalized with respect to electrode width (W) and the non-dimensional electric field is obtained by multiplying actual field values with a factor W/V_0 , where W is the width of each electrode in the array and V_0 is the amplitude of the applied voltage. Electrode width and gap equal to 50 μm and the applied voltage is 50 V at a frequency of 600 Hz. 54

2.17a	Comparison of total positive DEP force values from analytic approach and numerical solution in latex-in-water system. The horizontal axis is nondimensionalized with respect to electrode width (W) and vertical axis contains the actual DEP force values. Electrode width and gap equal to $50\ \mu\text{m}$ and the applied voltage is $50\ \text{V}$ at a frequency of $10\ \text{Hz}$ that corresponds to the positive value of the real part of frequency dependent Clausius-Mossotti factor for latex-in-water system.	55
2.17b	Comparison of total negative DEP force values from analytic approach and numerical solution in latex-in-water system. The horizontal axis is nondimensionalized with respect to electrode width (W) and vertical axis contains the actual DEP force values. Electrode width and gap equal to $50\ \mu\text{m}$ and the applied voltage is $50\ \text{V}$ at a frequency of $600\ \text{Hz}$ that corresponds to the negative value of the real part of frequency dependent Clausius-Mossotti factor for latex-in-water system.	56
3.1	Schematic diagram showing the conceptual picture of the proposed system for dielectrophoretic membrane filtration. $2H$ represents the total height of the channel. \bar{V}_x and V_w are average crossflow velocity in the channel and suction velocity on the membrane, respectively.	75
3.2	Surface plot of velocity component in vertical direction near the permeable surface of the channel with wall suction applied intermittently on the bottom wall. The plot shows the finite element solution obtained over a small representative section of the channel. Both the axes are nondimensionalized with respect to electrode width (W). The baseline of the geometry consists of 5 electrodes and 4 gaps in between. Width of electrodes and gaps are both $50\ \mu\text{m}$. The wall suction applied in the gap region is $10^{-5}\ \text{m/s}$ and average crossflow velocity is $10^{-3}\ \text{m/s}$ at the entrance of the channel.	76

3.3	Distribution of fluid velocity component in vertical direction at different horizontal planes, near the permeable surface of the channel with wall suction applied intermittently in the gap region. All the conditions remain same as in Figure 3.2. Horizontal axis is nondimensionalized with respect to electrode width (W), in the vertical axis the actual velocity is scaled with respect to maximum wall suction, $V_w = 10^{-5}$ m/s.	77
3.4	Trajectory of a particle in latex-in-water system under different conditions, namely, positive DEP, negative DEP and in the absence of DEP force. Both axes are nondimensionalized with respect to electrode width (W). The wall suction is uniform in all three cases, $V_w = 10^{-5}$ m/s and average crossflow velocity is 10^{-3} m/s. All other parameters are same as in table A1.	78
3.5	Trajectory of a particle in latex-in-water system under different conditions, namely, positive DEP, negative DEP and in the absence of DEP force. Both axes are nondimensionalized with respect to electrode width (W). The wall suction is intermittent in all three cases, $V_w = 10^{-5}$ m/s and average crossflow velocity is 10^{-3} m/s. All other parameters are same as in table A1.	79
3.6	Trajectory of a particle in latex-in-water system under positive DEP, with uniform and intermittent wall suction. Both axes are nondimensionalized with respect to electrode width (W). The average crossflow velocity and maximum wall suction values are same as in previous figures. All other parameters are same as in table A1.	80
3.7	Block diagram showing the steps involved in formulating the trajectory model.	81
4.1	Plot of real part of frequency dependent Clausius-Mossotti factor for water-in-oil and oil-in-water systems, against frequency of the applied ac signal. ϵ_p^* and ϵ_m^* represent the complex permittivity of particles and surrounding medium, respectively. The electrical properties of the particle and medium are listed in table A2 in the appendix.	92

4.2	(a) Effect of applied voltage on droplet trajectory (at different height) inside the channel. The horizontal axis in this plot is nondimensionalized with respect to electrode pitch, which is 100 μm and the vertical axis is nondimensionalized with respect to electrode width, which is 50 μm in this case. Applied voltage is 50 V, frequency $\omega = 600$ Hz. Sticking time for droplets released from different locations is shown on the plot. (b) Applied voltage, V is 100 V, frequency, $\omega = 600$ Hz. All other parameters remain same as in the previous plot.	93
4.3	(a) Effect of droplet size on droplet trajectory inside the channel. Droplet size varies from 100 nm to 1500 nm. Applied voltage, V is 50 V, frequency in this case is 600 Hz. Trajectory for droplets of different sizes released from same location. The horizontal axis and the vertical axes are non-dimensionalized as in previous figure (b) Plot of sticking time for droplets of different sizes released from the same location. All parameters are same as in previous plot. The flat part of the droplet trajectory indicates that the droplet has traversed across the electrode array plane and is not effected of DEP forces anymore.	94
4.4	Dependence of DEP force on droplet size. Droplet size varies from 100 nm to 1500 nm. Applied voltage, V is 50 V, frequency in this case is 600 Hz.	95
4.5	Effect of electrode width and spacing on droplet trajectory. Applied voltage, V is 50 V and frequency is 600 Hz. The horizontal and vertical axes are non-dimensionalized with respect to electrode pitch, which is 100 μm	96
4.6	Effect of membrane suction on droplet trajectory. Applied voltage is 50 V and frequency is 600 Hz. The horizontal and vertical axes are non-dimensionalized with respect to electrode width, which is 50 μm . The uniform wall suction is 5×10^{-5} m/s.	97
4.7	Separation effectiveness of the DEP based membrane filtration system. The horizontal axis shows droplet release height inside the channel. Effect of applied voltage on separation effectiveness is also shown. Applied voltage, V varies from 50 V to 100 V, frequency is 600 Hz.	98

4.8	Trajectory of droplets released from a height range of 33 to 35 μm . Applied voltage, V is 50 V, frequency is 600 Hz.	99
5.1	Trajectory of a particle in latex-in-water system under negative DEP, with uniform and intermittent wall suction. Both axes are nondimensionalized with respect to electrode width (W). The average crossflow velocity and maximum wall suction values are 10^{-3} m/s and 10^{-5} m/s, respectively. All other parameters are same as in table A1.	107
5.2	Trajectory of particles in latex-in-water system, released from different heights over the membrane surface. Both axes are nondimensionalized with respect to electrode width (W). (a) Uniform wall suction, $V_W = 10^{-6}$ m/s and average cross flow velocity is 10^{-3} m/s. (b) Uniform wall suction, $V_W = 10^{-5}$ m/s and average cross flow velocity is 10^{-3} m/s. All other parameters are given in table A1.	108
5.3	Effect of wall suction and applied voltage on equilibrium height attained by particles in the negative DEP force field. The horizontal and vertical axes are scaled with respect to wall suction, $V_w = 10^{-5}$ m/s and electrode width (W), respectively. Uniform wall suction is considered in this case. All other parameters are same as in table A1.	109
6.1	Schematic representation of the experimental setup, showing different components of the system.	118
6.2	Steps involved in microfabrication of the interdigitated electrode array.	119
6.3	Image of the microfabricated electrode array with a closeup view of the parallel electrodes.	120
6.4	Video images of water droplet movement inside the crossflow channel. The water droplets are subjected to positive DEP force. The three images correspond to three sequential time frames, $t = 0, 0.2$ and 1 sec.	121

List of Symbols

a	particle radius (m)
a_j, b_j	distance of leading and trailing edge of j_{th} electrode (m)
d	half of center to center electrode distance, pitch is $2d$ (m)
\mathbf{E}	electric field vector (Vm^{-1})
E_x, E_y	electric field components in x and y directions, respectively (Vm^{-1})
\tilde{f}_{CM}	Clausius-Mossotti factor
\mathbf{f}_e	electrical body force
f_i	universal hydrodynamic correction factors
F	force magnitudes (N)
F_x	forces in x direction
F_y	forces in y direction
F_{DEP}	dielectrophoretic force (N)
G	spacing between two consecutive electrodes
h	surface to surface separation distance (m)
H	Half channel height
k	Boltzmann constant ($1.38 \times 10^{-23} \text{ JK}^{-1}$)
m	mass of each particle
\mathbf{p}	dipole moment (Cm)
P	pitch of the electrode array
\mathbf{P}	polarization, dipole moment per unit volume
Q	electrical charge on the dipole (Coulomb)
r	arbitrary distance
u	drop velocity (ms^{-1})
v	volume of a sphere

v_x, v_y	undisturbed fluid flow components in x and y directions, respectively (ms^{-1})
V_o	amplitude of applied voltage (volts)
V_w	uniform suction velocity at the bottom wall (ms^{-1})
\bar{V}_x	average cross flow velocity in horizontal direction (ms^{-1})
W	electrode width
x, y	horizontal and vertical directions in Cartesian coordinate system, respectively
X	axial location where the droplets stick to the membrane

Greek Alphabets

α	polarizability (CV^{-1}m^2)
ϵ_p, ϵ_m	relative permittivity of particle and surrounding medium
ϵ_0	permittivity of free space ($8.85418 \times 10^{-12} \text{ Fm}^{-1}$)
η	separation effectiveness
λ	dimensionless distance from bottom wall
μ	viscosity of the suspending medium (Nm^{-2})
σ	electrical conductivity (Sm^{-1})
ϕ	electrical potential
ψ	auxiliary function
ω	frequency of applied voltage (Hz)

Abbreviations

DI	deionized
DEP	dielectrophoresis
IPO	iso propyl alcohol
PMMA	poly methyl methacrylate

Chapter 1

Introduction

1.1 Background and Overview

The concept of particle movement by the application of external forces has been explored extensively during the last few decades. Powerful techniques have emerged as an outcome of the increasing attention to this promising research area. Researchers have produced feasible means to gain better control over microscopic entities, such as, colloidal particles (10^{-9} m - 10^{-5} m), bacteria (10^{-6} m), and virus (10^{-7} m) [Hughes, 2002]. At the foundation of these techniques is the interaction of the microscopic entities with an external force field imposed on them. Various types of force fields can be used for manipulating or sorting particles, including optical tweezers, ultrasound, magnetic sorting, and centrifugation [Morgan and Green, 2002]. Electric field based techniques have proved to be very effective in creating manageable forces on the bodies. The past decade has seen an explosion of interest in microsystems for biological and chemical analysis. Electric field based manipulation and separation methods are highly suitable for integration into microdevices [Hughes, 2000, Cui *et al.*, 2002, Huang *et al.*, 2003]. Particle transport phenomena under the influence of electrical fields is generally known as *electrokinetics* and have found useful applications in various industrial processes [Masliyah, 1994].

In general, whenever charged particles are placed in an electric field, the particles exhibit continuous motion along the electric field lines. This aspect

of electrokinetics has been successfully used to separate charged bodies from a mixture. However, this is not the case for uncharged bodies, *i.e.*, bodies with no net charge. Comprehensive study of the movement of neutral bodies in an electric field was pioneered by Herbert Pohl, who wrote the classic text on this subject [Pohl, 1978]. Pohl used the term *dielectrophoresis* to define the motion of neutral bodies in a non-uniform electric field. Pohl identified the underlying physics of dielectrophoresis and outlined the prospect of this electrokinetic phenomenon.

In this dissertation, the electrical forces arising from the interaction of particles and the surrounding medium with an alternating electric field are at the center of interest. If these electrical forces are coupled with the conventional separation processes, the combination will open up a new frontier of highly effective separation technologies.

1.2 Objectives and Scope

The movement of electrically neutral particles in a continuous medium can be utilized to enhance separation processes. The primary objective of the work presented here is to capitalize on the potential of the electric field based technique, dielectrophoresis, to address several problems related to membrane based separation processes [Mulder, 1996]. In that context, a novel concept of coupling dielectrophoresis with membrane filtration is proposed, which can potentially enhance traditional membrane separation processes in two ways. First, the concept of dielectrophoretic membrane filtration can be developed to selectively enhance removal of trace amounts of a target species from a suspension. Secondly, the technique can be utilized to mitigate membrane fouling, a typical problem encountered during operation of membrane separation processes that can adversely affect the operation.

The feasibility of the proposed technique is studied by developing a model that can be employed to determine the behavior of the target particles in a

crossflow membrane filtration system. The membrane filtration system in this work is considered to be modified by incorporating parallel electrode array (set of parallel metallic conductors, separated by a distance) on the membrane surface, to create the necessary electrical forces. The nature of the dielectrophoretic force acting on the proposed system is determined by the electrical properties of the target species and the surrounding medium, as well as, the characteristics of the applied electrical signal. These properties determine the attractive or repulsive characteristics of the dielectrophoretic force. Therefore, study of the relative influence of various control parameters is also one of the key components of this work.

The concept of dielectrophoretic membrane filtration proposed in this work can be incorporated into various membrane separation processes to significantly improve separation efficiency. The dielectrophoretic forces are highly suitable for any separation process that involves removal of microscale entities. This technique can be used in conjunction with flow fractionation to separate biological samples and components of a complex fluid. The frequency dependent nature of the dielectrophoretic force can provide the basis for a valuable detection mechanism for chemical agents. On the other hand, repulsive (negative) dielectrophoretic force can be used to deter unwanted materials from depositing on a surface.

1.3 Organization of the Thesis

In this chapter, the overall objectives and scope of the study have been delineated. In chapter 2, the concept of ac dielectrophoresis is presented, followed by a discussion on how a parallel electrode array can be embedded on a cross-flow filtration membrane to couple dielectrophoresis with membrane filtration. Detailed analytical and numerical solutions for the electric fields and dielectrophoretic forces on such parallel electrode arrays are presented. Chapter 3 is devoted to the development of a modelling framework based on trajectory anal-

analysis to assess particle transport in a crossflow membrane filtration system, enhanced with a dielectrophoresis based force field. Combined, chapters 2 and 3 provide the general theoretical framework for addressing the dielectrophoretic membrane filtration problem. In chapters 4 and 5, two aspects of membrane filtration enhanced by dielectrophoresis are explored theoretically. First, in chapter 4, the enhancement of separation effectiveness for a binary water-in-oil emulsion is studied employing attractive (positive) dielectrophoresis to preferentially attract the water droplets toward the membrane. In chapter 5, the application of repulsive (negative) dielectrophoresis to prevent deposition of colloidal particles on a membrane and abatement of membrane fouling is discussed. Chapter 6 discusses the preliminary experimental verifications of the principles of dielectrophoresis enhanced separation. Finally, chapter 7 summarizes the key observations and conclusions from this work and delineates some key recommendations for future studies in this direction.

Chapter 2

Dielectrophoresis

2.1 Introduction

It has been long known to the scientific community that electrostatic forces, particularly the forces that originate from the interaction between particles and an imposed electrical field, are of paramount importance in manipulation and separation of microscale entities. The motion of particles and fluids in dc electric field has been studied for over 100 years. However, the study of particle movement in ac electric fields has gained momentum only during the past three decades, pioneered by Herbert Pohl. Study of the effect of alternating electric field on particles is now commonly referred to as ac electrokinetics. *Dielectrophoresis* is now regarded as one of the important branches of ac electrokinetics. In this chapter, we will discuss the theoretical aspects of the electrokinetic phenomena known as dielectrophoresis, to gain an understanding of the potential of dielectrophoresis as the driving force behind the applications proposed in this work. The term *DEP* is generally used as an abbreviation for dielectrophoresis.

One of the early experimental observations of dielectrophoretic phenomena was reported by Hatschek and Thorne, 1923. The phenomena was later named dielectrophoresis by Herbert Pohl [Pohl, 1951]. Pohl later published an thorough analysis of this subject in his book *Dielectrophoresis* in 1978 [Pohl, 1978]. Pohl's work on DEP demonstrated the potential of a new form of electrical force to manipulate and characterize small scale entities, for instance, investi-

aggregating properties of suspensoids and separation of particles from suspensions. DEP based applications have been extensively used in biological sciences to characterize and separate biological entities. Frequency-based investigation of dielectrophoretic response of a population of cells was undertaken by Kaler and Jones, 1990, Gascoyne *et al.*, 1993, Fuhr *et al.*, 1994, Markx and Pethig, 1995. Manipulation of virus [Morgan and Green, 1997, Hughes *et al.*, 1998, Hughes *et al.*, 2001] and characterization of microorganisms [Markx *et al.*, 1994] have been achieved by employing DEP based techniques. Practical applications of DEP include the collection of cells for cellular fusion in biological experiments [Zimmermann and Vienken, 1982, Abidor and Sowers, 1992]. DEP has found effective application in cancer research to separate a mixture of healthy and leukemic blood cells [Gascoyne *et al.*, 1992, Gascoyne *et al.*, 1994].

Considering the Brownian motion induced particle displacements, it was anticipated [Pohl, 1978] that the DEP induced deterministic motion of micron and sub-micron particles could not be achieved with the electric field strength available at that time. Early experiments used electric fields generated by relatively large electrodes and high voltages to collect particles. But with the advent of microfabrication technology it has been possible to fabricate electrode structures with length scales measuring in micrometers. These microelectrodes can generate large electric fields ($10^6 - 10^7$ V/m) from small voltages, to manipulate much smaller particles [Pethig *et al.*, 1992, Washizu and Jones, 1994, Fuhr and Shirley, 1995, Green and Morgan, 1997, Green *et al.*, 1997].

Dielectrophoretic fractionation has also been used in process engineering applications quite often, particularly for flocculation of colloidal entities in a uniform electric field [Shapiro *et al.*, 1985, Eow *et al.*, 2001]. In these processes, the local field gradients engendered by the different dielectric permittivities of the colloids and the suspending media result in an attractive force between the particles, leading to flocculation. DEP based field-flow fractionation of colloidal mixtures has proved to be highly efficient [Holmes *et al.*, 2003, Suehiro *et al.*, 2003, Yang *et al.*, 1999, Markx *et al.*, 1997b, Markx *et al.*, 1997a] with

specific electrode configuration. In this case, negative DEP force field is used to levitate particles of different polarizability to different equilibrium heights and consequently are fractionated along the length of the electrode array due to varying amount of drag force experienced by particles at different heights.

In this chapter, so far, a brief literature survey focusing on the fundamentals of ac dielectrophoresis has been presented. This will be followed by a description of ac dielectrophoresis on parallel electrode arrays. Then, an analytical method based on Green's function approach [Clague and Wheeler, 2001] is explained to predict the electrical field and DEP force distribution on a parallel electrode array. A finite element model was also developed to evaluate DEP force field and compare the numerical and analytical results.

2.2 Governing Principles of AC Dielectrophoresis

2.2.1 Electrical forces on particles and fluids

Particles suspended in a fluid, as well as the surrounding fluid medium can be moved only by the action of an external deterministic force, a force that can be controlled to a large extent. Other than the deterministic forces, there are random forces at work on the system originating from the thermal energy or temperature of the system, causing the suspended particles to move in random manner. This random motion, referred to as Brownian motion, can be controlled only by altering the viscosity of the suspending medium or the temperature of the system. Only sufficiently large deterministic forces can be effectively used to manipulate micron size particles. Therefore, manageable electrical forces acting on suspended particles open up a window of opportunity to manipulate, separate and characterize various colloidal entities suspended in a continuous medium.

When a charged particle is placed in a uniform dc electric field, it tends to move along the electric field lines toward the direction of the electrode with

opposite polarity of the charge. The charged particle will invariably follow the electric field lines even if the electric field in which it has been placed is non-uniform (spatially varying). Thus any electric field, uniform or non-uniform, exerts a force upon charged body.

In contrast, when a neutral body is placed in a uniform electric field the body will merely be polarized. In a uniform field, this may result in a torque due to anisotropic polarizability of the body or deformed shape of the body in the electric field. However, there will be no translational motion of the body since the forces acting on the two poles (equal and opposite charges) originating from the neutral body, will be equal and opposite in action. If instead, the neutral body is subjected to a non-uniform electric field, the polarized body will experience a net force toward the stronger field region due to unequal field regions acting on the two equal and opposite charges. Therefore, the usual result of polarization of a neutral body in a non-uniform field is to produce a force impelling the neutral body toward the region of stronger field. Furthermore, reversal of the polarity of the electric field as in ac electric field does not change the direction of movement of a polarized body simply because the polarization of the neutral body is also reversed. Figure 2.1 shows the movement of a charged body and a polarized neutral body in a non-uniform electric field.

Following the description above, dielectrophoresis can now be formally defined. According to Pohl, *Dielectrophoresis* is the translational motion of neutral matter caused by polarization effects in a nonuniform electric field [Pohl, 1951]. Pohl further described dielectrophoresis as the result of interaction between a non-uniform electric field and induced effective dipole moment of the neutral particle [Pohl, 1978]. In view of interaction of particles with an electric field, several other electrokinetic phenomena should be mentioned. For instance, charged bodies with non-zero net charge experience a Coulomb force in an electric field (uniform or non-uniform). The resulting motion of the charged particle due to that force is known as *electrophoresis*. Alternatively, when a body is subjected to a field with rotating field vector, the body experiences torque. This occurrence

of torque on a body is termed *electrorotation*. In general, both the particle and the suspending fluid can experience the electrical forces. Electrical fields produce a dielectrophoretic force on the surrounding medium if there is variation in charge density of the medium. Fluid movement due to the interaction of the field and free charge in a dc field is termed as *electroosmosis*. However, in this work, the forces evolving from dielectrophoresis has been focused only.

2.2.2 Induced dipole

When a polarizable particle suspended in a dielectric medium is subjected to an electric field, the interface between the two phases acquires a charge distribution which depends on the conductivity and permittivity of the two materials. This interfacial charge distribution plays a pivotal role in determining the nature of the dielectrophoretic force. The charge distribution around the particle can be described in terms of *polarizability*- a measure of the ability of a material to respond to a field and also a measure of the ability of a material to produce charge at interfaces [Morgan and Green, 2002].

If the polarizability of a particle in an electric field is higher than the polarizability of the surrounding medium, there will be a difference in charge density on either side of the particle, *i.e.*, across the interface. This gives rise to an effective or induced dipole across the particle aligned with the electric field. If the field is removed the dipole disappears and thus referred to as *induced* dipole. Conversely, when the particle is less polarizable than the surrounding medium, the net dipole points in the direction opposite to the electric field. However, no net dipole develops if both the particle and the medium possess same degree of polarizability.

The charge distribution at the interface does not occur instantaneously after a polarizable particle is placed in an electric field. Usually the time delay required to reach an equilibrium state is few microseconds. In case of reversal of the applied electric field, the dipoles realign with the electric field during this time duration. So at low frequency of the applied electric field, the dipoles have

enough time to reorient themselves with the changing direction of the applied field. However, with increase in frequency, the charges at some point can no longer respond to the changing field directions. From this point onward, the free charge movement is not a dominant factor in determining the charge at the interface, rather the bound charges (permittivity) are responsible for charging the interface between the two phases. The difference between these two states are termed as *dielectric dispersion* [Morgan and Green, 2002]. At high frequencies, the direction of the induced dipole changes from being in alignment with the field at low frequencies, to opposing the field. Therefore, interfacial polarization and induced dipole both are highly dependent on the frequency of the applied field in an ac electric field.

2.2.3 Positive and negative dielectrophoresis

The disparity in polarizability of the two phases dictates the basic nature of interaction with the electric field imposed on the system. Figure 2.2 shows the electric field distribution in two conceivable cases. First, a highly polarizable particle is considered to be suspended in a medium which has lower polarizability than the particle and then the opposite scenario. As shown in Figure 2.2a when the particle is more polarizable than the medium, it acts more like a conductive sphere with nearly no field inside. The electric field lines bend towards the particle and the contact angle tends to be right angle with increasing polarizability of the particle. On the other hand, if the particle is less polarizable than the surrounding medium (the medium is more conductive than the particle), the field lines bend around the particle as if the particle is an insulator with same fields inside and outside the interface. The latter case is shown in Figure 2.2b.

These two cases can be extended to understand the behavior of the same two particles, if they are subjected to a non-uniform electric field instead of a uniform field. The field lines would behave in the same manner as in previous two cases for respective particles. However, now the spatially varying field

will induce a net force on the two particles. In case of the highly polarizable particle, the field distribution will cause a net force acting towards the high field region, causing the particle to move towards the region of high field gradient. Conversely, the field distribution around the less polarizable particle will cause a net force that acts opposite to the region of high field gradient, causing the particle to move away from that region. These two cases are known as *positive* and *negative* dielectrophoresis, respectively. Therefore, the DEP force acting on a polarizable particle depends on the intrinsic properties of the particle and the surrounding medium, as well as the frequency of the applied field. This is one of the key aspects of dielectrophoresis that renders it as a promising technology for manipulation of microscale entities.

2.2.4 Effective dipole of particles

In general, ac electrokinetic systems consist of a suspension of dielectric particles in a dielectric fluid. On application of an electric field, surface charges accumulate at the interface between the two dielectrics due to differences in electrical properties. This distribution of surface charge density around the surface of the particle gives rise to an induced dipole. The interaction between these induced dipoles and the electric field is the basis of ac electrokinetic forces and torques.

Let us consider an electric dipole originating from a simple charge distribution consists of two charges of the same magnitude Q and opposite sign, separated by a finite distance d as shown in Figure 2.3 . The *dipole moment*, \mathbf{p} , is defined as a vector directed from the negative to the positive charge. The dipole moment has units of Coulomb-meter or Debye (1 Debye = 3.33×10^{-30} C-m).

$$\mathbf{p} = Q\mathbf{d} \quad (2.1)$$

The dipole potential and field at an arbitrary distance r ($r \gg d$) are defined as (in spherical co-ordinates) [Morgan and Green, 2002]

$$\phi = \frac{\mathbf{p} \cdot \hat{\mathbf{r}}}{4\pi\epsilon_0 r^2} \quad (2.2a)$$

$$\mathbf{E} = \frac{\mathbf{P}}{4\pi\epsilon_0 r^3} (2 \cos \theta \hat{\mathbf{r}} + \sin \theta \hat{\boldsymbol{\theta}}) \quad (2.2b)$$

where, \mathbf{E} is the electric field due to dipole and ϵ_0 is the absolute permittivity of free space.

If the dipole is placed in a non-uniform electric field, the two charges on the dipole will experience an imbalance of force in the non-uniform field, *i.e.*, there will be a net force acting on the dipole. If a dipole with charges $+Q$ and $-Q$ is acted upon by a non-uniform field \mathbf{E} , the net force can be expressed as

$$\mathbf{F} = Q\mathbf{E}(\mathbf{r} + \mathbf{d}) - Q\mathbf{E}(\mathbf{r}) \quad (2.3)$$

where \mathbf{r} is the position of the negative charge on the dipole and \mathbf{d} is the distance vector between the two poles as shown in Figure 2.3. If the length of the vector \mathbf{d} is small compared with the typical dimension of the non-uniformity of the electric field, \mathbf{E} can be expanded around \mathbf{r} using a vector Taylor series

$$\mathbf{F} = Q\mathbf{E}(\mathbf{r}) + Q(\mathbf{d} \cdot \nabla)\mathbf{E} + \text{Higher order terms} - Q\mathbf{E}(\mathbf{r}) \quad (2.4)$$

Substituting for the dipole moment from Eq.(2.1) and neglecting the higher order terms, the above expression can be written as

$$\mathbf{F} = (\mathbf{p} \cdot \nabla)\mathbf{E} \quad (2.5)$$

This force expression implies that there will be no DEP force involved in a uniform electric field. The assumption that the length of the dipole \mathbf{d} is much smaller than the typical dimension of the field non-uniformity, is known as *dipole relaxation*. This assumption is only valid when the magnitude of the electric field does not vary significantly across the dimension of the dipole. Multipole force terms must be considered when this assumption is no longer valid. An alternative and more exact method is to use Maxwell stress tensor which requires exact solution for potential in the system and the integration of the stress tensor around the particle surface to obtain the force [Jones, 1985, Washizu and Jones, 1994, Wang *et al.*, 1997].

Complex permittivity of dielectrics and Clausius-Mossotti factor

A dielectric is a material that contains charges which polarize under the influence of an applied electric field. These charges are bound within the material and can only move short distances under the applied field, opposite charges move in opposite directions to form induced dipole. The average dipole moment of the molecules of a dielectric material is proportional to the magnitude of the field

$$\mathbf{p}_{\text{av}} = \alpha \mathbf{E}' \quad (2.6)$$

where, \mathbf{E}' is the local electric field around the dipole and α is called the *polarizability*, a measure of the response of the dielectric to the electric field. It has units of $(\text{CV}^{-1}\text{m}^2)$ or (Fm^2) . In a dielectric consisting of n molecules per unit volume, the *polarization* \mathbf{P} (dipole moment per unit volume) is defined as $\mathbf{P} = n\mathbf{p}_{\text{av}}$. The polarization and the displacement of the charges give rise to a net charge at points in the dielectric or at the surface, referred to as polarization or bound charges.

There are three basic molecular polarization mechanisms when an electric field is applied to a dielectric: electronic, atomic and orientational. In addition, interfacial polarization is a long range effect due to accumulation of charges at the internal interfaces in the dielectrics. Focus will be on interfacial polarization since it is the origin of the induced dipole on particles.

Let us consider the polarization of a dielectric with permittivity ϵ and conductivity σ , *i.e.*, leaky dielectric, which is like most real dielectrics. In case of leaky dielectrics, the polarization of the medium depends on the frequency of the applied field. Using the analogy of a parallel plate capacitor as shown in Figure 2.4 containing homogeneous dielectric subjected to a potential difference V of angular frequency ω , the *complex permittivity* is defined as

$$\epsilon^* = \epsilon - i\frac{\sigma}{\omega} \quad (2.7)$$

where ϵ^* is the complex permittivity of the system and i is an imaginary quantity defined as $\sqrt{-1}$. Let us now consider a homogeneous dielectric sphere (particle)

of radius a , suspended in a homogeneous dielectric medium and subjected to a uniform electric field. The sphere is assumed to have its center at the origin so that the problem is axially symmetric in a two dimensional spherical co-ordinate system. For an ideal dielectric sphere, the solution for potential and electric field in and around the sphere can be obtained by solving *Laplace* equation $\nabla^2\phi = 0$. *Gauss's* law provides the boundary condition at the interface of the two dielectrics or at the surface of the sphere

$$\varepsilon_m \mathbf{E}_m \cdot \hat{\mathbf{n}} = \varepsilon_p \mathbf{E}_p \cdot \hat{\mathbf{n}} \quad (2.8)$$

where the subscripts m and p indicate particle and suspending medium, respectively. The same boundary conditions can be used for continuity of displacement ($\mathbf{D} = \varepsilon_0 \mathbf{E} + \mathbf{P}$), if the dielectrics are not ideal, *i.e.*, the permittivities of the dielectrics are complex and the applied field is harmonic of single frequency ω . Only the complex permittivity values need to be substituted. The solutions for the potential outside and inside the sphere are [Morgan and Green, 2002]

$$\phi_m = E a^3 \left(\frac{\varepsilon_p^* - \varepsilon_m^*}{\varepsilon_p^* + 2\varepsilon_m^*} \right) \frac{\cos \theta}{r^2} - E r \cos \theta \quad (2.9)$$

$$\phi_p = - \left(\frac{3\varepsilon_m^*}{\varepsilon_p^* + 2\varepsilon_m^*} \right) E r \cos \theta \quad (2.10)$$

where r is the distance from the origin and $r = a$ describes the surface of the sphere. E is the magnitude of the initial uniform electric field. The potential distribution outside the sphere has contribution from the dipole moment, which is the first part and the applied field, represented by the second part on the right hand side of the equation. By comparing with dipole potential in Eq. 2.2, the dipole moment is

$$\mathbf{p} = 4\pi\varepsilon_m \left(\frac{\varepsilon_p^* - \varepsilon_m^*}{\varepsilon_p^* + 2\varepsilon_m^*} \right) a^3 \mathbf{E} \quad (2.11)$$

This is the *effective dipole moment* of the dielectric sphere. It can be written in terms of the volume v of the sphere and *complex effective polarizability* $\hat{\alpha}$ as

$$\mathbf{p} = v \hat{\alpha} \mathbf{E} \quad (2.12)$$

Therefore, effective polarizability is

$$\hat{\alpha} = 3\varepsilon_m \left(\frac{\varepsilon_p^* - \varepsilon_m^*}{\varepsilon_p^* + 2\varepsilon_m^*} \right) = 3\varepsilon_m \tilde{f}_{CM} \quad (2.13)$$

\tilde{f}_{CM} is called the *Clausius-Mossotti factor* that describes the dependence of polarizability and effective dipole moment on the frequency of the applied electric field. At low frequency the real part of the Clausius-Mossotti factor reaches a limiting value of $(\sigma_p - \sigma_m)/(\sigma_p + 2\sigma_m)$, indicating dominance of conductivity of the system. At high frequency the limiting value is $(\varepsilon_p - \varepsilon_m)/(\varepsilon_p + 2\varepsilon_m)$, the polarization is dominated by permittivity of the particle and suspending medium. In general, the real part of the Clausius-Mossotti factor is bounded by 1 and -0.5.

To demonstrate the frequency dependence of Clausius-Mossotti factor, let us consider an example of latex-in-water system. The conductivity of latex particles (σ_p) is considered to be higher than the conductivity of DI water (σ_m) and water has a much higher value of permittivity than latex ($\varepsilon_m \gg \varepsilon_p$). The electrical properties of the latex-in-water system are listed in table A1 in the appendix. The real part of the Clausius-Mossotti factor for this system ranges from positive to negative values depending on the frequency of the applied ac voltage as well as the properties of the two components. Figure 2.5 shows the variation of the real part of the Clausius-Mossotti factor with respect to frequency. This variation of the real part of the Clausius-Mossotti factor means that the same latex particles may experience either attraction or repulsion in water if the frequency of the applied voltage is varied from low to high frequency. The frequency at which the $\text{Re}[\tilde{f}_{CM}]$ is zero is called *crossover frequency*, since the DEP force value changes sign on either side of this frequency. At this frequency the particle experiences no DEP force at all. The crossover point is marked by the symbol in Figure 2.5. Crossover frequencies are a product of dielectric dispersions that cause the relative polarizability of the particle to change. Origin and implications of crossover frequency have been discussed in Hughes, 2002.

As mentioned before, it is important to note that dielectrophoresis originates from non-uniform electric field. However, the uniform field solution for the dipole moment is used as the foundation. This approximation is only valid when the size of the particle is small compared with the characteristic length associated with field non-uniformity.

2.2.5 Dielectrophoresis in an AC field

Within the scope of this research, we will only focus on DEP forces engendered from a non-uniform electric field with spatially varying magnitude (constant phase) of the applied field, also known as stationary wave DEP. If both the magnitude and phase of the applied ac signal vary then the resulting DEP force is called a travelling wave DEP (twDEP).

Assuming an applied potential of a single frequency ω , the time dependent values in a system can be represented in terms of phasors. Let us define an arbitrary potential

$$\phi(\mathbf{x}, t) = \text{Re}[\tilde{\phi}(\mathbf{x})e^{i\omega t}] \quad (2.14)$$

$$\tilde{\phi} = \phi_R + i\phi_I \quad (2.15)$$

where i is an imaginary quantity defined as $i = \sqrt{-1}$, \mathbf{x} is the spatial location and $\tilde{\phi}$ represents complex phasor. ϕ_R and ϕ_I are the real and imaginary components of the complex phasor, respectively. The corresponding electric field can be defined as

$$\tilde{\mathbf{E}} = -\nabla\tilde{\phi} \quad (2.16)$$

and

$$\mathbf{E}(\mathbf{x}, t) = \text{Re}[\tilde{\mathbf{E}}(\mathbf{x})e^{i\omega t}] \quad (2.17)$$

where \mathbf{E} is the amplitude of the electric field. Since the phase is constant in stationary wave DEP, the field phasor can be assumed to be real without the loss of generality ($\tilde{\mathbf{E}} = \mathbf{E} = -\nabla\phi_R$). The dipole moment of the particle is now

$$\tilde{\mathbf{p}} = v\tilde{\alpha}\mathbf{E}e^{i\omega t} \quad (2.18)$$

where all symbols bear the same meaning as before. From Eq. 2.5 the time averaged force on the particle is

$$\langle \mathbf{F}_{DEP} \rangle = \frac{1}{2} Re[(\tilde{p} \cdot \nabla) \mathbf{E}^*] \quad (2.19)$$

where * represents complex conjugate. Since the phasors are real, the above equation can be rewritten as

$$\langle \mathbf{F}_{DEP} \rangle = \frac{1}{2} v Re[\tilde{\alpha}] (\mathbf{E} \cdot \nabla) \mathbf{E} \quad (2.20)$$

Using the vector identity: $\nabla(\mathbf{A} \cdot \mathbf{B}) = (\mathbf{A} \cdot \nabla) \mathbf{B} + (\mathbf{B} \cdot \nabla) \mathbf{A} + \mathbf{B} \times (\nabla \times \mathbf{A}) + \mathbf{A} \times (\nabla \times \mathbf{B})$ and the irrotational ($\nabla \times \mathbf{E} = 0$) property of the electric field, the time averaged DEP force can be expressed as

$$\langle \mathbf{F}_{DEP} \rangle = \frac{1}{4} v Re[\tilde{\alpha}] \nabla(\mathbf{E} \cdot \mathbf{E}) \quad (2.21)$$

or

$$\langle \mathbf{F}_{DEP} \rangle = \frac{1}{4} v Re[\tilde{\alpha}] \nabla |\mathbf{E}|^2 \quad (2.22)$$

This is the governing equation for DEP force on a polarizable spherical particle in a non-uniform electric field that is to be used in all the analysis in the following chapters.

This equation indicates that the DEP force depends on the volume of the particle and the gradient of the field magnitude squared. The force also depends on the real part of the effective polarizability and consequently the frequency of the ac voltage. As mentioned earlier, the real part of the Clausius-Mossotti factor determines the nature of the stationary DEP force. When the particle is more polarizable than the medium ($Re[\tilde{f}_{CM}] > 1$), the particle experiences attractive DEP force towards the regions of high field strength. Conversely, if the particle is less polarizable than the medium ($Re[\tilde{f}_{CM}] < 1$), the resulting DEP force is repulsive, repelling the particle away from the region of high field strength.

2.2.6 Dielectrophoresis on parallel electrode array

In this section, the technique will be described to generate strong dielectrophoretic force field on the polarizable particles in a suspended medium and the evaluation of the DEP force. As mentioned before, typical electrode dimension would require a high voltage source to produce the large electric field gradients necessary to produce DEP force, which in most cases is not feasible. To avoid this limitation, the size of the electrodes can be reduced by several orders of magnitude. The reduced size of the electrodes results in an increase of DEP force, inversely proportional to the cube of the separation distance between the electrodes. Advances in micro- and nano-fabrication techniques now can produce electrodes that are as small as $1\mu\text{m}$ in size. This in effect can produce very high electric field, e.g. two electrodes separated by $1\mu\text{m}$ with an applied potential difference of 10 V can generate a field strength of 10^7 Vm^{-1} . The strength and the morphology of the electric field engendered from an electrode array are also highly dependent on the electrode structure. Therefore, using electrodes with a characteristic length scale of few micron can provide a solution to the problems associated with high voltage applications. Considerable amount of work has been done in terms of electrode design and configuration. Several types of electrode structures, namely, polynomial [Huang and Pethig, 1991, Pethig *et al.*, 1992], castellated [Pethig *et al.*, 1992] and interdigitated electrode [Fuhr *et al.*, 1991, Hagedorn *et al.*, 1992, Wang *et al.*, 1993] geometries, have been explored and discussed in the literature, with the focus on particle manipulation, characterization and separation.

Interdigitated electrode arrays are widely used in ac electrokinetics. Interdigitated electrode arrays are primarily used for standing wave DEP separation. Moreover, same type of electrodes are also used for generation of travelling electric fields for travelling wave DEP (twDEP). Interdigitated electrode design consists of long array of successively addressed thin parallel bar microelectrodes, typically $10\text{-}50\ \mu\text{m}$ wide. Figure 2.6 shows a schematic diagram of an interdigitated electrode array that is representative of the electrode configuration used

in this model. The length of the electrodes on the array are assumed to be significantly larger than the other dimensions of the electrodes so that the electrodes can be modelled as a two dimensional problem. Since the electrodes are generally fabricated using microfabrication techniques, the electrodes can be assumed to be infinitely thin. The space above the electrode plane is considered to be infinite compared to the electrode dimension. For simple or stationary wave DEP, the electrodes are energized by 180° phase-shifted electric potential, *i.e.*, two consecutive electrodes have equal and opposite potential imposed on them. Figure 2.7 shows the potential distribution at the electrode plane over three consecutive electrodes in an array of interdigitated electrodes. The potential in the gap region is assumed to vary linearly; validity of this assumption will be discussed later. The electric field engendered by this type of array will be used in this work to evaluate the DEP force on the polarizable particles suspended in a dielectric medium.

2.3 Dielectrophoretic Force Calculation: Analytic Approach

The dielectrophoresis phenomena is only observed in an nonuniform electric field; in the presence of high field gradient. Therefore, clear understanding and information of the electric field distribution are the primary components of DEP force evaluation for a given system and necessary to predict the regions where particles would experience maximum positive or negative DEP force. In this section, the analytical solution for electric field over a parallel electrode array is obtained, followed by evaluation of DEP forces on a spherical polarizable particle in the non-uniform electric field. The general formulation leading to the analytical solution of the electric field produced by the parallel electrode array has been adopted from Clague and Wheeler, 2001. The expressions for electric potential and electric field distribution were derived using the general formulation to obtain the correct forms. The corrected forms of analytical solutions for

the electric field distribution were later employed to evaluate DEP forces acting on a polarizable particle suspended in a medium with different polarizability than the particle; subjected to the non-uniform electric field engendered by the electrode array.

2.3.1 Electric field evaluation

Evaluation of electric field in a given space can be categorized as *analytical modelling* and *numerical modelling*. Analytical modelling is about obtaining the exact solution of the electric field at every point in the problem space using a series of equations, which is relatively easy task for simple geometries. However, obtaining an analytic form of the solution can pose a formidable challenge if the electrode geometry is relatively complicated. In such cases, numerical modelling based on some sort of numerical approximation offers a discrete solution of the electric field, rather than a continuous solution. Irrespective of the solution approach, the solution methodology generally begins by formulating the problem in some form of *Poisson's* equation

$$\nabla E = - \frac{\rho}{\epsilon} \quad (2.23)$$

where E is the electric field, ρ is the charge density, ϵ is the permittivity, and ∇ is the del operator. For a system without free charge, the potential distribution can be obtained by simplifying Poisson's equation as

$$\nabla^2 \phi = 0 \quad (2.24)$$

Electric field E is related to the applied electric potential ϕ as $E = -\nabla\phi$. For the present analysis, an interdigitated parallel electrode geometry has been chosen as shown in Figure 2.6, primarily for the simplicity of the design and also considering the overall design aspects of the proposed device. Solution for the potential field produced by the planar electrode array has been obtained by following the *Green's theorem* based approach presented by Wang *et al.*, 1996, Clague and Wheeler, 2001. An alternative analytical solution based on Fourier

series is also provided by Morgan *et al.*, 2001a, Morgan *et al.*, 2001b. *Green's theorem* states that any two continuous scalar functions ϕ and ψ inside a volume V , having a boundary surface A satisfy the following relationship

$$\int_V dV (\phi \nabla^2 \psi - \psi \nabla^2 \phi) = \oint_A dA \left(\phi \frac{\partial \psi}{\partial n} - \psi \frac{\partial \phi}{\partial n} \right) \quad (2.25)$$

where $\frac{\partial}{\partial n}$ represents differentiation along the normal direction to the area element dA . By using *Green's Theorem*, the Laplace equation can be converted into an integral form which can provide the potential distribution for planar electrode geometry. An appropriate mathematical form of the auxiliary function, ψ , needs to be chosen to simplify the analysis. Following the approach described by Wang *et al.*, 1996, we have chosen the well known electrical potential distribution in vacuum due to a point charge located at a given distance, as our auxiliary function. For a point charge q located at a distance $r = r_0(x_0, y_0, z_0)$, Eq. 2.24 can be rewritten

$$\phi(r_0) = -\frac{1}{4\pi q} \oint_A \left(\phi \frac{\partial \psi}{\partial n} - \psi \frac{\partial \phi}{\partial n} \right) dA \quad (2.26)$$

where A is the electrode plane, assumed to be infinite, with a space V above it. The electrical potential at r_0 can be determined if the boundary conditions of ϕ and ψ are known on the planar surface A . For standing wave DEP analysis, the boundary conditions for ϕ on the electrode plane are of Dirichlet type, *i.e.*, the value of the applied ac signal is known on the electrode plane. An appropriate Dirichlet type condition can also be chosen in the gap region between two consecutive electrodes. Once the boundary conditions for ϕ is well described at the electrode plane, the auxiliary function ψ can be conveniently selected to be zero on A , so that the second term in Eq. 2.25 vanishes. The mirror-image method is employed to derive a functional form of the auxiliary function ψ which is followed by obtaining the normal derivative of ψ .

From Figure 2.6 it is understood that the electrode plane is described by the xz plane ($dA = dx dz$) and the y is the normal direction to the electrode plane. By substituting the function ψ and the normal derivative in Eq. 2.25, a

general expression for potential distribution over the planar electrode array can be obtained:

$$\phi(r_0) = -\frac{1}{4\pi} \int \frac{2z_0 \phi_{y=0}}{[(x-x_0)^2 + (z-z_0)^2 + y^2]^{3/2}} dA \quad (2.27)$$

Therefore, using *Green's Theorem* and appropriate auxiliary function, the electrical potential engendered by any planar electrode geometry can be calculated from an integral of a potential distribution function over boundary surface. Following the general formulation for potential distribution on a planar surface due to the presence of a point charge, the formulation adopted from Clague and Wheeler, 2001 will be explained for an array of parallel electrodes. This formulation utilizes a half-plane Green's function that has a different functional form than the one discussed earlier. However, for identical geometry of parallel electrodes both approach should arrive at the same solution.

As shown in Figure 2.8, the analysis starts with a set of interdigitated electrodes where the in-plane direction can be considered of infinite length compared to other two dimensions. Therefore the problem is rendered as a two dimensional system. For this analysis, the electric field is produced by applying an ac voltage to the electrodes with a phase increments of π for each consecutive electrode in the array. Here y is the vertical position above the electrode plane and x is the horizontal position along the plane. Fig 2.7 shows the location of the k^{th} midpoint (λ_k) between electrodes, the center-to-center distance between electrodes ($2d$); the leading (a_j) and trailing (b_j) edges of the j^{th} electrode, respectively.

Implementing upper half-plane Green's function as described by Clague and Wheeler, 2001, the following functional form is assumed:

$$\phi(x, y) = \int_{-\infty}^{\infty} G(x, y|\xi) \phi_s(\xi) d\xi \quad (2.28)$$

where

$$G(x, y|\xi) = \frac{x/\pi}{(x-\xi)^2 + y^2} \quad (2.29)$$

where again x and y denote horizontal position along the electrode plane and position above the plane, respectively, ξ is the position of the surface potential

along x direction. $\phi_s(\xi)$ represents the surface potential as a function of surface coordinate.

The surface boundary conditions are known in terms of the applied ac signal on the electrodes and approximation of potential in the gap region between electrodes. The potential applied to the j^{th} electrode (Figure 2.8) is given by

$$\phi_e(\xi) = V_0 \cos\left(\omega t + \frac{2\pi j}{n}\right) \quad (2.30)$$

where V_0 is the magnitude of applied rms (root mean square) voltage, ω is the frequency of the applied signal, j is the electrode identification number, and n is the mode. For this analysis, only the stationary wave DEP is of interest, and accordingly, n will be set to 2.

The surface potential in the gap between the electrodes is assumed to change linearly [Wang *et al.*, 1996], thereby ensuring continuity and smoothness of the surface potential profile between consecutive electrodes. This approximation produces results that are in accord with results obtained by application of charge density method [Wang *et al.*, 1993]. The surface potential in the gaps can be expressed as

$$\phi_g(\xi) = V_0 \left(\left[\frac{\cos_{j+1} - \cos_j}{2d - W} \right] \left[x - \left\{ \lambda_k - d + \frac{W}{2} \right\} \right] + \cos_j \right) \quad (2.31a)$$

$$\phi_g(\xi) = C_1 + C_2 x + C_3 \quad (2.31b)$$

$$C_1 = V_0 \cos_j; \quad C_2 = V_0 \left(\frac{\cos_{j+1} - \cos_j}{2d - W} \right); \quad C_3 = - \left(\lambda_k - d + \frac{W}{2} \right) C_2 \quad (2.31c)$$

where λ_k is the midpoint of the k^{th} electrode pair (Figure 2.8) and \cos_j is an abbreviated form of the term $\cos(\omega t + 2\pi j/n)$. Figure 2.7 is a schematic representation of the boundary conditions on the electrode plane; two consecutive electrodes have been applied with phase shifted ac voltage and the potential varies linearly in the gap between the electrodes.

By performing a piecewise integration of the half-plane Green's function with appropriate surface potential boundary conditions along the entire surface, the potential distribution above the electrode array can be obtained as [Clague and

Wheeler, 2001]

$$\begin{aligned}
\phi(x, y) = & -\frac{1}{\pi} \sum_{j=1}^N \phi_e(\xi) \left(\arctan \left[\frac{x - b_j}{y} \right] - \arctan \left[\frac{x - a_j}{y} \right] \right) + \\
& \frac{1}{\pi} \sum_{j=1}^{N-1} -\phi_g(\xi) \left(\arctan \left[\frac{x - a_{j+1}}{y} \right] - \arctan \left[\frac{x - b_j}{y} \right] \right) + \\
& \frac{C_2 y}{2} \left[\ln \left(1 + \left[\frac{x + a_{j+1}}{y} \right]^2 \right) - \ln \left(1 + \left[\frac{x + b_j}{y} \right]^2 \right) \right] \quad (2.32)
\end{aligned}$$

The constant C_2 in Eq. (2.31) is same as in Eq. (2.30c) for the potential in the gaps, while the terms a_j and b_j stand for the distances of the leading and trailing edges of the j^{th} electrode, respectively, from the origin of the coordinate system. N represents the number of electrodes in the planar electrode array and since the array is assumed to begin and end with electrodes, the number of gaps in between the electrodes are $(N - 1)$.

One of the limitations of this formulation is that it does not take into account the variation in electric field distribution due to presence of multiple particles. Presence of the particles will certainly modify the electric field distribution but to account for that modification would significantly complicate the analytic approach; a numerical analysis of the problem is more suitable to consider such effect. Therefore, the analysis in this study is restricted to only electric field analysis over an interdigitated electrode array. This analytic solution based on Green's function is valid for an array of electrodes that extends to infinity in both dimensions. Therefore, the accuracy of the solution for electric potential and consequently, the electric field analysis can be effected by the number of electrodes considered in the interdigitated array.

After obtaining the expression for potential distribution on and above the electrode plane, calculations of electric field components and other derivatives are performed by differentiating Eq. 2.31. These steps are carried out by using *Symbolic Math Toolbox* available in MATLAB[®] which is a high-performance language for technical computing. It integrates numerical computation, visualization, and programming in an easy-to-use environment. The expressions for

electric field components in x and y directions are:

$$\begin{aligned}
E_x = & \frac{1}{\pi} \sum_{j=1}^N \phi_e \left(\frac{y}{y^2 + [x - b_j]^2} - \frac{y}{y^2 + [x - a_j]^2} \right) \\
& + \frac{1}{\pi} \sum_{j=1}^{N-1} \phi_g(x) \left[\frac{y}{y^2 + (x - a_{j+1})^2} - \frac{y}{y^2 + (x - b_j)^2} \right] \\
& + C_2 \left(\arctan \left[\frac{x - a_{j+1}}{y} \right] - \arctan \left[\frac{x - b_j}{y} \right] \right) \\
& - C_2 y \left[\frac{x - a_{j+1}}{y^2 + (x - a_{j+1})^2} - \frac{x - b_j}{y^2 + (x - b_j)^2} \right] \tag{2.33}
\end{aligned}$$

$$\begin{aligned}
E_y = & \frac{1}{\pi} \sum_{j=1}^N \phi_e \left(\frac{x - a_j}{y^2 + [x - a_j]^2} - \frac{x - b_j}{y^2 + [x - b_j]^2} \right) \\
& + \frac{1}{\pi} \sum_{j=1}^{N-1} \phi_g(x) \left[\frac{x - b_j}{y^2 + (x - b_j)^2} - \frac{x - a_{j+1}}{y^2 + (x - a_{j+1})^2} \right] \\
& - C_2 y^2 \left[\frac{1}{y^2 + (x - a_{j+1})^2} - \frac{1}{y^2 + (x - b_j)^2} \right] \\
& - \frac{C_2}{2} \ln \left[\frac{y^2 + (x - a_{j+1})^2}{y^2 + (x - b_j)^2} \right] \tag{2.34}
\end{aligned}$$

These expressions for electric field distributions will provide electric field values at any given location over an electrode array based on a series summation for the number of electrodes considered in the planar electrode configuration.

2.3.2 Force calculation

In this subsection, polarizable particles suspended in a surrounding medium, subjected to a highly nonuniform electric field is considered to evaluate the electrical forces experienced by the particles. The formation of dipoles within the polarizable material and accumulation of charges at the interface of two dielectric materials in the presence of an electric field have already been discussed. In a uniform field net Coulomb force is zero due to the formation of equal and opposite charges on the two poles; but the net Coulomb force has a finite value if the field has varying magnitude across the region encompassed by

the particle, in other words a non-uniform electric field.

In a non-uniform electric field, a spherical polarizable particle will have regions of positive and negative charges separated by a finite distance. These two charged regions are equal in magnitude but opposite in polarity. Since the forces exerted on the two poles are different due to nonuniform electric field there will be a net force:

$$\mathbf{F} = (\mathbf{p} \cdot \nabla)\mathbf{E} \quad (2.35)$$

where \mathbf{p} is the net dipole moment as in Eq. 2.5.

In section 2.1.5, the necessary governing equation (Eq. 2.21) for DEP force in an ac field has been derived. The time-averaged dielectrophoretic (DEP) force [Pohl, 1978, Jones, 1995] acting on a single spherical particle due to a non-uniform external electrical field can be approximated in terms of dipole effects as

$$F_{DEP} = 2\pi a^3 \epsilon_m \text{Re}[K(\epsilon_m^*, \epsilon_p^*)] \nabla(\mathbf{E} \cdot \mathbf{E}) \quad (2.36)$$

where \mathbf{E} is the applied electric field, a is the particle radius, ϵ_m is the permittivity of the surrounding medium, $\text{Re}[K(\epsilon_m^*, \epsilon_p^*)]$ is the real component of the frequency-dependent Clausius-Mossotti factor (\tilde{f}_{CM})

$$K(\epsilon_m^*, \epsilon_p^*) = \frac{\epsilon_p^* - \epsilon_m^*}{\epsilon_p^* + 2\epsilon_m^*} \quad (2.37)$$

determined by ϵ_p^* and ϵ_m^* , the complex permittivities of the particle and the surrounding medium, respectively. The complex permittivity is $\epsilon^* = \epsilon - i(\frac{\sigma}{\omega})$, where $i = \sqrt{-1}$, ϵ is the permittivity, σ is the conductivity, and ω is the angular frequency of the applied field.

The term $\nabla(\mathbf{E} \cdot \mathbf{E})$ in Eq. 2.35 defines the force component engendered by the non-uniform field \mathbf{E} . Equation 2.35 implies that the DEP force is proportional to the gradient of electric field intensity, $\nabla(\mathbf{E} \cdot \mathbf{E})$, which can be expressed as a combination of the following derivatives

$$\frac{\partial}{\partial x}(\mathbf{E} \cdot \mathbf{E}) = 2 \left(E_x \frac{\partial E_x}{\partial x} + E_y \frac{\partial E_y}{\partial x} \right) \quad (2.38a)$$

$$\frac{\partial}{\partial y}(\mathbf{E} \cdot \mathbf{E}) = 2 \left(E_x \frac{\partial E_x}{\partial y} + E_y \frac{\partial E_y}{\partial y} \right) \quad (2.38b)$$

Expressions for the electric field components in both x and y directions, E_x and E_y , are given in Eq. 2.32 and 2.33. Directional derivatives of E_x and E_y can be calculated from the given analytic expressions. Utilizing these analytic form of expressions, the DEP force along the two principal directions can be written as follows:

$$(F_{DEP})_x = 2\pi a^3 \varepsilon_m \text{Re}[K(\varepsilon_m^*, \varepsilon_p^*)] \frac{\partial}{\partial x}(\mathbf{E} \cdot \mathbf{E}) \quad (2.39a)$$

$$(F_{DEP})_y = 2\pi a^3 \varepsilon_m \text{Re}[K(\varepsilon_m^*, \varepsilon_p^*)] \frac{\partial}{\partial y}(\mathbf{E} \cdot \mathbf{E}) \quad (2.39b)$$

The magnitude and the direction of the force are dependent on the electric field gradient, the size of the drops, and the dielectric properties of the dielectric particles relative to the surrounding medium.

In the following section, the nature of the electric field and the DEP force profile over a representative section of the electrode array will be discussed.

2.4 Results for Electric Field and Dielectrophoretic Force Calculation

2.4.1 Electric field and gradients of field intensity

To understand the behavior of the DEP force, a complete picture of the electric field and gradient of the field intensity is essential. Eq. 2.35 reflects the dependence of DEP force on complex dielectric permittivities of polarizable particle and the suspending medium, particle size, and gradient in field intensity as discussed in Pohl, 1978, Wang *et al.*, 1994. All the simulations described here are performed for a system comprising of water droplets suspended in decane representing a dilute water-in-oil emulsion. The physical and chemical properties used in these simulations are listed in the appendix A.

The $\nabla(\mathbf{E} \cdot \mathbf{E})$ term in Eq. 2.35 describes the non-uniform spatial distribution of the field magnitude and is important in determining the DEP effect. On the electrode array, the regions with high gradient of field intensity are of

primary interest, since the particles will experience the highest DEP force in these regions.

Figure 2.9a and 2.9b show the variations of the field intensity gradient along the x and y directions, respectively, over a small section at the center of a parallel electrode array consisting of ten electrodes. The electrode array considered for these plots has equal electrode width (W) and spacing (G), and the forces are shown over a height equal to twice the electrode width. The geometric configuration of the parallel electrode array produces an electric field that is periodic in nature. Because of the periodic nature of the field intensity gradients, analyzing the small section of the array in the middle will provide sufficient information to understand the behavior of the DEP force field over the entire length of the electrode array. The length scales in the figures are non-dimensionalized with respect to electrode width; the zero position on the horizontal scale represents the absolute mid position of the electrode array, which, in this case, is the mid point of a gap. The plots in Figure 2.9a and 2.9b depict the sharp gradients of the electric field on the edge of each electrode. It should be noted that the sharp changes in field intensity gradients occur very close to the electrode plane and decay nearly exponentially into the far field which will be discussed in detail later. Therefore, the DEP effect will have an upper bound in terms of the height to effectively influence target particles in a suspending medium. In other words, the nature and rate of the decay of DEP force in the vertical direction will dictate the design of the electrode array and the following applications.

2.4.2 Dielectrophoretic force field

An estimation of the DEP forces engendered by the standing wave ac electric fields will be undertaken in this subsection. For the present simulations, the DEP force is evaluated using the analytic expression for the electric field gradients in Eq. 2.37a and 2.37b, over an array of 40 parallel electrodes. The x and y components of the electric field intensity gradients and consequently, the DEP forces are evaluated by employing series summation as mentioned before. Since

the DEP force is proportional to the field intensity gradients, the force profile exhibits similar dependence on electrode width, spacing, and applied voltage as the field intensity gradients. As is evident from Eq. 2.35, the particle size and frequency dependent Clausius-Mossotti factor have significant effects on the DEP forces. The variation of polarizability of suspended particles depending on the frequency of applied electric field and effect of the particle size has been extensively discussed in the literature [Green and Morgan, 1998]. In this analysis, first the effect of frequency on DEP force is studied over a small frequency range, 600 Hz - 2 kHz, within which the DEP force remains attractive for the system modelled here, namely, water-in-decane system.

The results are shown in Figure 2.10, where the total DEP force adjacent to the electrode plane is plotted for different frequencies of the applied voltage. It is observed that the DEP force tends to decrease slightly with increasing frequency of the applied field. The mid-plane of the gaps are the only regions over the electrode plane where the DEP force is substantially affected by variation of the frequency.

The DEP force profile displays sharp changes along the length of the electrode array. Figure 2.11 shows the DEP force distribution at the middle of a 40-electrode array. The surface plot in Figure 2.11 is generated from a simulation with 40-electrode array, where an ac voltage of 50 V at 600 Hz was applied to the electrodes to emulate standing wave DEP force field. Both the electrode width and gap in the array were taken to be 50 μm , and the forces were obtained over a domain height of 100 μm from the electrode plane. The actual DEP force in Figure 2.11 is nondimensionalized as $F_{DEP}W/kT$, where F_{DEP} is the actual DEP force, W is the electrode width, k is the Boltzmann constant, and T is a reference temperature (room temperature in these simulations). The sharp peaks in the DEP force occur at the edge of each electrode, coinciding with the location of the high field intensity gradients. Furthermore, although the forces become quite small near the mid points of the electrodes and the gaps, the magnitude of the residual force is higher at the gap mid-point compared to

the middle of the electrode.

Figure 2.12 shows the decay behavior of the DEP force at different locations on the electrode and the gap for the 40 electrode array. The horizontal axis in this plot shows the vertical distance over the electrode plane, which is non-dimensionalized with respect to the electrode width. It is interesting to note that the decay is exponential at the middle of the electrode spacing whereas at the edge of the electrode, the DEP force actually increases over a small distance from the electrode before it starts to decay exponentially. At a distance of about $75 \mu\text{m}$ from the electrodes, the decay behavior appears to be almost identical irrespective of horizontal location on the electrode plane. An approximation for the far field decay behavior of the DEP force over a parallel electrode array is provided elsewhere [Green *et al.*, 2002b].

The magnitude of the applied voltage alters the DEP force significantly. A detailed analysis of the dependence of DEP force on the electric field intensity gradient is provided by Clague and Wheeler, 2001, which shows that the gradient of field intensity is proportional to the square of applied rms voltage. Figure 2.13 shows the dependence of DEP force on applied voltage near the center of a 40 electrode array. The locations of two electrodes are shown on the horizontal axis. Increasing the applied voltage from 50 to 250 V results in an order of magnitude increase in the magnitude of the DEP force near the electrodes. The force profiles depict that for most of the electrode plane barring the regions near the mid-points of the electrodes, the DEP forces typically range from 10 pN (pico- Newtons) to 10 nN (nano-Newtons). These forces are substantially large compared to typical electrokinetic forces observed in dc electrokinetics, namely, the electrostatic double layer forces, which usually range from 1 to 10 pN. Consequently, a colloidal size particle can migrate more rapidly under the influence of ac dielectrophoretic forces.

2.5 Dielectrophoretic Force Calculation: Finite Element Analysis

Analytical methods provide exact solutions of the electric field gradient at any point in space on the electrodes in an array. However, it is only useful when considering a limited number of simple electrode geometries (mainly 2D). The majority of electrode configurations do not conform to these simplified models. Even if the real electrodes resemble the structures considered in the analytic formulation, they are usually constructed using thin film technology and are far from being represented by infinitely long (2D) models, the complex electric field morphology varies in magnitude and may be in phase in all three dimensions. It is often not feasible or possible to derive analytical expressions for the field for complex geometries. Therefore, we resort to numerical analysis to employ approximation methods to simplify the problem and obtain approximately accurate solution for an arbitrary arrangement of electrodes.

2.5.1 Finite element formulation

Here the analytic solution for the DEP force field is compared with a finite element solution for identical set of parameters. Finite element analysis of dielectrophoretic and travelling wave forces enables simulations for different types of geometries and arbitrary configuration of electrodes. This can potentially aid in the process of determining the optimal electrode configurations to achieve the maximum effects of dielectrophoresis. Recently, simulations of DEP forces based on this approach have been proposed in the literature [Green *et al.*, 2002*b*].

Finite element method was originally developed for solving mechanical stresses in civil engineering, but was later adopted for calculating electric fields [Zienkiewicz, 2000]. As in many other numerical techniques, the solution space is divided up into a series of nodes that define the corners of enclosed elements. Unlike in finite difference method, these elements need to loosely follow a general shape such as cuboid or tetrahedron. As long as the element has appropriate

number of corners and faces, it does not need to conform to the shape too rigidly. The element is transformed locally onto a rigidly defined master element and the Poisson's equation is approximated linearly across that element. Potential across each element is determined and then recombined to determine the potential across the whole computational geometry. The results are mapped onto a system matrix and solved as a series of simultaneous equations to determine the overall electric field. Boundary conditions are mapped as defined potentials at the appropriate nodes. Since the electric field is approximated to be linear across each element, most finite element models use automated meshing techniques to ensure that the elements are small in the regions where the electric field is changing the most, such as at the electrode edges.

Finite element method is now widely used for electric field calculations. Many commercial packages are available with finite element solvers, design modules for defining the model and postprocessing programs for data analysis.

2.5.2 Model description

The finite element solution has been obtained based on a 2D Cartesian framework over a parallel electrode array. The computational geometry is depicted in Figure 2.14. Since the electric field engendered by the electrode array and consequently the DEP force profile is perfectly periodic, a small representative section of the array has been focused to obtain numerical solution. The bottom boundary in the schematic shows the arrangement of two consecutive electrodes and the gap in between. All the lengths are normalized with respect to electrode width (W). The gap (G) between the electrodes is considered to be equal to the width (W) of the electrode and in the vertical direction the height of the computational domain is assumed to quite large ($4W$), compared to the range of the effective range of DEP force distribution. The applied potentials on the boundaries are also normalized by amplitude of the applied ac voltage (V_0). Assuming no free charges exist in the system, the finite element model solves the *Laplace* equation to obtain electric potential distribution above the

electrode plane.

$$\nabla^2 \phi = 0 \quad (2.40)$$

where ϕ is the electric potential applied to the electrode array. The time dependent electrode and gap potentials given by Eqs. 2.29 and 2.30 are employed as boundary conditions on the electrode plane.

$$\phi = \phi_e/V_0, \quad \partial\Omega \in W \quad (2.41a)$$

$$\phi = \phi_g/V_0, \quad \partial\Omega \in G \quad (2.41b)$$

where ϕ_e and ϕ_g are the applied potentials on the electrode and gap region as in Eqs. 2.29 and 2.30, respectively and $\partial\Omega$ represents the bottom boundary of the computational domain. The electric potential on the top boundary is assumed to be zero (grounded) since the top boundary is assumed to be far away from the electrode plane where the potential distribution is expected to diminish to zero. Potential distribution in the gap between two consecutive electrodes varies linearly as described by Eq. 2.30 and attains zero value exactly at the midpoint of each gap. In reality, the potential function is defined by surface charge density on the surface and will not be linear. The linear assumption is used in this analysis only for a comparative study of the analytic solution with the numerical results. At the inlet and exit planes that represent the midsection of the gap regions in this geometry, the electric fields are assumed to be uniform (symmetry condition). With these boundary conditions, the Laplace equation is solved over the computational domain to predict the spatial variation of the electric potential and field distributions.

2.5.3 Discretization

The domain of interest is meshed using quadrilateral elements with increasing mesh density near the electrode edges and surfaces to account for high field gradients in these regions. The model uses 2D quadratic elements for calculation of electric potential and field distribution inside the domain. The scope of using

unstructured/free mesh and mapped mesh with same type of mesh distribution in the domain has been explored. It has been observed that same level of numerical accuracy can be achieved by employing mapped mesh scheme with even less number of elements than in case of a free mesh. Structured or mapped meshing breaks up the region to be meshed into a series of smaller rectangular regions where rows and columns of elements can be generated. This allows the flexibility of controlling how the region is meshed, by manually choosing number of subdivisions on the lines that bound the computational domain.

In case of a mapped mesh element, aspect ratio (ratio of longest dimension to the shortest dimension) is of serious concern inside the computational domain. For each element, as the aspect ratio becomes large the elements becomes long and skinny. In a finite element analysis a small mesh size is normally required in regions of high field gradients, *i.e.*, regions where large variation of electric field is observed. Since the electric field decays over the electrode array and exhibits sharp gradients near the edges of the electrodes, smaller mesh elements are absolutely necessary near the electrode edges. However, same type of mesh density in the far field region will be redundant; simply because the far field calculations will not be seriously effected by the use of elements with high aspect ratio. Therefore, a structured mesh scheme was employed that uses high mesh density with low aspect ratio near the electrode plane where the DEP force calculation is significantly effected by the number of elements and mesh quality due to high electric field gradient. The size of the elements progressively increases away from the electrode plane and the aspect ratio of the elements near the top boundary becomes reasonably high as the elements tend to be slender in that region. Careful choice of element size, near the regions where high field gradient is anticipated, is very important to produce reliable results when use of structured mesh is intended.

2.5.4 Finite element solution

To ensure convergence of the numerical solution, electric field values in the region of high field gradient are compared with the results from the analytic method. Based on the field distribution, DEP force calculation is performed using Eq. 2.38 in a plane at a given height over the electrode plane. Noting that the Laplace equation has no dependence on time, the solution is based on the assumption that the electrical fields are instantaneously developed depending on the transient variations of the electrode and gap potentials. In other words, the transient nature of the electric fields exactly follows the periodic nature of the voltage fluctuations on the electrodes, dictated by the frequency of the ac signal. The finite element model was implemented using commercial finite element software, ANSYS®. A built-in quadratic element, PLANE 121, from the ANSYS element library has been used for modelling the electrical problem. This element is generally used to model 2D electrostatic problems. The simultaneous equations generated by finite element procedure are solved using direct elimination solver.

2.5.5 DEP force estimation and convergence

By introducing simplifying conditions in the numerical analysis of the physical problem, errors are introduced in the solution. For example, the discretization of otherwise continuous functions in the computational incorporate some level of error in the solution. The nature of these errors depend on the approximations used in the process.

The numerical and analytical results obtained under identical sets of boundary conditions are compared in this section. These results represent latex-in-water system, where the dielectric permittivity of the particle is much smaller than the solvent permittivity. As discussed earlier latex particles may experience either positive or negative DEP force in the same system depending on the frequency of the applied ac signal. Both cases have been simulated for the same system at two different frequency ranges, on either side of the crossover fre-

quency (Figure 2.5) for latex-in-water system. As discussed earlier, the crossover frequency is influenced by the electrical properties of the two dielectric materials in the system. It should be noted that the range of applied frequency, where this system exhibits positive DEP phenomena (around 15 Hz) is extremely low and therefore can cause severe electrode polarization in real applications. However, the higher end of the frequency range for a negative DEP force field can be increased significantly to avoid the problems associated with low frequency applications.

Figure 2.15 shows the effect of number of mesh elements on the numerical computation. The vertical axis represents the L2 norm of numerical solution obtained for negative DEP force compared to the analytic results. By utilizing the periodicity of the force profile, a set of data over a periodic segment of the array were used, to calculate the error in numerical calculation. In this small region, force values obtained from finite element calculation for increasing number of mesh elements were compared to the analytic results at same spatial locations. The numerical solution for DEP force was normalized by analytic force value at each data point and the norm was averaged over the number of data points used in the representative region of the electrode array. As can be seen from Figure 2.15, the calculated norm decreases exponentially, with an increase in number of elements used in the finite element analysis of the problem. The finite element analysis for these comparisons were based on a free mesh scheme, where the mesh was refined gradually near the electrode plane and DEP force was calculated after each cycle of mesh improvement. It is evident from Figure 2.15 that the finite element solution reaches an optimum condition with around 20,000 elements and further mesh refinement does not effect the result significantly. An increase in number of elements may improve the results marginally but at the cost of increased computational time.

In this study, it was found that by employing a mapped mesh with appropriately chosen element length near electrode edges, can produce highly accurate force field with fewer number of elements than in case of free mesh. Therefore,

a mapped mesh was used for the following comparison of electric field and DEP forces. For the same set of parameters, the two methods produce results that are in good agreement as shown in Figures 2.17a and 2.17b. Figure 2.16 depicts the distribution of the electric field ($-\nabla\phi$) over a periodic region spanning two consecutive electrodes. The non-dimensional field is obtained by multiplying the actual electric field value with a factor W/V_0 where W is the width of each electrode in the array and V_0 is the amplitude of the applied voltage. The analytic result is shown by the solid line, in the plot while the numerical result is given by the symbols. Both techniques produce electric field profiles that are almost identical. Electric field values from both analytic solution and numerical method match with high accuracy. Predictions of the DEP force are compared for identical set of parameters in Figure 2.17a and 2.17b, for positive and negative DEP force fields, respectively. First in Figure 2.17a, the applied voltage is 50 V and the applied frequency is low enough (10 Hz) to create positive DEP phenomena in the latex-in-water system. The analytic result shown by solid line in the force profile is slightly higher than the numerical solution presented by the symbols. In Figure 2.17b the same system is modelled with a higher value of frequency (600 Hz) of the applied ac signal to simulate negative DEP force field.

It is evident from Figure 2.5, that the value of the real part of the Clausius-Mossotti factor goes through a change of sign on either side of the crossover frequency. The peak value of DEP force in case of negative DEP is significantly larger than that observed in positive force field. This can be attributed to the higher magnitude of the real part of the Clausius-Mossotti factor in the latter case. In both the simulations, the two predictions match closely over the entire domain, except at the sharp peaks observed at the electrode edges. This is an artifact of the numerical procedure for evaluation of the spatial derivatives. The sharp peaks are missed in the calculation of the derivatives by interpolation of the basis functions in the finite element analysis. This limitation can be avoided by carefully choosing the integration limits to coincide with the electrode edges,

and employing piecewise continuous functions. However, such a procedure cannot be applied in a general implementation of the numerical code, since the periodic nature of the functions and the locations of their discontinuities cannot be assessed a priori during the numerical solution.

2.6 Summary

In this chapter, the physical phenomena of dielectrophoresis has been discussed in the context of origin of the electrokinetic forces. Correct form of the analytic solution is derived for the non-uniform electric field distribution over a simple interdigitated microelectrode array. This analytic solution is later used to evaluate standing wave DEP force engendered by a parallel electrode array. The basic governing equations of DEP force on a polarizable particle suspended in a dielectric medium, under the action of a non-uniform ac electric field have also been discussed. The frequency dependent behavior of the complex polarizability and DEP force have been discussed. Also the DEP force is highly dependent on the electrical properties of the particle and the suspending medium, particle volume and proportional to the square of electric field intensity. A numerical approach based on finite element method has been discussed, to evaluate the electric field distribution for any arbitrary geometry in general. The analytic expression described in this chapter will be utilized in the following chapters, to study the effect of non-uniform electric field on different types of dielectric systems.

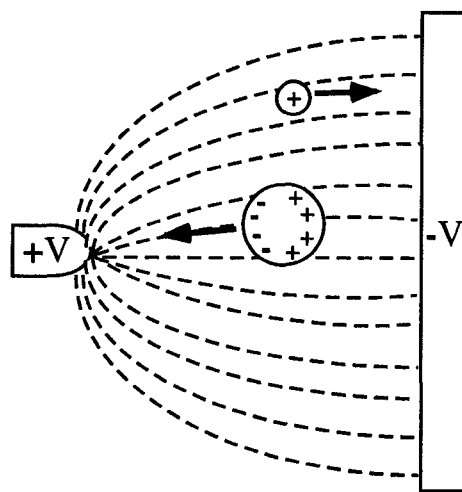
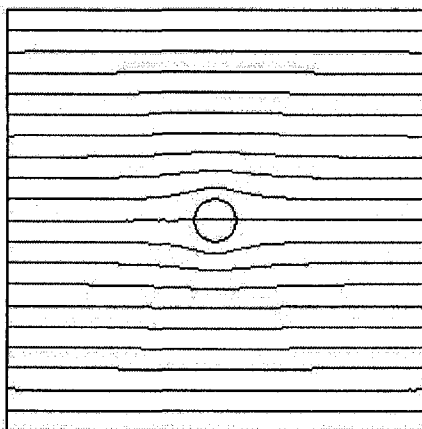
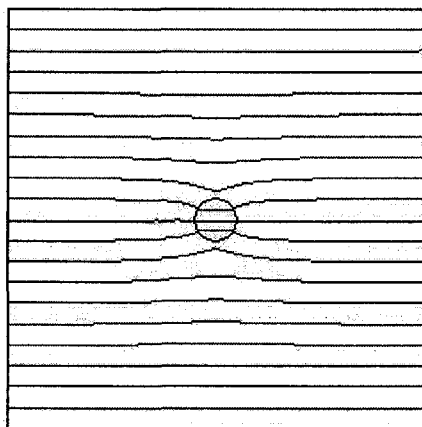


Figure 2.1: Schematic diagram showing the movement of a charged body (small sphere) and a polarized neutral body (large sphere) in a non-uniform electric field. The dotted lines represent the electric field lines.



(b)

Figure 2.2: (a) Electric field lines around a particle with polarizability higher than the surrounding medium. (b) Electric field lines around a particle with polarizability lower than the surrounding medium.

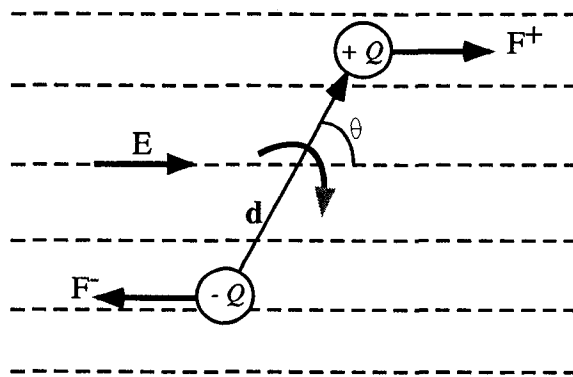


Figure 2.3: Schematic diagram showing a dipole in a uniform electric field. F^+ and F^- represent the electrical force acting on the charges due to the electric field.

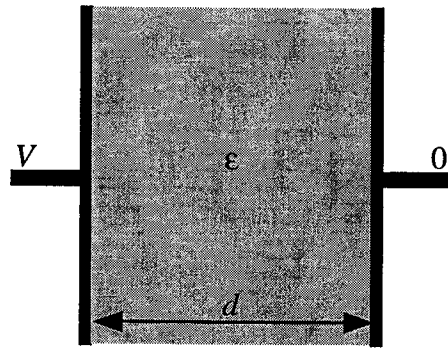


Figure 2.4: Schematic diagram showing a dielectric medium with a permittivity, ϵ , under an electric field.

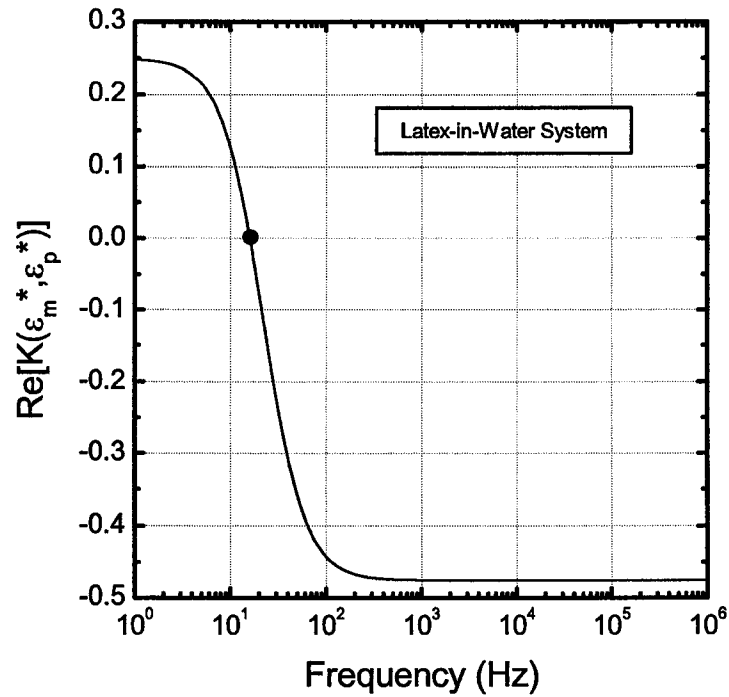


Figure 2.5: Plot of real part of frequency dependent Clausius-Mossotti factor for latex-in-water system against frequency of the applied ac signal. ϵ_p^* and ϵ_m^* represent the complex permittivity of particles and surrounding medium, respectively. The electrical properties of the particle and medium are listed in table A1 in the appendix.

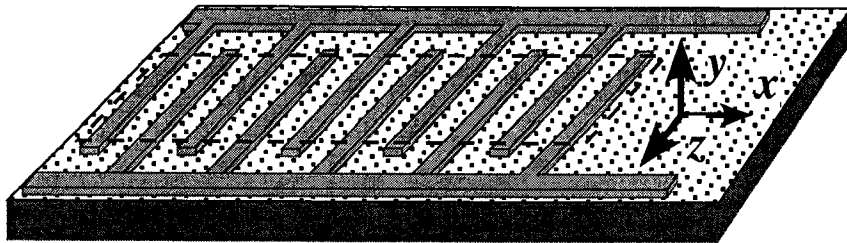


Figure 2.6: Schematic diagram of interdigitated electrode array with the region of interest marked by dotted line.

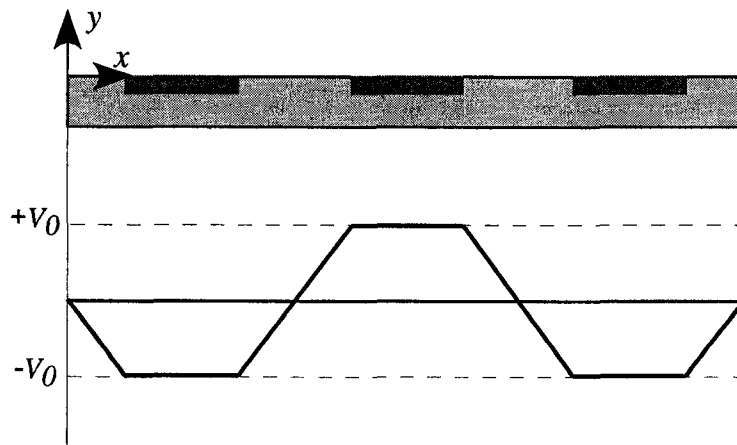


Figure 2.7: Schematic diagram of applied potential distribution on the electrode plane for stationary wave DEP.

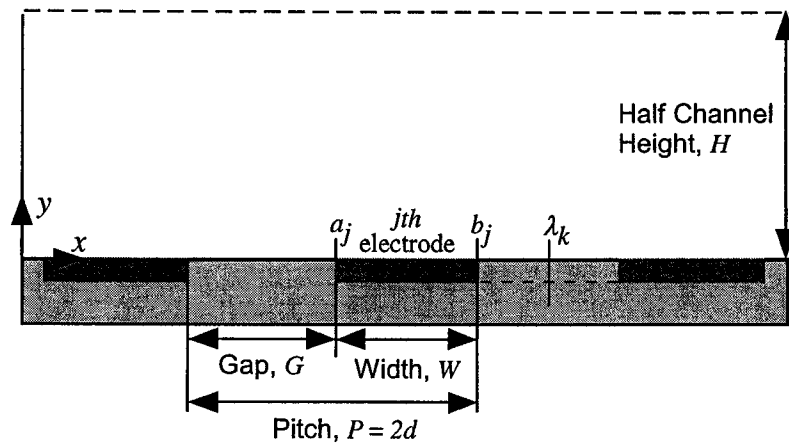
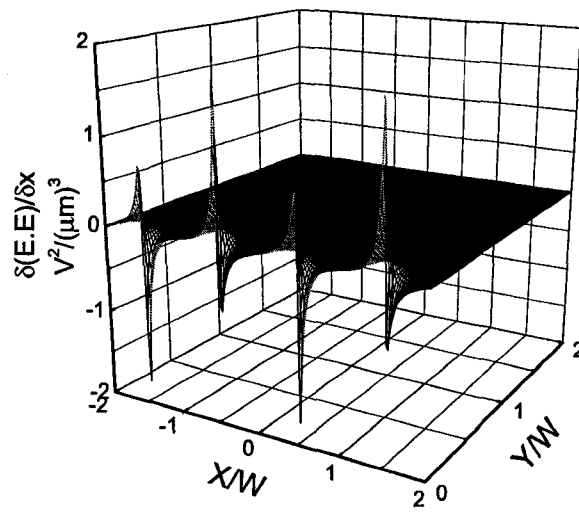
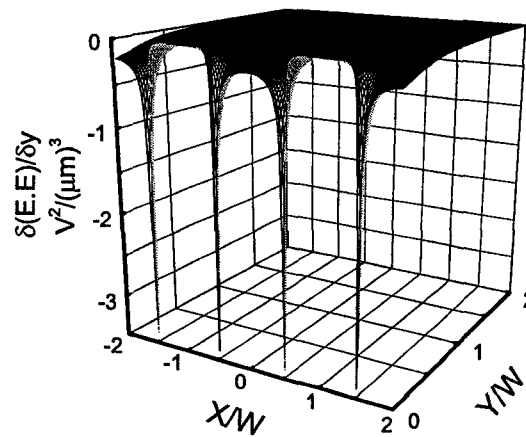


Figure 2.8: Schematic diagram showing the coordinates and the electrode configuration. a_j and b_j are the leading and trailing edge of the j^{th} electrode. λ_k is the midpoint of k^{th} pair of electrode.



(a)



(b)

Figure 2.9: (a) Surface plot showing the electric field gradient in the horizontal direction over the electrode plane. The horizontal and vertical axes in this plot are non-dimensionalized with respect to electrode width, which is $50 \mu\text{m}$ in this case. In this electrode configuration, gap between two consecutive electrodes is equal to the width of each electrode. Applied voltage, $V = 50 \text{ V}$ and frequency, $\omega = 600 \text{ Hz}$. (b) Surface plot showing the electric field gradient in the vertical direction over the electrode plane under same conditions as in the previous case.

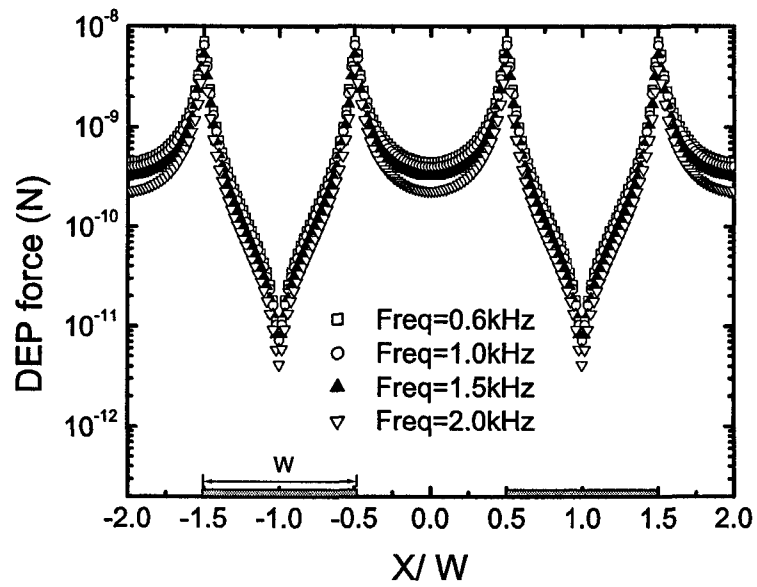


Figure 2.10: Dependence of total DEP force on applied frequency. The horizontal axis in this plot is non-dimensionalized with respect to electrode width, which is $50 \mu\text{m}$ in this case. Gap between electrodes is equal to electrode width. Applied voltage, $V = 50 \text{ V}$.

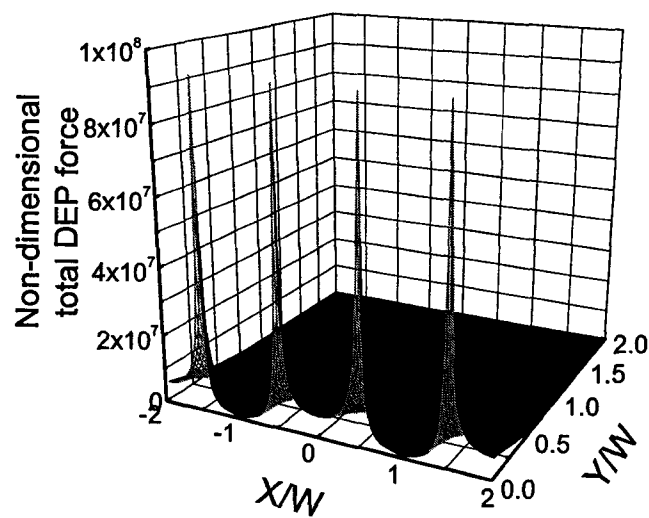


Figure 2.11: DEP force distribution over the electrode plane. The horizontal and vertical axes in this plot are non-dimensionalized with respect to electrode width, which is $50 \mu\text{m}$ in this case. Gap between electrodes is equal to electrode width. Applied voltage, $V = 50 \text{ V}$ and frequency, $\omega = 600 \text{ Hz}$. The DEP force is non-dimensionalized with respect to electrode width, Boltzmann constant and temperature, *i.e.*, the non-dimensional force is $F_{DEP}W/kT$.

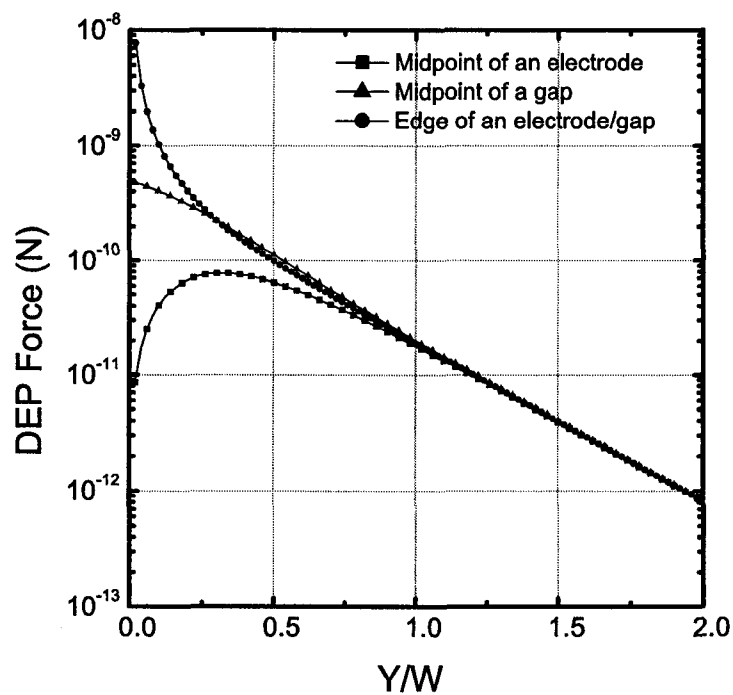


Figure 2.12: Variation of total DEP force with distance from the electrode plane at different axial locations. The horizontal axis in this plot is non-dimensionalized with respect to electrode width, which is $50 \mu\text{m}$. Gap between electrodes is equal to electrode width. Applied voltage, $V = 50 \text{ V}$ and frequency, $\omega = 600 \text{ Hz}$.

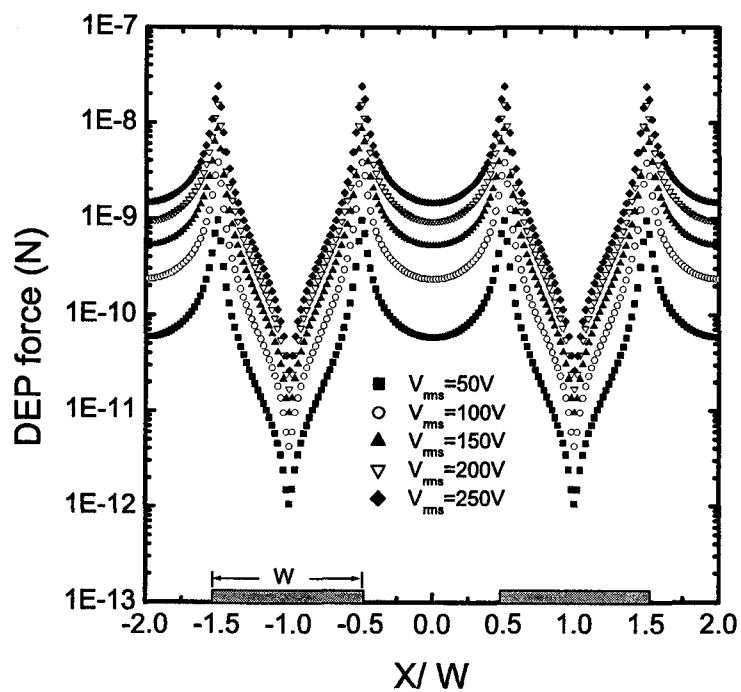


Figure 2.13: Plot showing the dependence of total DEP force near the electrode plane (at $1 \mu\text{m}$ from the electrode plane) on applied voltage. The horizontal axis in this plot is non-dimensionalized with respect to electrode width, ($50 \mu\text{m}$). Gap between electrodes is equal to electrode width. Applied voltage, V varies from 50 V to 250 V. Applied frequency, $\omega = 600 \text{ Hz}$.

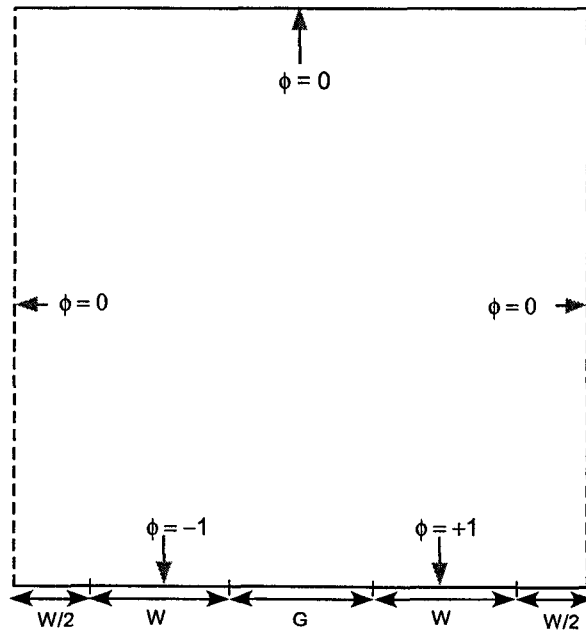


Figure 2.14: Schematic diagram of the finite element model with boundary conditions. A representative segment of the electrode array is shown here. W and G are the width of the electrodes and gap between two consecutive electrodes on the parallel electrode array, respectively. ϕ is the applied electric potential on different parts of the boundary. $|\phi| = 1$ is scaled potential applied to the electrode surface, scaled with respect to V_0 , amplitude of the applied ac signal. All the lengths are scaled with respect to electrode width (W) and the gap (G) between electrodes is assumed to be equal to the width of electrode.

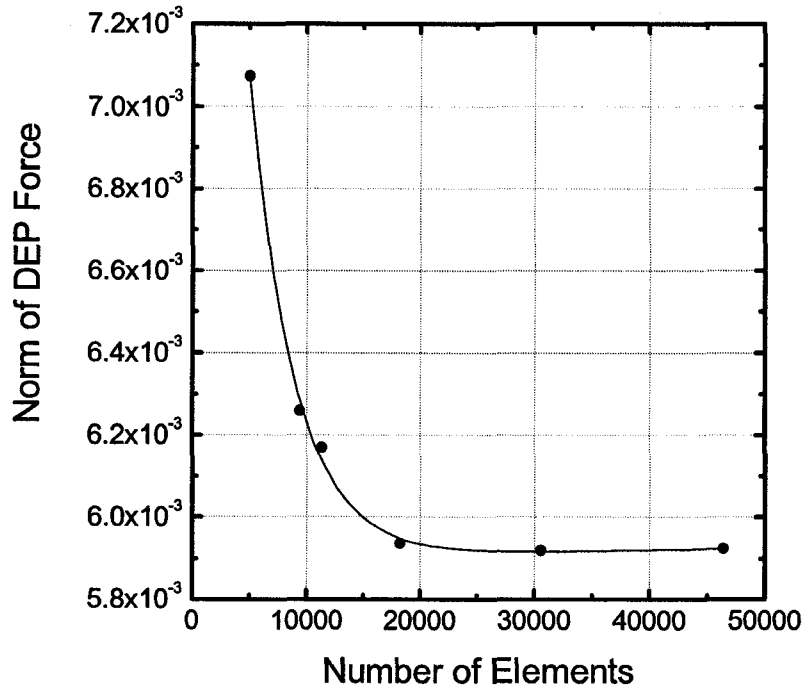


Figure 2.15: Plot showing norm of total DEP force with variation of number of elements used in the finite element analysis. DEP force evaluation was performed for a geometry shown in Figure 2.14. Norm was calculated over a periodic segment of the electrode array and averaged over 1600 data points evenly distributed on the segment. For each element specification, norm is defined as $(1/N) \sum (1 - F_{num}/F_{anal})^2$, where, N is the number of data points, F_{num} is the numerical value of the DEP force and F_{anal} is the analytic solution at each of the N points on the segment. The analysis was done for a latex-in-water system with applied voltage of 50 V and frequency of 600 Hz. The electrode width and gap are equal to 50 μm .

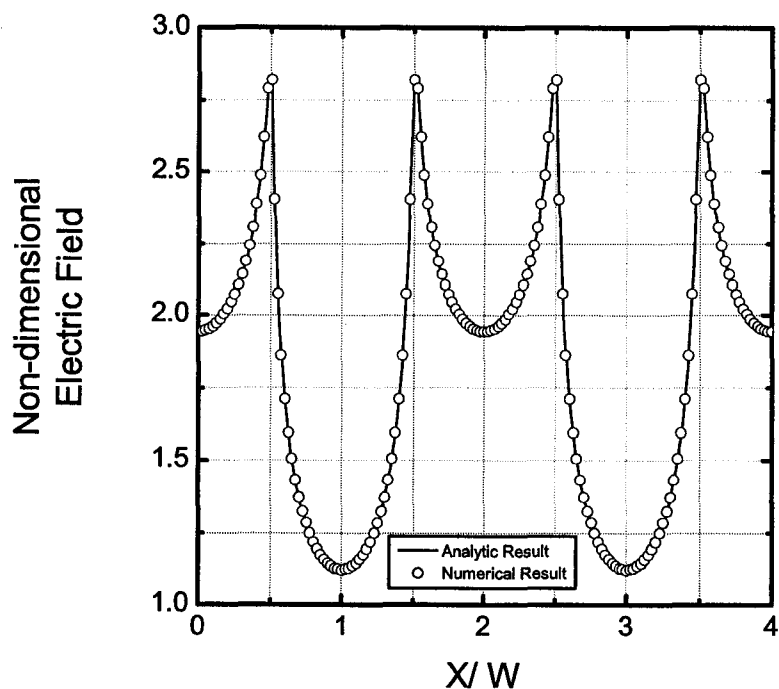


Figure 2.16: Comparison of non-dimensional electric field values from analytic approach and numerical solution. The horizontal axis is nondimensionalized with respect to electrode width (W) and the non-dimensional electric field is obtained by multiplying actual field values with a factor W/V_0 , where W is the width of each electrode in the array and V_0 is the amplitude of the applied voltage. Electrode width and gap equal to $50 \mu\text{m}$ and the applied voltage is 50 V at a frequency of 600 Hz.

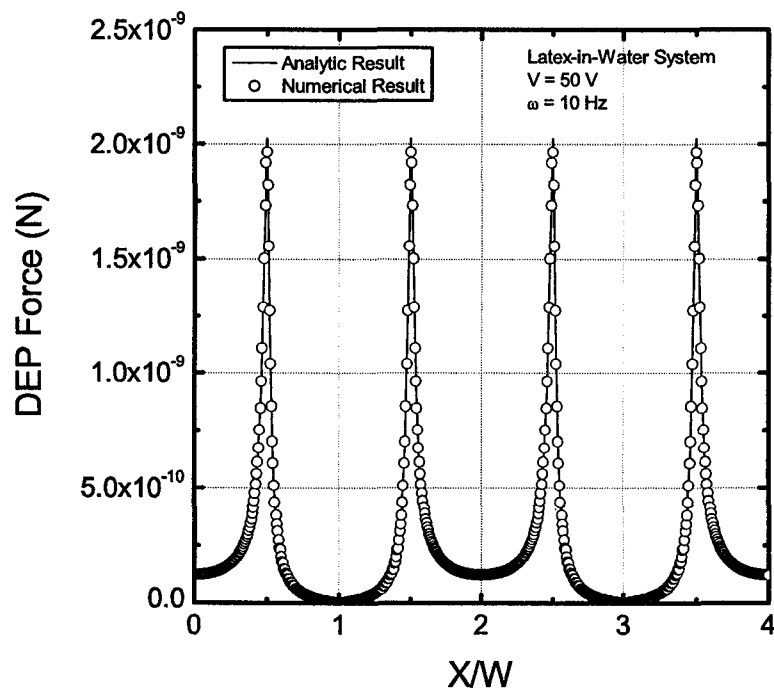


Figure 2.17a: Comparison of total positive DEP force values from analytic approach and numerical solution in latex-in-water system. The horizontal axis is nondimensionalized with respect to electrode width (W) and vertical axis contains the actual DEP force values. Electrode width and gap equal to $50 \mu\text{m}$ and the applied voltage is 50 V at a frequency of 10 Hz that corresponds to the positive value of the real part of frequency dependent Clausius-Mossotti factor for latex-in-water system.

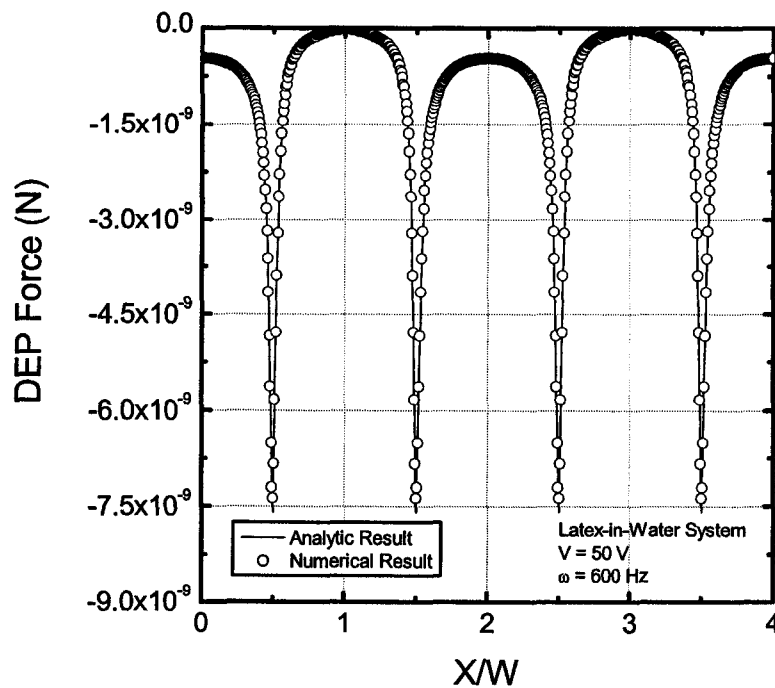


Figure 2.17b: Comparison of total negative DEP force values from analytic approach and numerical solution in latex-in-water system. The horizontal axis is nondimensionalized with respect to electrode width (W) and vertical axis contains the actual DEP force values. Electrode width and gap equal to $50 \mu\text{m}$ and the applied voltage is 50 V at a frequency of 600 Hz that corresponds to the negative value of the real part of frequency dependent Clausius-Mossotti factor for latex-in-water system.

Chapter 3

Trajectory Analysis of Crossflow Membrane Filtration

3.1 Introduction

Membrane based processes utilize a semi-permeable barrier (membrane) with an external driving force, typically pressure, to selectively transport certain components of a mixture across the membrane. Large scale membrane separation processes are widely used in water and waste water treatment, biomedical applications, food processing, and a variety of industrial separation and purification processes. Reliability, compactness, low maintenance, and low cost makes membrane processes feasible and attractive for many large scale industrial applications [Mulder, 1996].

In a typical pressure driven membrane process, the magnitude of the driving force determines the extent of separation of the target components to the permeate side of the membrane while the other components are retained. An ideal membrane is expected to have high selectivity, high permeability and mechanical stability. The membrane should also demonstrate chemical stability, *i.e.*, resistance to fouling or degradation.

Long term operation of a membrane module can cause deterioration of the separation process efficiency. Typical problems encountered are flux decline and membrane fouling. Flux decline is defined as the decrease in permeate flux

over time due to increasing resistance to flow and decrease in effective pressure difference. These problems can be addressed by incorporating a flow of the feed solution across the membrane surface - generally known as crossflow membrane filtration. In crossflow filtration, rejected solutes are continuously carried away from the membrane surface, thereby minimizing solute buildup.

With the continued operation of a membrane, rejected solutes build up a concentrated layer near the membrane surface - a phenomena known as concentration polarization. Due to concentration polarization, different resistances towards solvent permeation increase with time, thereby slowly reducing permeate flux. Various forms of resistance, such as, formation of cake layer, scale formation on the membrane surface, pore blocking due to entrapment of particles, and adsorption of solutes may contribute significantly to the decline of permeate flux. Furthermore, concentration polarization near the membrane surface can cause reduction in effective pressure difference across the membrane, due to osmotic pressure buildup, resulting in flux decline.

The primary goal of this study is to couple ac dielectrophoresis with crossflow membrane filtration to address two issues pertaining to this technology. First, positive DEP force will be used to preferentially attract a target species toward the membrane and enhance it's separation. Secondly, negative DEP will be utilized to prevent colloidal entities from coming in contact with the membrane, thereby reducing it's fouling potential. Both these aspects of the study fundamentally rely on the transport behavior of colloidal entities in crossflow membrane filtration, in presence of various forces (electrical, hydrodynamic, colloidal, Brownian etc.).

Majority of the studies on solute transport in membrane filtration employ a continuum (Eulerian) approach, which involves solving the governing Convection-Diffusion equation [Bakewell and Morgan, 2001], to obtain the solute concentration distribution in the module. In the present study, a trajectory analysis is employed to assess the transport phenomena. The primary reasons for this mode of analysis are simplicity and ability of obtaining a detailed map

of the trajectories of non-Brownian particles in presence of various forces.

In a dilute system, the movement of each particle can be described by using a Lagrangian approach. The position of a single particle can be determined by considering the active forces on the particle, namely, deterministic forces, fluid drag and forces causing random Brownian motion. This formulation is referred to as *Langevin* equation because of the presence of Brownian motion term [Langevin, 1908]. Since the inter-particle interaction can be neglected in a dilute system, the Lagrangian approach can predict the path of the particle in a suspending medium with reasonable accuracy. This trajectory analysis for an isolated particle is rather straightforward to implement but is a good indicator of the particle behavior in a given system.

In this chapter, the pertinent particle transport model is developed, which will enable exploration of the effect of DEP on enhancement of separation effectiveness, as well as, on minimization of membrane fouling. The movement of particles close to the membrane surface can be significantly affected by the fluid flow field in that region. The trajectory model developed here can also be employed to gain an understanding of the effect of near-membrane fluid velocities in dielectrophoretic crossflow membrane filtration process.

3.2 Model Description

A mathematical model has been developed to explore the different aspects of the membrane separation process, under the action of a deterministic force field, like the dielectrophoretic (DEP) force in this work. The model is constructed based on the flow of a colloidal suspension through a channel that has a porous bottom wall. The bottom wall is considered to be embedded with an interdigitated microelectrode array that creates the DEP force field.

Figure 3.1 depicts a schematic representation of the setup to be considered for the simulation of dielectrophoretic membrane filtration based separation process. As indicated in Figure 3.1, the channel under consideration is rectangular

with a height $2H$ and the bottom surface of the channel is a membrane, embedded with an array of interdigitated electrodes. The array consists of electrodes of same width (W) with equal or larger spacing (G) in between the electrodes. Since the depth of the channel is significantly larger than the electrode dimensions, the model is rendered in a two dimensional Cartesian system. For the simulations presented here, the electrode surfaces are considered to be coated with a layer of low dielectric material to avert short-circuiting of the electrodes. This coating should be sufficiently thin so as not to significantly attenuate the electric field.

In the simulations of dielectrophoretic membrane filtration in a tangential flow (crossflow) system, the suspension containing the target species approaches the electrode plane with an initial concentration and flows across the channel length with an average velocity governed by the axial volumetric flow rate. As the emulsion flows over the electrode array, the dielectrophoretic force field acts on the target species to either attract or repel them from the membrane surface.

3.3 Trajectory Analysis

A trajectory model has been formulated to understand the behavior of the suspended particles inside the channel. This model is used to track the migration of a single polarizable particle in a non-uniform electric field while suspended in a dielectric medium. The trajectory of each particle is obtained under the combined effect of electrical and hydrodynamic forces. The fluid flow field analysis, necessary to account for hydrodynamic influence, will be described in the following section. Appropriate DEP forces are incorporated into the model from the analytic solution for a given length of the electrode array as described in the previous chapter.

In this section, the formulation to track the motion of the target species inside the flowing medium under DEP effect will be explained. The target species

is modelled as ideal spherical particles and neutrally buoyant. The particles are assumed to be sparsely distributed in the flow and are non-interacting. Consequently, constant properties of the particles are assumed, and any particle-particle interaction in the bulk medium arising from local modifications of the electrical field distribution is neglected. The physical parameters such as viscosity and bulk density are taken to be that of the suspending medium. Brownian motion and gravity effects on the suspended particles can be neglected for micron size particles.

In general, when a particle is moving relative to the surrounding fluid, it experiences a viscous drag due to the action of the fluid on the particle. This drag force fu is proportional to, and acts against the relative velocity of the particle, where f is the friction factor and u is the particle velocity [Hiemenz, 1986]. The friction factor is related to the size, shape and surface characteristics of the particle. When the particle is suspended in a fluid and accelerated by a deterministic force, it experiences an increasing drag force and at some point the two opposing forces counterbalance each other. The particle reaches a terminal velocity beyond which it does not accelerate and which also depends on the fluid velocity. The particle velocity can be obtained by balancing *Stokes drag* force and the deterministic force which is DEP force in this case.

$$F_{DEP} = fu = 6\pi\mu au \quad (3.1a)$$

$$u = \frac{F_{DEP}}{6\pi\mu a} \quad (3.1b)$$

where a is the particle radius and μ is the viscosity of the suspending medium. The factor $6\pi\mu a$ is the Stokes-Einstein drag coefficient on a smooth spherical particle of radius a . The velocity components in horizontal and vertical directions can be evaluated by considering dielectrophoretic forces in those directions. This approach, however, does not provide sufficient details about the particle trajectories very close to the channel walls, since the hydrodynamic interactions are not considered in Eq. 3.1. Consequently, a more rigorous trajectory model that accounts for the hydrodynamic interactions is developed, to track

the trajectories of the particles accurately as they approach the electrode plane.

Since the effect of dielectrophoretic force fades out as one moves away from the electrode plane, the particles near the electrode-bearing wall (which is also permeable when the electrodes are on the membrane) will experience the maximum attractive force. This effective region is considerably small compared to the channel height but can be modified by manipulation of the electrical forces. Therefore, the simulations were focused on a narrow region near the bottom wall of the channel (similar to the thickness of a concentration boundary layer). The velocity of the particles in the fluid flow can be defined as [Elimelech *et al.*, 1995]

$$u_{\parallel} = f_3 v_{\parallel} = f_3 v_x \quad (3.2a)$$

$$u_{\perp} = f_1 f_2 v_{\perp} = f_1 f_2 v_y \quad (3.2b)$$

with u_{\parallel} and u_{\perp} being the velocity components of a particle in the axial and vertical directions, respectively. v_x and v_y are the components of fluid velocity in axial and transverse directions inside the channel, respectively. The terms f_1 , f_2 , f_3 are the universal hydrodynamic correction factors to account for the modification of velocity of particles near the planar surface and are calculated based on non dimensional separation distance, h/a , where h is surface to surface separation distance. Tabulated values for these factors can be found from Masliyah, 1994.

Neglecting other forms of particle interactions, the particles are subjected to only hydrodynamic force and the dielectrophoretic force. The random forces arising from thermal energy of the system causing Brownian motion can also be taken into account. Applying Newton's second law of motion, the equation of motion for each particle can be expressed as

$$m \frac{du_i}{dt} = \sum F_i \quad (3.3)$$

where i corresponds to the two principal directions, namely x and y , and m is the mass of each suspended particle. The right hand side of the above equation represents the summation of all the forces acting on each particle, inside the

channel. This term encompasses the fluid drag and the dielectrophoretic force on the particle. It may also include other forces, such as, random force, particle-particle interaction forces and buoyancy forces, provided the force expressions are known. Assuming that the particles do not accelerate and balancing the active forces on the particle, the following trajectory equations for each droplet can be derived [Masliyah, 1994, Elimelech *et al.*, 1995]

$$\frac{dx}{dt} = f_3 v_x + \frac{F_{DEP,x} + \sum F_x}{6\pi\mu a} \quad (3.4a)$$

$$\frac{dy}{dt} = f_1 f_2 v_y + \frac{F_{DEP,y} + \sum F_y}{6\pi\mu a} \quad (3.4b)$$

Here, $F_{DEP,x}$ and $F_{DEP,y}$ represent the axial and transverse components of the dielectrophoretic force on the particle at a given location over the electrode plane. $\sum F_x$ and $\sum F_y$ represent all other forces, combined, acting on the particle at the same instance, in x and y directions, respectively. Various components of the trajectory model and the flow of information in the analysis are summarized in Figure 3.7.

The size of particles considered in this work falls in the range of 1-2 μm . In case of sub-micron particles, the DEP force necessary to manipulate particles needs to be significantly large to overcome Brownian motion. For particles in the size range of 1 μm , the dielectrophoretic force, and consequently the particle velocity is considerable and the effect of Brownian motion is negligible. However, for smaller particles, Brownian motion can dominate particle dynamics in the system [Russel and Schowalter, 1995]. Gravity as an external force has influence on a particle in a fluid, which manifests itself as the buoyancy force. Again, for the size of particles considered here, the buoyancy force is usually negligible, but can be seen over long periods of observation [Morgan and Green, 2002]. A good review of forces in microelectrode structures can be found in Ramos *et al.*, 1998, Green *et al.*, 2000b.

It should be noted that Eqs. 3.4a and 3.4b, in contrast to Eq. 3.1, consider the hydrodynamic retardation near the wall depending on the magnitudes of the hydrodynamic correction functions. These two differential equations govern

the position of the particles suspended in a flowing medium. Solving the above two ODE's with proper initial conditions can provide the complete trajectory for each particle inside the channel.

These trajectory equations were solved using a variable order, multistep solver based on the numerical differentiation formulas (NDFs). The NDFs are generally more efficient than the closely related family of backward differentiation formulas (BDFs), also known as Gear's methods. The trajectory analysis is implemented through a commercial package, MATLAB[®], which offers a variety of solvers for different types of differential equations. The ODE's are solved using *ode15s*, a solver available for stiff problems. The relative and absolute tolerance during the solution process were set to 10^{-6} and 10^{-9} , respectively.

3.4 Fluid Velocity Field in Crossflow Filtration

Application of ac electrokinetics requires the presence of a fluid as a suspending medium for the particles. The movement of a particle suspended in the fluid, under the action of an external force, is influenced by the fluid motion as well. An understanding of the fluid flow field is therefore essential to predict the motion of the particles. In this section, the governing fluid dynamic equations will be summarized, so that the fluid flow can be analyzed inside the channel bounded by the membrane on one side. In the following discussion, the fluid is assumed to be the continuous medium.

In the system considered here, the fluid is assumed to be incompressible. The average crossflow velocity inside the system is restricted to a low range of values based on transverse Reynolds number, $Re_x < 2000$. However, the wall suction applied on the bottom wall (membrane) is several orders of magnitude smaller than the crossflow velocity, therefore, $Re_y \ll Re_x$. The Reynolds number limits the fluid flow inside the channel to laminar flow regime.

The flow of the bulk medium inside the channel is modelled as flow between parallel plates. The crossflow, described by the parabolic velocity profile, tra-

verses the electrode plane in x direction (Figure 3.1). Poiseuille fluid flow occurs at some distance from the entry point of the fluid into a channel. At the entry point, the fluid flow can be significantly different and there is a characteristic distance to be travelled by the fluid before the parabolic profile is established (*entry length*). Detailed description of entry length can be found in standard fluid mechanics text [Tritton, 1988]. For low Reynold's numbers, the entry length is short and can be ignored without significantly effecting the analysis. Therefore, the fluid flow in the axial direction can be assumed to be a parabolic profile.

In the following discussion, two possible fluid flow situations have been described, in the context of crossflow membrane filtration. First, the suction velocity employed at the bottom wall of the channel, *i.e.*, the membrane surface, is assumed to be constant over the span of the channel length. Secondly, the fluid flow field is analyzed with an intermittent wall suction applied only on the parts of membrane surface that are not blocked by the presence of electrodes. The effects of these two wall suction conditions are compared to gain understanding of the particle trajectories near the membrane surface.

3.4.1 Crossflow filtration with uniform suction at membrane

For the two-dimensional crossflow filtration process with uniform wall suction, general analytic expressions for the undisturbed fluid flow components in the directions parallel and perpendicular to the channel walls were given by Kleinstreuer and Paller, 1983. Here, the simplified forms of these equations have been used, applicable for transverse Reynolds numbers smaller than unity. The axial or crossflow velocity component V_x is given by

$$v_x(x, \lambda) = \frac{3}{2} \bar{V}_x (1 - \lambda^2) \quad (3.5)$$

The uniform wall suction velocity is defined as

$$v_y(\lambda) = \frac{V_w}{4} (-\lambda^3 + 3\lambda + 2) \quad (3.6)$$

where H is the height of the mid-plane of the channel, y varies between the electrode surface and mid-plane of the channel and \bar{V}_x is the average flow velocity in the channel, defined through the Reynolds number, based on the hydraulic diameter of the channel. Here λ is a dimensionless distance from the permeable wall defined as $(1 - y/H)$, where y is the distance from the membrane surface to the center of a particle. V_w is the uniform suction velocity at the bottom wall of the channel. The wall suction effect diminishes far away from the wall. The wall suction in these simulations is several orders of magnitude smaller than the average crossflow velocity. v_x and v_y are the same velocity components in axial and transverse directions, respectively, as mentioned in Eq. 3.2 and 3.4.

3.4.2 Velocity components for intermittently permeable membrane

It is possible that when electrodes are embedded on the membrane, the wall suction becomes intermittent, and correspondingly, the velocity profiles near the membrane will tend to differ substantially from the profiles given by Eqs. 3.5 and 3.6. To account for this effect, we simulated the influence of the intermittent suction on the near-membrane velocity field by directly solving the governing fluid momentum (Navier-Stokes) equations for the crossflow filtration process. Assuming steady incompressible two-dimensional flow in a Cartesian coordinate system, the governing Navier-Stokes equations can be written as

$$u \frac{\partial u}{\partial x} + v \frac{\partial u}{\partial y} = -\frac{1}{\rho} \frac{\partial p}{\partial x} + \gamma \left(\frac{\partial^2 u}{\partial x^2} + \frac{\partial^2 u}{\partial y^2} \right) \quad (x - \text{momentum}) \quad (3.7a)$$

$$u \frac{\partial v}{\partial x} + v \frac{\partial v}{\partial y} = -\frac{1}{\rho} \frac{\partial p}{\partial y} + \gamma \left(\frac{\partial^2 v}{\partial x^2} + \frac{\partial^2 v}{\partial y^2} \right) \quad (y - \text{momentum}) \quad (3.7b)$$

where $u(x, y)$ and $v(x, y)$ are the axial and transverse components of the fluid velocity, respectively. ρ and γ are the fluid density and the kinematic viscosity, respectively. The properties of the bulk medium, namely, density and viscosity, are assumed to be that of the suspending medium. Combined with the continuity equation $\nabla \cdot \mathbf{u} = 0$, where \mathbf{u} is the fluid velocity vector, the solution

of the above equations with appropriate boundary conditions representing the filtration process, leads to a detailed map of the fluid velocity field.

The flow domain modelled here spans over a section of the rectangular cross-flow filtration channel, with intermittent microelectrodes embedded on the permeable membrane surface. The inlet flow is assumed to be one dimensional and parabolic as given by Eq. 3.5. The membrane surface boundary conditions can be described as

$$u = 0 \quad (3.8a)$$

$$v = V_w, \partial\Omega = G \quad (3.8b)$$

$$v = 0, \partial\Omega = W \quad (3.8c)$$

where $\partial\Omega$ represents the boundary of the computational domain. In other words, the axial velocity on the membrane is always zero based on no-slip condition, while the transverse velocity switches from uniform suction V_w at the gaps to zero transverse velocity on the electrodes. At the exit of the channel, the boundary condition is defined as a normal flow with zero pressure, *i.e.*, the tangential component of the velocity and the normal component of the viscous force is zero. The final boundary condition is applied at the mid-plane of the filtration channel, where symmetry condition is assumed to be valid. This boundary condition implies that both walls of the channel are permeable. Moreover, a no-slip condition is used on the wall facing the membrane. Use of either boundary condition leads to nearly identical velocity fields near the membrane surface as long as the transverse velocity is several orders of magnitude smaller than the axial velocity. Simulations were performed for two channel lengths, namely, 10 mm (containing 100 electrodes) and 1.3 mm (containing 13 electrodes). The electrode width and gap width were chosen to be equal, implying that 50% of the membrane surface is permeable.

Numerical solution procedure

The governing equations were solved by employing a finite element approach. The discretization of the geometry was performed using triangular *Lagrange*

element. Mesh distribution can be controlled by tuning different mesh parameters. Adjusting the maximum element size on the bottom boundary and a mesh growth factor, a non-uniform mesh was generated with highly refined spatial discretization near the membrane. The results for fluid velocity field discussed here were obtained with 26,000 Lagrange elements in the computational domain. The finite element analysis for the fluid flow was implemented using a commercial package, FEMLAB[®] (COMSOL, Inc.). The governing equations were solved using a non-linear solver employing a damped Newton method. The relative tolerance was set to 10^{-6} , while the maximum and minimum damping parameter values were set to 1 and 10^{-4} , respectively.

The accuracy of the solution was verified in two limiting cases. First, the results were compared with the case of a uniform suction over the entire membrane. In this case, the boundary condition was set to $v = V_w$ on $\partial\Omega = W$. The solutions were compared with the velocity profiles given by Eqs. (3.5) and (3.6). The agreement for the stated number of element was excellent. Secondly, the transverse velocity profiles were compared, obtained over a section of the channel between the fourth and fifth electrodes from the entrance, using the two different channel lengths. The results were identical in both cases, indicating that the local velocity profiles were unaltered irrespective of the domain length chosen. The velocity profiles resulting from the finite element simulations were exported as gridded data, and employed in the subsequent trajectory analysis calculations to determine the convective velocity of the particles.

One should note that the simulations for the velocity fields were performed assuming no body force (gravity or electrical forces) on the fluid. While effect of gravity is obviously negligible for the geometry under consideration, one might be concerned about the absence of the electrical body force in these simulations. In general, the application of electrical fields to a fluid produces body forces and therefore fluid flow. There are two main forces related to the action of the electric field on the fluid: (a) Electrothermal, where the electric field acts on the gradients in permittivity and/or conductivity produced by non-uniform

heating, and (b) Electroosmosis, where the electric field acts on free charge in the electrical double layer. The electrical body force is given by [Morgan and Green, 2002]

$$\mathbf{f}_e = \rho \mathbf{E} - \frac{1}{2} |\mathbf{E}|^2 \nabla \varepsilon_m + \frac{1}{2} \nabla \left(\rho_m \left(\frac{\partial \varepsilon_m}{\partial \rho_m} \right)_T |\mathbf{E}|^2 \right) \quad (3.9)$$

where ρ and ρ_m are the charge and mass densities respectively and ε_m is the permittivity of the fluid. On the right hand side of this expression, the first term is the Coulomb force, the second is the dielectric force and the last term is the electrostriction pressure. For an incompressible fluid, the electrostriction pressure can be ignored since it is the gradient of a scalar and has no effect on the dynamics of the system. The above expression defines the body force in terms of local variations in charge density. Localized Joule heating of fluid gives rise to gradients in permittivity and conductivity, which in turn produce a body force on the fluid. The conductivity gradient produces free volume charge and Coulomb force, while a permittivity gradient produces the dielectric force [Ramos *et al.*, 1998, Green *et al.*, 2000a, Gonzalez *et al.*, 2000, Green *et al.*, 2002a]. The Joule heating of the fluid when subjected to an electric field is discussed by Castellanos, 1998. As found by Ramos *et al.*, 1998, the body force is frequency dependent and has two distinct limits: at low frequencies the Coulomb force dominates, and at high frequencies, the dielectric force dominates the fluid motion. There can also be natural convection due to temperature gradient in the system which produces changes in density. The electrothermal force can be calculated from the solution of electric and thermal fields, to give the body force in the Navier-Stokes equation, from which the velocity of the fluid can be calculated.

If mobile free charges (such as ions) are present in the solvent, the solvent velocity will be subjected to an electrical body force $\rho_f \mathbf{E}$, where ρ_f is the volumetric charge density and \mathbf{E} is the electric field intensity. In absence of free charge, this term should be zero. Secondly, the solvent can become polarized in an alternating electric field, much in the same way as the particles are subjected to dielectric polarization. Here, this effect has been neglected, considering that

the dielectric polarization effect on the solvent molecules will be negligible compared to the colloidal particles, since the solvent molecules are barely a few angstroms in size, as opposed to the micron sized colloidal particles. Nevertheless, detailed computation of the velocity fields considering these electrodynamic forces on the solvent might provide considerable insight regarding fluid flow in an alternating electric field. This type of analysis was not considered in the present work, and the flow field simulations presented here should be regarded as simplistic velocity fields accounting solely for the flow of a solvent over an intermittently permeable membrane.

3.4.3 Fluid velocity profiles

Figure 3.2 shows the surface plot of the vertical component of the fluid velocity over a small section of the total channel length (5% of channel length). Both axes are scaled with respect to electrode width (W) in the channel. The horizontal axis in this plot shows part of the channel over a span of 5 electrodes and in the gaps in between the electrodes. The vertical component of the velocity is observed to fluctuate periodically in axial direction near the membrane wall. This can be attributed to the periodic presence of the electrodes on the respective surface, *i.e.*, the blockage of the membrane surface by the electrodes at regular interval. Dark regions in the plot represent the section of the permeable surface where wall suction is applied. Away from the permeable wall the vertical velocity component decays rapidly and vanishes at the height of the mid-plane of the channel.

Figure 3.3 depicts the decay behavior of the transverse component of velocity at increasing height above the membrane surface. Each line in the plot shows the velocity profile at a given height over the bottom channel wall. Diminishing amplitudes of the oscillating velocity profiles indicate almost exponential decrease of the transverse velocity component as the distance from the bottom wall increases. It should be noted that at a height equal to two electrode widths ($\approx 100 \mu\text{m}$), the velocity becomes almost uniform, showing negligible variation

in axial direction. This distance is also the effective range of DEP force field and the polarizable entities in the system will experience the greatest effect of both the electric field and fluid suction within this narrow range.

3.5 Trajectory in Dielectrophoretic Membrane Filtration

At this point, we have developed a model to study the effect of deterministic forces on particles suspended in a flowing fluid, contained in a channel. Prior to that, movement of polarizable particles in a non-uniform electric field, engendered by interdigitated parallel bar electrodes have been discussed. The necessary expressions to evaluate the electric field and consequently the dielectrophoretic force field above an electrode array have been described in chapter 2. In the work presented here, we intend to utilize the dielectrophoretic forces to manipulate polarizable colloidal particles in a flowing suspension. With that goal in mind, a membrane filtration channel with interdigitated electrode array embedded in the membrane surface, is proposed to produce a DEP force field, to facilitate the separation process. With the trajectory model developed in this chapter it is now possible to use DEP force as a deterministic force in the trajectory equations and combine with the fluid flow field solution to study the particle trajectory inside the system described previously.

In the previous chapter, the frequency dependent nature of the dielectrophoretic force has been emphasized. Based on the example of latex-in-water system, the change of behavior of the DEP force, from positive to negative upon crossing the crossover frequency, has been explained. This remarkable characteristic of dielectrophoresis can be exploited to attract or repel a target particle suspended in a fluid. Let us again consider the same latex-in-water system described in chapter 2, to visualize how the particle would behave inside the channel used in the model. If a suspension of latex particles in water is flowing through the channel, following the restrictions mentioned in the previ-

ous section and is subjected to an ac electric field, the particles can either be attracted toward the membrane surface or repelled away from that surface. The nature of the particle movement will be dictated primarily by the nature of the DEP force engendered by the electrode array, assuming that DEP force is the dominating force in the system.

Following the analysis in chapter 2, it is now known that the DEP force depends on the relative polarizations of the particle and the surrounding medium, frequency of the applied ac voltage and also the magnitude of the voltage. Figure 2.5 shows the change of sign of the real part of the Clausius-Mossotti factor with the increase in applied frequency. Therefore, the latex particles in the flowing suspension can be subjected to an attractive or repulsive force field if the frequency of the applied signal is on either side of the crossover frequency. The other aspect of this membrane filtration system is the wall suction. The influence of uniform wall suction and intermittent suction at the membrane will be discussed in the context of both positive and negative DEP forces.

3.5.1 Particle trajectories under uniform suction

First, the particle trajectory is discussed in a system with uniform wall suction at the permeable wall. Figure 3.4 shows trajectories of a single particle released from the same location under different conditions, namely, attractive DEP force, repulsive DEP force and plain convection, presented by different symbols on the plot. The axes are nondimensionalized with respect to electrode width (W). According to the discussion in chapter 2, latex particles in water may experience either positive DEP or negative DEP depending on the frequency of the applied ac signal. The trajectories are representative of these situations. At sufficiently low frequency the DEP force field engendered is attractive in nature, thus attracting the latex particles toward the electrode plane. Conversely, the particles are repelled away from the same surface if the frequency is above the crossover frequency. In the latter case the particle gradually moves upward until it reaches a steady height thus successfully prevents the particle from

depositing on the membrane surface. Figure 3.4 also shows the trajectory of the same particle without the presence of any DEP force. In this case, the particle drifts down under the action of hydrodynamic forces and settles on the membrane surface after traversing in axial direction. This in effect shows how a repulsive DEP force field can be utilized to avoid fouling in a membrane based separation.

3.5.2 Particle trajectories under intermittent suction

Following the fluid flow analysis described in previous section, we have studied the particle trajectory in a channel with intermittent wall suction. The vertical component of the fluid velocity field obtained from finite element analysis is used instead of the uniform wall suction. The finite element analysis was based on the same wall suction velocity except that the membrane surface was partially blocked by impermeable electrodes. Figure 3.5 shows the latex particle trajectory under identical conditions as in Figure 3.4. Same nondimensionalization as in Figure 3.4 is followed. It is interesting to note that in case of positive DEP force, the effect of different wall suction on the particle trajectory is imperceptible due to the strong influence of DEP force. Figure 3.6 shows more descriptive trajectories of the latex particle, attracted towards the membrane under uniform and intermittent wall suction. The variation in the two trajectories is marginal, demonstrating that when the particles are subjected to positive DEP, the particle trajectories will not be drastically altered by various wall suction. The effect of uniform and non-uniform wall suction is more apparent in the other two cases, shown in Figure 3.5, namely, in the absence of any DEP force and under negative DEP force. When the particle is not under the action of DEP force of any kind, the particles will obviously deposit on the membrane. However, it can be seen from Figure 3.5 the particle now travels a longer distance in axial direction before depositing on the surface compared to the distance traversed under uniform suction. Similarly, when the particle is acted upon by a repulsive DEP force inside a channel with intermittent wall

suction, the particle is pushed away to an even greater height than in case of uniform suction. Intuitively, the particle experiences less convective drag force in the transverse direction, when the velocity field in the vertical direction is intermittent near the membrane, thus travelling to higher height even when the negative DEP force remains unaltered. Therefore, it would be fair to say that the predictions based on an uniform wall suction, are on the conservative side; yielding the lower bounds of the influence of DEP on the particle trajectories.

3.6 Summary

A trajectory model has been developed to study membrane based separation system aided by dielectrophoresis. The model takes into account the effect of external forces acting on the system. The fluid flow field inside a channel has been discussed in the context of membrane filtration with intermittent suction applied on the membrane. Finally, the trajectory equations are formulated to track single particles in a flowing suspension, acted upon by dielectrophoretic forces. The trajectory model developed in this chapter will be put to use in the following two chapters to analyze the scope of the application of dielectrophoresis in two different contexts - to use positive DEP to improve membrane separation by preferentially attracting a target species towards the membrane and to apply negative DEP to prevent colloidal entities from depositing on the membrane surface.

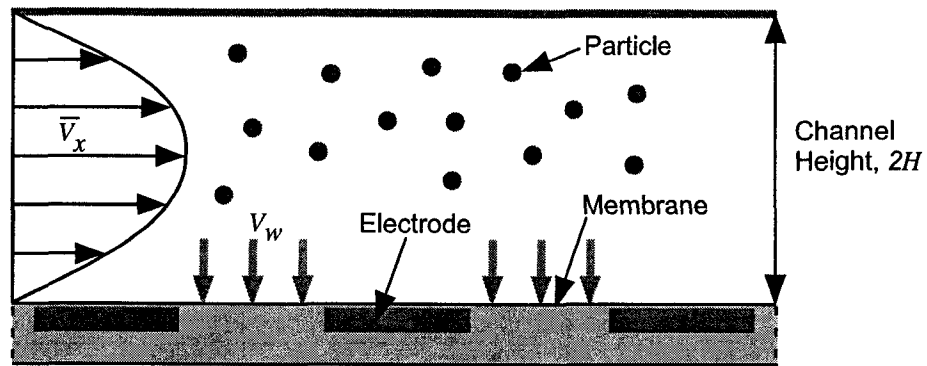


Figure 3.1: Schematic diagram showing the conceptual picture of the proposed system for dielectrophoretic membrane filtration. $2H$ represents the total height of the channel. \bar{V}_x and V_w are average crossflow velocity in the channel and suction velocity on the membrane, respectively.

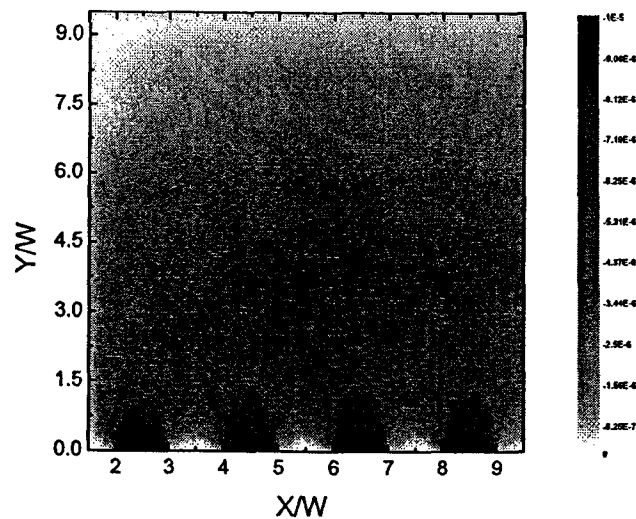


Figure 3.2: Surface plot of velocity component in vertical direction near the permeable surface of the channel with wall suction applied intermittently on the bottom wall. The plot shows the finite element solution obtained over a small representative section of the channel. Both the axes are nondimensionalized with respect to electrode width (W). The baseline of the geometry consists of 5 electrodes and 4 gaps in between. Width of electrodes and gaps are both $50 \mu\text{m}$. The wall suction applied in the gap region is 10^{-5} m/s and average crossflow velocity is 10^{-3} m/s at the entrance of the channel.

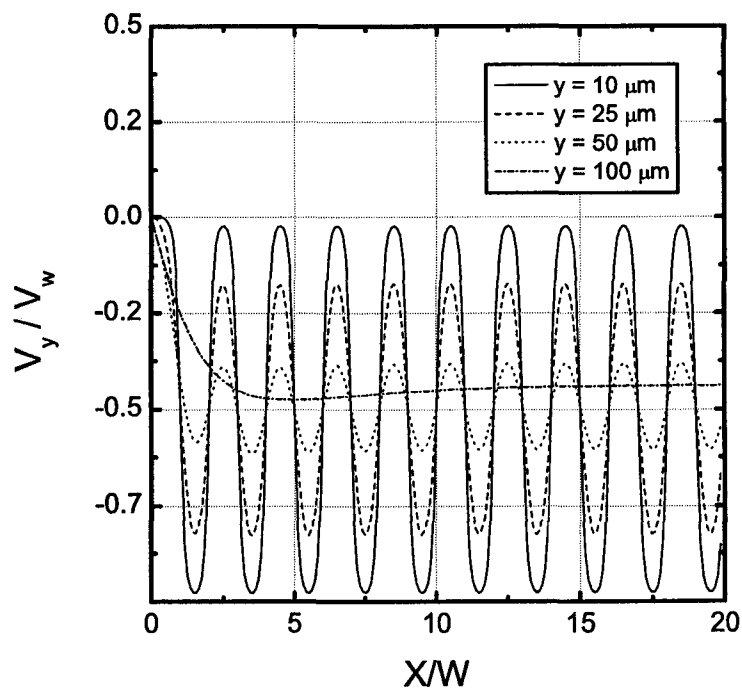


Figure 3.3: Distribution of fluid velocity component in vertical direction at different horizontal planes, near the permeable surface of the channel with wall suction applied intermittently in the gap region. All the conditions remain same as in Figure 3.2. Horizontal axis is nondimensionalized with respect to electrode width (W), in the vertical axis the actual velocity is scaled with respect to maximum wall suction, $V_w = 10^{-5}$ m/s.

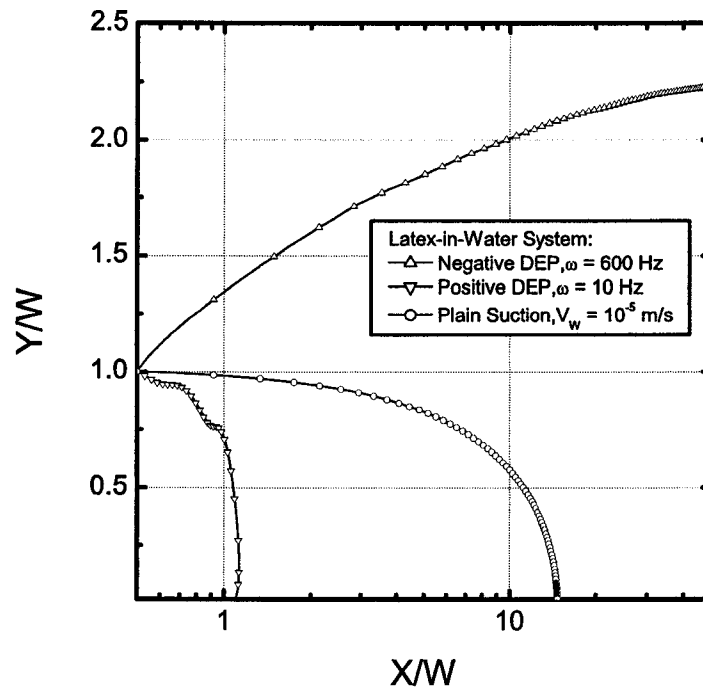


Figure 3.4: Trajectory of a particle in latex-in-water system under different conditions, namely, positive DEP, negative DEP and in the absence of DEP force. Both axes are nondimensionalized with respect to electrode width (W). The wall suction is uniform in all three cases, $V_w = 10^{-5}$ m/s and average crossflow velocity is 10^{-3} m/s. All other parameters are same as in table A1.

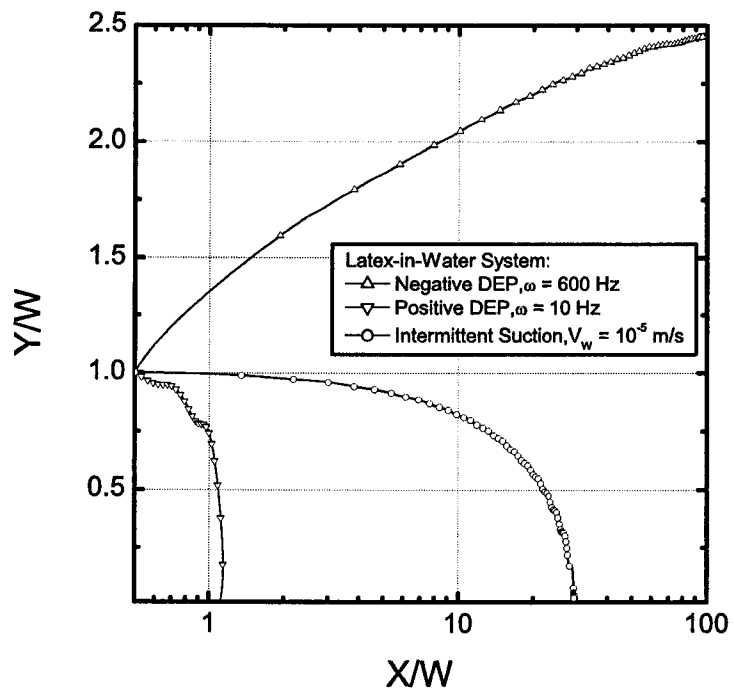


Figure 3.5: Trajectory of a particle in latex-in-water system under different conditions, namely, positive DEP, negative DEP and in the absence of DEP force. Both axes are nondimensionalized with respect to electrode width (W). The wall suction is intermittent in all three cases, $V_w = 10^{-5}$ m/s and average crossflow velocity is 10^{-3} m/s. All other parameters are same as in table A1.

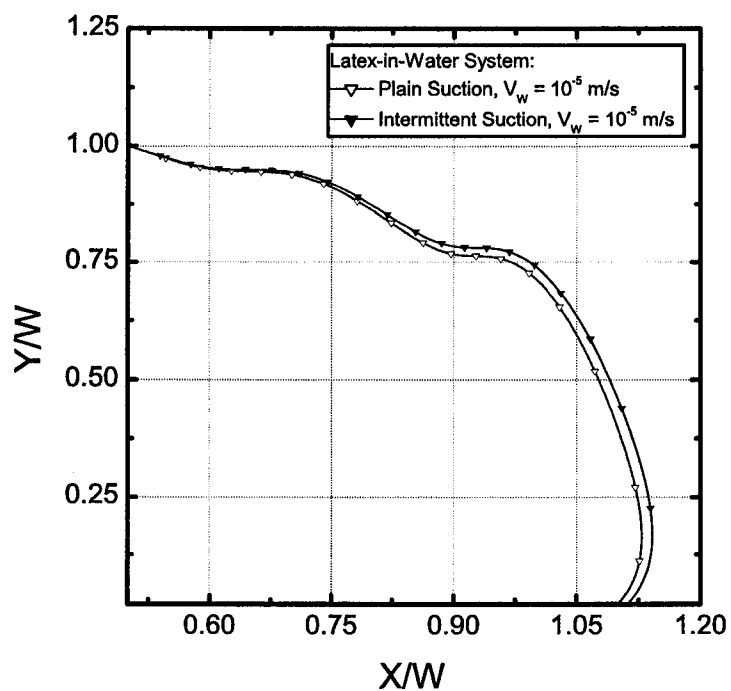


Figure 3.6: Trajectory of a particle in latex-in-water system under positive DEP, with uniform and intermittent wall suction. Both axes are nondimensionalized with respect to electrode width (W). The average crossflow velocity and maximum wall suction values are same as in previous figures. All other parameters are same as in table A1.

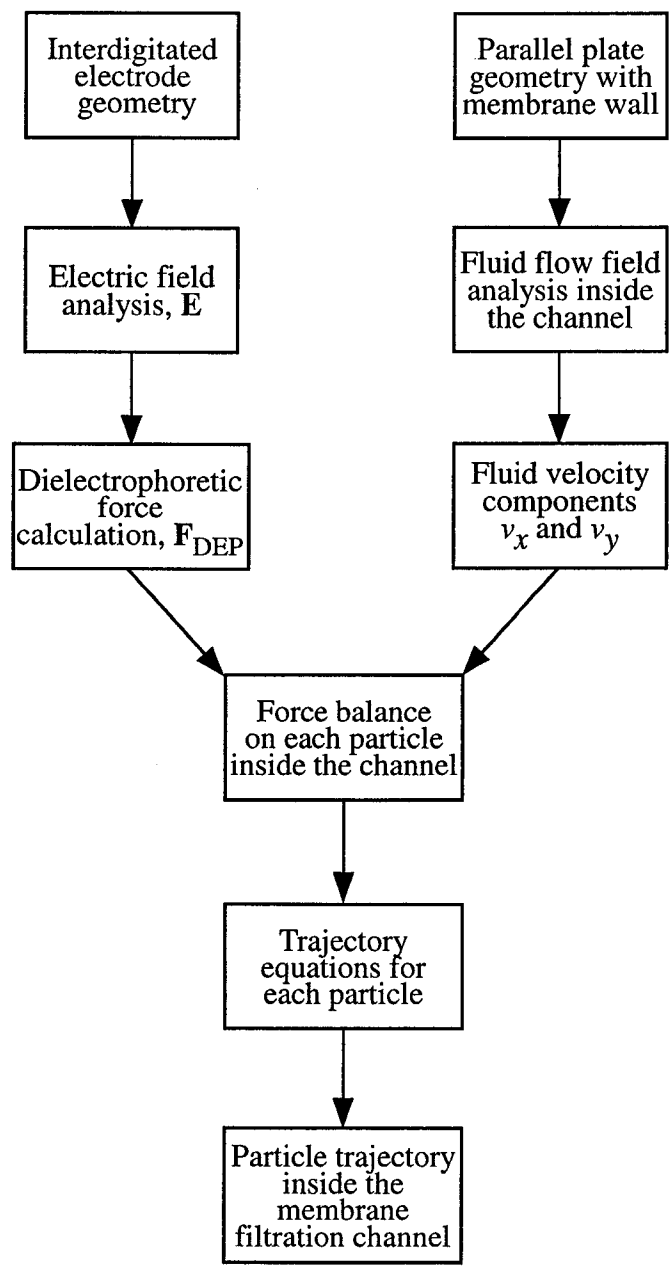


Figure 3.7: Block diagram showing the steps involved in formulating the trajectory model.

Chapter 4

Dielectrophoretic Filtration in Water-in-Oil System

The general mathematical framework developed and explained in the previous chapter will be used in this chapter and the following chapter to model two different systems, based on the attractive and repulsive manifestation of DEP forces in colloidal systems, subjected to crossflow membrane filtration. In this chapter, the application of positive (attractive) DEP forces to preferentially attract colloidal scale droplets toward the membrane in a crossflow filtration system will be described. The technique is applied to a water-in-oil emulsion, causing the water droplets to migrate to the membrane, thereby creating a water rich phase at the membrane surface. This will be followed by evaluation of the effectiveness of the proposed DEP based separation system with respect to conventional membrane separation techniques.

The Water-in-Oil system is basically a dilute emulsion subjected to dielectrophoretic force in a crossflow filtration channel. This system attempts to mimic the typical emulsion composition during extraction of bitumen from tar sands using water based processes. During such a process, about one percent (by volume fraction) water remains suspended in the extracted dilute bitumen as microscopic droplets [Xu *et al.*, 1999, Wallace *et al.*, 2001]. These droplets are difficult to remove by centrifugal separation, and pose serious problems in the downstream processes, which include corrosion of the equipment, unwanted

chemical reactions leading to products that can be corrosive, and numerous other difficulties [Eaton, 2000]. In this context, a technology for removal of this residual water from diluted bitumen has become a major focus of attention during the recent years.

4.1 System Description

A dilute water-in-oil emulsion has been considered here as the suspension flowing through the crossflow membrane filtration channel, described in the chapter 3. The same channel geometry as in Figure 3.1, is assumed for the simulations in this chapter. In this two component system, the microscopic water droplets are assumed to be ideal spheres and sparsely distributed in the oil phase. The low concentration of water in the suspending media allows us to assume no interaction amongst the droplets, thus considerably simplifying the problem. The oil phase is modelled with same properties as Decane. The specific gravity of Decane is very close to unity, which implies that the water droplets in the system will be neutrally buoyant.

In terms of electrical properties, water droplets have higher conductivity and higher dielectric permittivity than the suspending medium. As explained in chapter 2, these electrical properties along with the frequency of the imposed ac field, determine the nature of dielectrophoretic response of the system. The water-in-oil system can be subjected to an attractive force field, provided an appropriate frequency is chosen for the applied ac voltage. A given system may experience both positive and negative DEP force in different regions of the frequency spectrum depending on the complex permittivity. Figure 4.1 shows the variation of the real part of Clausius-Mossotti factor for water-in-oil and oil-in-water systems with the frequency of applied voltage, as in Figure 2.5 for latex-in-water system. In both systems, the value of the Clausius-Mossotti factor does not switch sign as the frequency is increased. However, it can be seen from Figure 4.1 that for the water-in-oil system, the real part of the Clausius-

Mossotti factor remains positive over a wide range of frequencies. On the other hand, the same parameter attains negative value in a oil-in-water system, for the same range of frequencies. The water-in-oil emulsion in this analysis has been studied for a specific range of the frequencies (600 Hz - 2 kHz), where the suspended water droplets experience only positive DEP force, i.e, the real part of Clausius-Mossotti factor for the system remains positive. The typical property values of the two components, namely, water and decane are listed in table A2.

The feed solution enters the channel with an initial concentration of water droplets suspended in Decane, at the inlet. The cross flow velocity of the emulsion is dictated by the volume flow rate. In these simulations, the flow rate is restricted by low value of Reynolds number and consequently, the flow through the channel is approximated as laminar flow. Therefore, the fluid flow problem is simplified according to the formulation described in chapter 3. The fluid velocity profile at the inlet of the channel is assumed to be parabolic and defined as a function of Reynolds number.

As the emulsion flows over the microelectrode array, the water droplets dispersed in the continuous phase are pulled by the electrical forces and begins to move towards the bottom wall of the channel which contains the embedded electrodes. The DEP force is usually strong enough to deflect droplet trajectory even in the presence of convective force. Within very short span of time (less than 1 second), droplets close to the electrode plane, collect near the electrode edges, *i.e.*, regions of highest field gradient and gradually the concentration of water increases at the bottom wall. The permeable membrane then allows these droplets to be removed from the feed stream to the permeate side. The removal of water can be further enhanced by adding small wall suction on the membrane. A concentration gradient develops inside the channel while the water phase is removed from the bulk solution and this is expected to set up diffusion of droplets towards the bottom wall of the channel. As a result, the flowing emulsion will have significantly lower concentration of water at the outlet.

Such a process can be extremely useful in a variety of applications involving separation of the components of a microemulsion. Apart from this example, there are several other microfluidic separation scenarios in which this type of separation technique could theoretically be applied.

4.2 Simulation Results

In this section, migration of the microscopic water droplets under attractive DEP force is examined, to conduct a parametric study of the separation process in DEP enhanced membrane filtration. The effect of various control parameters, such as droplet size and electrode length are discussed, with regards to trajectory analysis. First, the droplets trajectories are obtained by considering the influence of attractive DEP force only. This resembles the situation where the water-in-oil emulsion flows through an impermeable wall channel, thus no wall suction is applied on the membrane surface. Simulation results for an impermeable wall channel reflects the true potential of the positive DEP forces as an effective means to separate water droplets from the emulsion. Secondly, to facilitate the preferential separation of water droplets from the water-in-oil emulsion, a wall suction component is added on the membrane surface. Based on the analysis in chapter 3, it is anticipated that the inclusion of effective wall suction on the membrane would further enhance the separation effectiveness of the membrane filtration process.

4.2.1 Droplet migration in an impermeable wall channel

In this section, the scope of using positive DEP effect to attract and capture micron-sized droplets suspended in a flowing suspension inside a channel with impermeable walls is explored. As outlined in the chapter 3, the droplet velocity can be calculated by balancing the x and y components of the DEP force and hydrodynamic drag acting on each droplet. The time required for a droplet to reach the electrode plane can be calculated by following the path of each

droplet from the time of its release. For this analysis, a dilute suspension of micron-sized water droplets in Decane has been considered, flowing across the electrode plane. The trajectory of a number of droplets inside the channel is studied over an array of electrodes (40 electrodes in this case), where both the electrode width and spacing are $50\ \mu\text{m}$ and the height of the channel is $100\ \mu\text{m}$. The applied voltage is $50\ \text{V}$ at a frequency of $600\ \text{Hz}$. The width of the channel is considered to be infinite compared to the electrode dimensions.

Figure 4.2 depicts a few sample trajectories of the droplets starting from different initial positions in the channel, until they stick to the electrode plane. Figure 4.2a and 4.2b show the trajectories for two different voltages, namely, $50\ \text{V}$ and $100\ \text{V}$, respectively. All other conditions are identical in the two figures.

It is evident from these figures that DEP forces have greater influence on droplets that are closer to the electrode array and the time required for the droplets to reach the electrode surface (sticking time) can be reduced significantly by increasing the applied voltage. By increasing the voltage by a factor of two, the maximum sticking time (corresponding to the droplets released from the maximum vertical distance) was reduced by 73%. It should also be noted that up to the midsection of channel height, influence of the cross flow velocity is more pronounced on the droplets with increasing vertical distance. In other words, droplets further away from the electrode plane will travel over a longer axial distance before sticking to the membrane (evident from the sticking times depicted in the legend). The slightly undulating nature of the trajectories is due to the frequency dependent oscillation of the DEP force.

The DEP force acting on a droplet is proportional to the cube of the droplet radius, and hence, larger droplets demonstrate greater response to the DEP effect. Figure 4.3a shows different trajectories followed by droplets of varying size ($100\ \text{nm}$ - $1500\ \text{nm}$) and Figure 4.3b shows the sticking time required for the same set of droplets. Initial release positions are identical for every droplet. The flat parts of the trajectory lines in Figure 4.3b reflect the situation where the droplet has crossed over the electrode array and is beyond the range of any DEP

effect (in these figures, the electrodes span the first 4 mm of the axial distance). Under similar conditions, as the size of the droplets decreases, attracting the droplets downwards becomes more difficult, and for very small droplets (100 nm in this case) the DEP force fails to alter the horizontal trajectory of the droplet perceptibly. To generate the same amount of force for the smaller droplets, the modification of the geometric parameters and electrode design is needed.

Figure 4.4 shows the variation of magnitude of the DEP force with particle size, at a given separation from the electrode plane. The force increases non-linearly with increasing particle size over four orders of magnitude. It should be noted here, that our simulations for the sub-micrometer sized droplets do not account for the Brownian forces. This may render the smaller droplet trajectories somewhat erroneous. Although the influence of Brownian forces can be embedded in the trajectory analysis through either an effective diffusive drift term or more rigorously using Brownian dynamics, it was perceived as an unnecessary complication when the DEP forces are considerably larger than the Brownian forces. Near the electrode edges, where the field intensity gradients are highest, the DEP forces are at least two orders of magnitude larger than the typical Brownian forces for the smallest droplets.

The electrode width and spacing on the array have an important effect on the process of exerting positive DEP force on the droplets. Results of a simulation for varying electrode width/gap ratio are presented in Figure 4.5. Under identical conditions, increasing the width/gap ratio weakens the gradient of the electric field intensity, which eventually reduces the DEP force exerted on the droplet. This affects the trajectories of the droplets. For larger gaps between the electrodes, the DEP forces are weaker, and the particles traverse a larger axial distance before sticking to the wall. Reducing the gap between the electrodes intensifies the DEP force, and the trajectories sharply approach the wall. All the results were obtained for a fixed pitch of 100 μm . For larger values of the pitch, the DEP forces become less pronounced. Thus, it is emphasized here that DEP is indeed a microscale phenomenon, and even if one contemplates its

application for a large membrane module, it is necessary to ensure that both the electrode width and gap are in the micrometer range.

4.2.2 Droplet migration during dielectrophoretic membrane filtration

To effectively remove the deposited target species from the plane of electrodes, suction must be applied on the permeate side of the membrane, which can provide the necessary pressure gradient for the transport of the droplets across the membrane. If water droplets are allowed to accumulate on the electrode plane, the electric field produced by the electrode array will be altered due to high dielectric constant of water droplets. Here, the formulation from the previous subsection will be extended by incorporating an axially uniform wall suction at the bottom wall of the channel, *i.e.*, the permeable membrane surface. The modelling approach based on uniform wall suction and intermittent suction have already been discussed. The results in chapter 3, demonstrate the relative influence of the two different flow fields inside the channel. In case of positive DEP membrane filtration, it has been found that the particle trajectories are marginally effected by the use of intermittent wall suction as opposed to uniform wall suction. However, uniform wall suction on the membrane will create constant fluid drag on the droplets, causing them to deposit on the membrane at a shorter axial distance than in case of intermittent wall suction. Therefore, for the simulations in this chapter, a uniform wall suction at the membrane has been considered and the resulting droplet trajectories represent the lower bound of the probable droplet deposition distances on the membrane surface. The effect of uniform wall suction is clearly visible in the two trajectories in Figure 4.6. The particle travels shorter distance in axial direction before depositing on the membrane surface when the uniform wall suction is imposed on the membrane.

This model enables us to investigate the effectiveness of application of a coupled dielectrophoretic membrane filtration process. The assumptions used

in the previous section are also valid for this analysis. Density of the emulsion is considered to be very close to that of suspended water droplets, therefore the gravitational effect can be neglected in this case. The suspension is also assumed to be sufficiently dilute so that colloidal and dielectrophoretic interaction between the suspended droplets can be ignored.

4.3 Theoretical Effectiveness

The separation effectiveness of the dielectrophoretic membrane filtration process is calculated by comparing the trajectories of the droplets in the two-dimensional flow field (with the membrane suction), in the absence and presence of the dielectrophoretic field. Trajectories of the droplets released from the same initial position are followed until they stick to the membrane, and the axial distances at which the droplets stick to the membrane are recorded. The efficiency of droplet deposition in presence of the DEP field can then be quantified by determining the ratio of the axial distance traversed by the droplet in absence and presence of the dielectrophoretic field, respectively. Here, the effectiveness of DEP is simply defined as the ratio:

$$\eta = \frac{X_{without\ DEP}}{X_{with\ DEP}} \quad (4.1)$$

where X represents the axial distance traversed by the droplet from the point of release to the point where it sticks to the membrane. It is evident that the effectiveness will be greater than unity if the DEP force enhances the migration of the droplets toward the membrane surface. Figure 4.7 depicts the variation of the DEP effectiveness with the release distance (vertical distance) from the membrane. The simulations were performed by releasing the droplets from a fixed axial location and from incrementally larger vertical distances from the membrane.

A 10 mm long crossflow channel was considered. The axial velocity of the fluid in the channel was 10^{-3} m/s, while a constant wall suction velocity ranging

from $10^{-6} \sim 5 \times 10^{-5}$ m/s was considered. The electrode width and pitch were $50 \mu\text{m}$ and $100 \mu\text{m}$, respectively.

It is evident from Figure 4.7 that the deposition effectiveness increases dramatically in presence of the DEP force. The effectiveness increases as the release distance from the membrane surface is increased. A maximum value of the effectiveness is observed for the vertical release distances between 35 to $45 \mu\text{m}$. This maximum is attained at a greater release distance when the applied voltage is increased. Following the maximum, the effectiveness decreases in a stepwise manner as the release distance is further increased. The nature of the effectiveness curves closely emulates the qualitative trends of the axial DEP force profiles, as manifested in the axial electric field intensity gradients in Figure 2.9a.

To analyze the behavior of the effectiveness curve near each step jump, the trajectories of some of the droplets released from the vicinity of $35 \mu\text{m}$ from the membrane are depicted in Figure 4.8. It should be noted that the trajectories of the droplets become curved backward as they approach the membrane when the release height approaches $35 \mu\text{m}$. For a release distance slightly greater than $35 \mu\text{m}$, the trajectories do not show the backward curve. This phenomenon gives rise to the step jumps in the effectiveness. Noting that the electrode edge in Figure 4.8 is located at $100 \mu\text{m}$ on the horizontal axis, the region in the vicinity of $100 \mu\text{m}$ experiences an intense DEP attractive force. The droplets are transported backward against the axial flow under the influence of this force. However, as soon as the droplet trajectories are out of the range of this attraction, the droplets migrate toward the next electrode under axial convective forces. Thus, for a given electrode arrangement, and a given applied voltage, the trajectories of two droplets released from marginally different heights can be dramatically different, which will give rise to the stepwise diminution of the deposition effectiveness depicted in Figure 4.7.

The results of the trajectory analysis clearly indicate the drastic improvement in the droplet capture from the flowing emulsion in presence of a DEP

force. It should be noted that these simulations depict the effectiveness of the DEP force in attracting the droplets toward the membrane over the convective forces engendered by the transverse wall suction. Furthermore, it is observed that the range of distance from the membrane surface over which the DEP force effectively attracts the droplets, is comparable to the concentration boundary layer thickness due to concentration polarization attainable in typical membrane separation processes. In other words, droplets from distances of 80 - 100 μm can be preferentially attracted to the membrane by application of the DEP forces. If the membrane is permeable to the droplets, then it may be assumed that all these droplets will be transported to the permeate stream. In any event, the DEP force coupled with the membrane permeation will allow concentration of droplets from the bulk feed solution to the membrane and preferential transport of the droplet rich phase across the membrane.

4.4 Summary

A novel technique based on simultaneous ac dielectrophoresis on a parallel electrode array and crossflow membrane filtration is proposed for separation of emulsions. It is demonstrated that the coupled separation process can be highly efficient for removal of water droplets from water-in-oil emulsions.

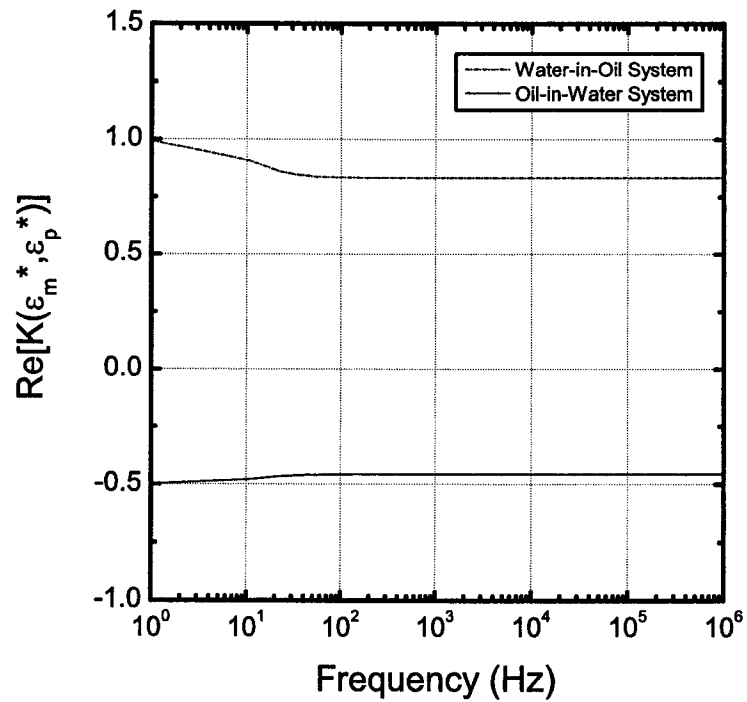
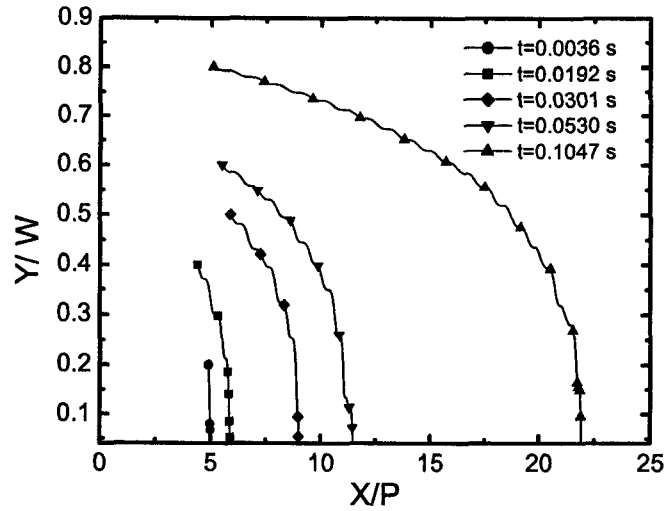
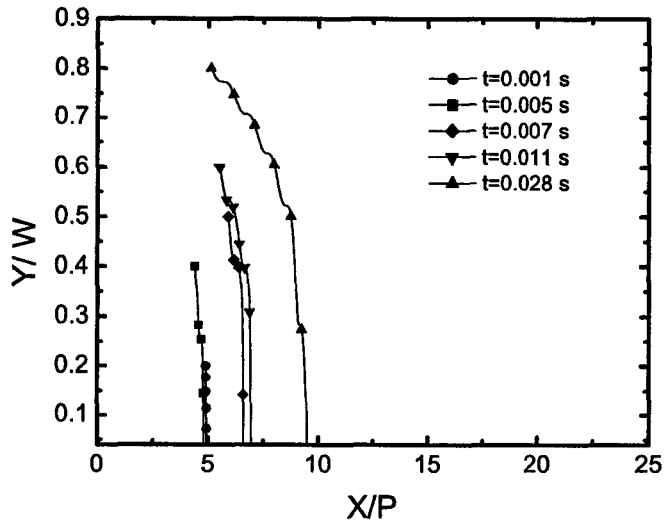


Figure 4.1: Plot of real part of frequency dependent Clausius-Mossotti factor for water-in-oil and oil-in-water systems, against frequency of the applied ac signal. ϵ_p^* and ϵ_m^* represent the complex permittivity of particles and surrounding medium, respectively. The electrical properties of the particle and medium are listed in table A2 in the appendix.

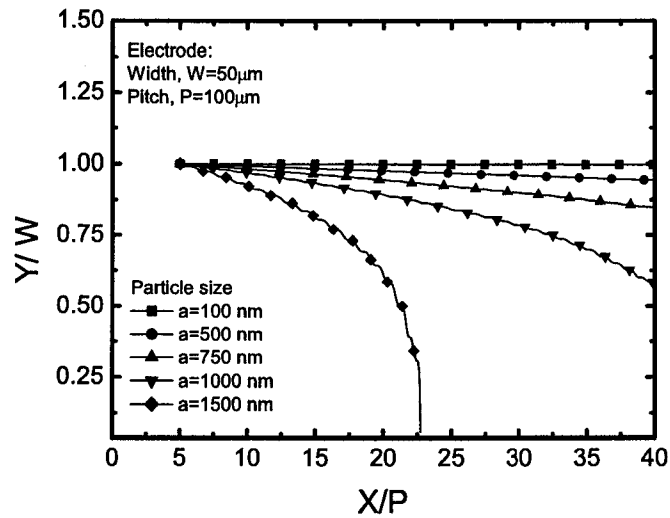


(a)

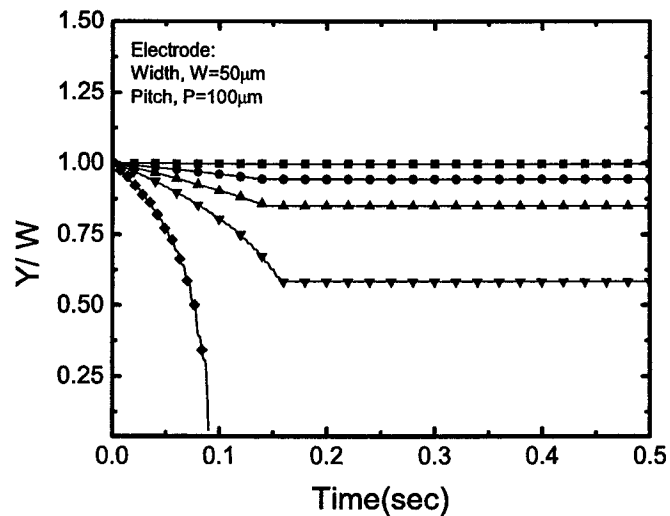


(b)

Figure 4.2: (a) Effect of applied voltage on droplet trajectory (at different height) inside the channel. The horizontal axis in this plot is nondimensionalized with respect to electrode pitch, which is $100 \mu\text{m}$ and the vertical axis is nondimensionalized with respect to electrode width, which is $50 \mu\text{m}$ in this case. Applied voltage is 50 V , frequency $\omega = 600 \text{ Hz}$. Sticking time for droplets released from different locations is shown on the plot. (b) Applied voltage, V is 100 V , frequency, $\omega = 600 \text{ Hz}$. All other parameters remain same as in the previous plot.



(a)



(b)

Figure 4.3: (a) Effect of droplet size on droplet trajectory inside the channel. Droplet size varies from 100 nm to 1500 nm. Applied voltage, V is 50 V, frequency in this case is 600 Hz. Trajectory for droplets of different sizes released from same location. The horizontal axis and the vertical axes are non-dimensionalized as in previous figure (b) Plot of sticking time for droplets of different sizes released from the same location. All parameters are same as in previous plot. The flat part of the droplet trajectory indicates that the droplet has traversed across the electrode array plane and is not effected of DEP forces anymore.

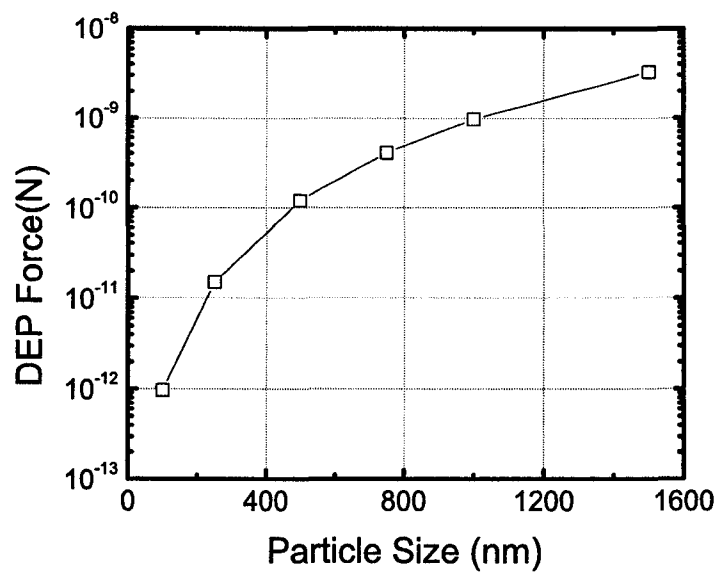


Figure 4.4: Dependence of DEP force on droplet size. Droplet size varies from 100 nm to 1500 nm. Applied voltage, V is 50 V, frequency in this case is 600 Hz.

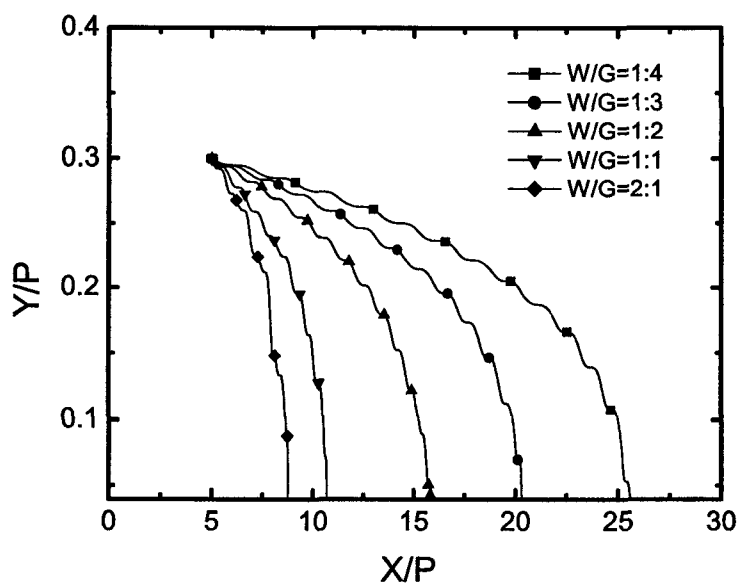


Figure 4.5: Effect of electrode width and spacing on droplet trajectory. Applied voltage, V is 50 V and frequency is 600 Hz. The horizontal and vertical axes are non-dimensionalized with respect to electrode pitch, which is 100 μm .

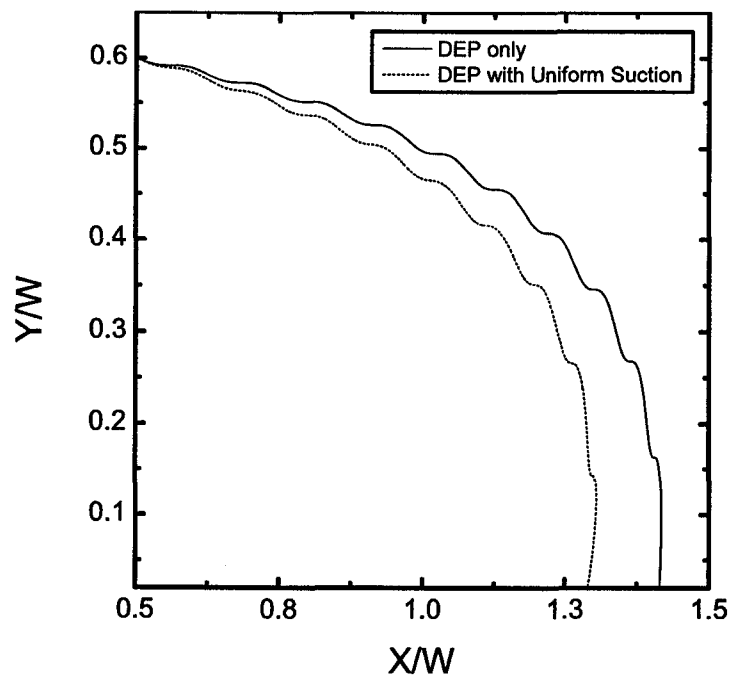


Figure 4.6: Effect of membrane suction on droplet trajectory. Applied voltage is 50 V and frequency is 600 Hz. The horizontal and vertical axes are non-dimensionalized with respect to electrode width, which is 50 μm . The uniform wall suction is 5×10^{-5} m/s.

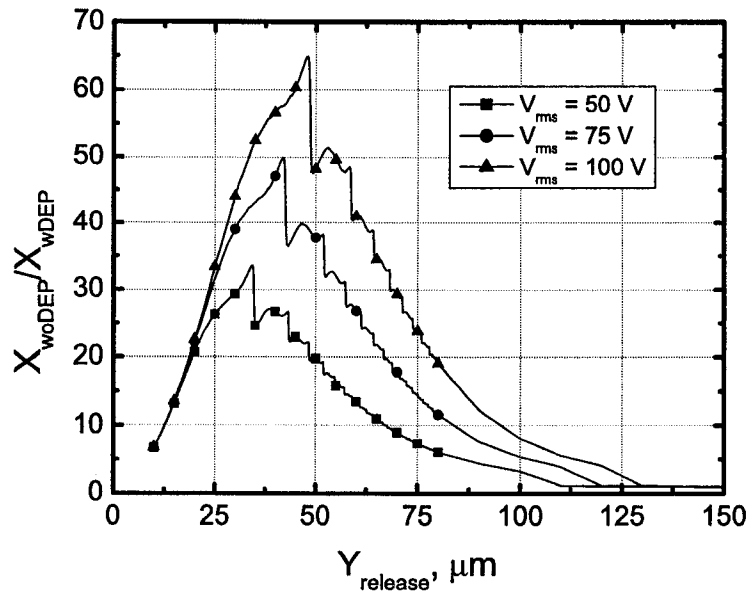


Figure 4.7: Separation effectiveness of the DEP based membrane filtration system. The horizontal axis shows droplet release height inside the channel. Effect of applied voltage on separation effectiveness is also shown. Applied voltage, V varies from 50 V to 100 V, frequency is 600 Hz.

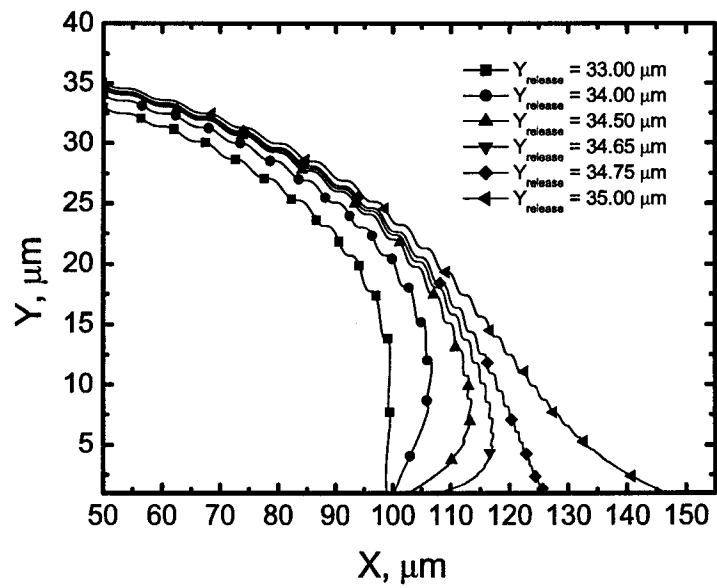


Figure 4.8: Trajectory of droplets released from a height range of 33 to 35 μm . Applied voltage, V is 50 V, frequency is 600 Hz.

Chapter 5

Dielectrophoresis in Membrane Fouling Prevention

During operation of membrane based processes, the efficiency of the system is adversely affected by accumulation of rejected solute particles on the membrane surface and within the membrane pores, which results in deterioration of permeate flux. This phenomenon is known as fouling of the membrane. Fouling is a critical factor in the life cycle of membrane based systems, and has been the major source of problem for continuous operation of these systems. Considerable attention has been devoted toward minimization and abatement of membrane fouling ever since the early days of commercial application of membrane based separations.

A majority of fouling control techniques is primarily geared toward creating disturbances in the flow field near the membrane, leading to removal of the accumulated particles from the membrane surface. Use of tangential flow is one of the primary means of controlling the extent of particle deposition on membranes. While significantly more effective than simple dead end filtration, particle deposition cannot be completely averted in simple crossflow filtration processes. Other means of creating disturbances in the hydrodynamic fields to minimize particle deposition on membranes include use of turbulence promoting spacers or inserts, use of flow geometries to promote near-membrane mixing through secondary flows like Dean vortices, pressure pulsing, and back flow

[Blanpain-Avet *et al.*, 1999, Hadzismajlovic and Bertram, 1998, Hong *et al.*, 2002, Kuberkar *et al.*, 1998, Mallubhotla *et al.*, 1998, Mikulasek *et al.*, 1997, Broussous *et al.*, 1998]. Numerous approaches based on chemical modification of the membranes to render these non-fouling have also been proposed [Carroll *et al.*, 2002, Grebenyuk *et al.*, 1998, Johansson *et al.*, 1998, Maartens *et al.*, 1998, Otaki *et al.*, 1998].

Over the past couple of decades, sporadic attempts of employing an electric field to reduce fouling have also been reported; techniques which are sometimes described under the terminology electro-filtration [Visvanathan and Benaim, 1989, Vonzumbusch *et al.*, 1998, Weigert *et al.*, 1999, Lee *et al.*, 2002, Yang *et al.*, 2002]. The inherent advantage of applying electric or other types of force fields (like ultrasonic fields) is to impede development of the fouling layer during the filtration process, as opposed to stopping the filtration operation intermittently for cleaning the membrane, which is generally the case in back-pulsing or flushing techniques.

In this chapter, a technique for reducing fouling of membranes is proposed, utilizing *dielectrophoresis* (DEP), which has been extensively utilized for manipulation, separation, and analysis of colloidal scale particles for several decades [Green and Morgan, 1997, Morgan and Green, 1997, Green and Morgan, 1998, Morgan *et al.*, 1999, Dussaud *et al.*, 2000, Gascoyne and Vykoukal, 2002, Pethig *et al.*, 1992]. These forces have also been used for fractionation of components of a cellular mixture [Green *et al.*, 2000b, Hughes, 2000, Heida *et al.*, 2002, Durr *et al.*, 2003, Holmes *et al.*, 2003].

As discussed in chapter 2, the basic principle underlying dielectrophoresis is the interaction of induced dipoles in colloidal entities with a spatially inhomogeneous electric field. Depending on the relative polarizations of the colloidal particles and the suspending medium, the interaction can give rise to attractive or repulsive forces on the particles. The particles are subjected to a repulsive DEP force field when they are less polarizable than the surrounding medium. In other words, when the dielectric constant of the suspended particles is smaller

than the dielectric constant of the suspending medium, the particles are repelled from regions of high electric field intensities. This phenomenon is called negative DEP. It is notable that in most aquatic colloidal dispersions, the dielectric constants of the particles are significantly smaller (less than 10) than the dielectric constant of water (about 80). Consequently, in an appropriately designed electrode array on a membrane that can generate regions of high field intensities near the membrane, the suspended particles in an aqueous medium will experience a repulsive force in the vicinity of the membrane. Although at present such membranes with an embedded array of microelectrodes do not exist, recent developments in microfabrication technology render it at least theoretically possible to fabricate such arrays of a conducting material on numerous ceramic and polymeric substrates.

5.1 System Description

The analysis in this chapter is based on a system very similar to the one used in chapter 4. Only the flowing suspension studied here is different; a system containing latex particles suspended in water is considered. The latex particles are assumed to behave as the colloidal particles in a typical membrane filtration system. The suspension in this study also flows through the membrane filtration channel that was described in the previous chapter. The properties of the two components of the suspension are listed in table A1 in the appendix.

The latex-in-water system in this case is subjected to a DEP force field that will repel the latex particles. The frequency of the applied voltage is selected based on the frequency dependent Clausius-Mossotti factor of the system. As discussed earlier, the nature of the DEP force can be different depending on the frequency of the applied voltage. Using the frequency spectrum in Figure 2.5, a high frequency was selected for the simulations in this chapter. When a feed suspension containing low dielectric colloidal particles suspended in an aqueous medium, flows through the channel, application of an ac signal to the

parallel microelectrode array embedded in the membrane, can create an appropriate repulsive (negative) DEP force field. Depending on the magnitude of this repulsive force, the target particles will levitate to a steady height from the membrane inside the channel. Eventually most of the particles of the target species will converge to a narrow region at a steady height above the membrane surface and will drift away with the flowing suspension. Theoretically, this novel technique can prevent almost all of the foulant particles from depositing on the membrane. A model has been developed to evaluate the feasibility of using this technique to reduce fouling and to determine relative importance of various control parameters in creating appropriate DEP force fields. This technique can dramatically increase the life of a membrane by reducing fouling.

5.2 Effect of Dielectrophoresis in Fouling Reduction

The effectiveness of coupled dielectrophoretic membrane filtration in reduction of membrane fouling has been explored based on the trajectory model developed in chapter 3. Relative influence of basic parameters, e.g. applied voltage and wall suction on the system has also been explored. The trajectory model in this case, tracks the particles in a repulsive force field as opposed to the attractive DEP forces in chapter 4. Table A1 lists the typical parameter values used for these simulations. The particles considered for these simulations are assumed to be less polarizable than the surrounding aqueous medium. The aqueous feed solution flows over the membrane surface embedded with electrode array, the electrodes being actuated by ac voltage. As before, the electrodes considered for these simulations are of equal width (W) and gap (G). The particle trajectory is constrained by a predefined channel length, beyond which the suspended particles are not subjected to DEP force.

The effect of uniform and non-uniform wall suction on the particle trajectories was discussed in chapter 3. It was pointed out that the particle trajectories

in an attractive DEP force field are not significantly affected by the variation of wall suction. The overpowering influence of the attractive DEP force reduced the effect of uniform and intermittent wall suction on the trajectories. However, the effect of wall suction is more noticeable when the particles are subjected to a repulsive force field, as shown in Figure 5.1. Figure 5.1 depicts two particle trajectories starting from the same initial position, under uniform and intermittent wall suction condition. As discussed before, particles experience less fluid drag in the transverse direction in case of intermittent wall suction. Compared to the uniform wall suction, this reduced drag condition allows the particles to be pushed away to a greater height inside the channel, under same negative DEP force field. Therefore, simulation results obtained by considering uniform wall suction actually provides the lower bound of the effectiveness of the fouling prevention technique. The simulation results in this chapter were obtained assuming uniform wall suction on the membrane surface.

The simulation results show significant effect of DEP force in fouling reduction by levitating the target species away from the membrane surface. Figures 5.2a and 5.2b show the trajectories of particles starting from different heights. These two trajectories illustrate the influence of wall suction velocity on the particle motion. As discussed earlier, particles initially starting from different heights converge to an equilibrium height depending on the force balance on each particle at a given location. As can be seen in Figure 5.2a and 5.2b, the transverse plane where the particles converge varies significantly with suction velocity. Higher value of wall suction naturally restricts the upward journey of the particles. Moreover, the axial location along the length of the channel, where majority of the particles reach the equilibrium height is significantly reduced due to increased wall suction. Therefore, wall suction can play an important role in determining the active channel length for this kind of application.

The equilibrium plane represents a transition zone where in this case the DEP force and hydrodynamic forces counterbalance each other. The effect of wall suction force in the transverse direction is usually more dominant than the

typical DEP force. Particles beyond the effective DEP field, follow a downward path due to suction until they start to experience the negative DEP force that pushes the particles upwards. The equilibrium height also depends on the magnitude of repulsive force exerted on the particles in the flowing medium. The negative DEP force, as in this case, is highly dependent on the applied voltage. Figure 5.3 shows the combined effect of applied ac voltage and wall suction velocity on the equilibrium height attained by the particles. Increase in applied voltage produces larger repulsive force, which is reflected as higher equilibrium height of the particles.

5.3 Implications on Membrane Fouling

To summarize, the simulations based on trajectory analysis indicate that negative DEP forces on a parallel electrode array embedded in a membrane can be effectively utilized to prevent colloidal fouling during crossflow filtration. Once the target species converge into a narrow zone above the membrane, they will drift away along the channel length due to the presence of cross flow of the feed solution. Under these conditions, the target species will eventually flow over the membrane surface without ever coming close enough to the membrane to deposit on the surface. Furthermore, the application of the high frequency ac fields will prevent phenomena like electrode polarization or other double layer type effects, as long as the electrodes do not short circuit. Preventing short circuits will also minimize several secondary electrical heating effects since there will be no current in the system. The application of relatively high voltages with negligible current will also ensure that the energy consumption associated with the DEP force field generation is negligible.

5.4 Summary

The combination of negative dielectrophoresis with crossflow membrane filtration can lead to an effective physical means for preventing membrane fouling

caused by deposition of colloids. The simulations for a model colloidal system indicate that the significant difference between the dielectric polarizabilities of suspended particles and the solvent can be utilized to prevent or minimize membrane fouling in an entirely physical manner, without significantly altering the chemistry of the membrane or the feed suspension. The application of the ac field is an added advantage in this respect, since the common complications encountered with ionic solutions in presence of dc fields, namely electrical double layer formation, electrolysis, or other thermal effects arising from current flow can be avoided.

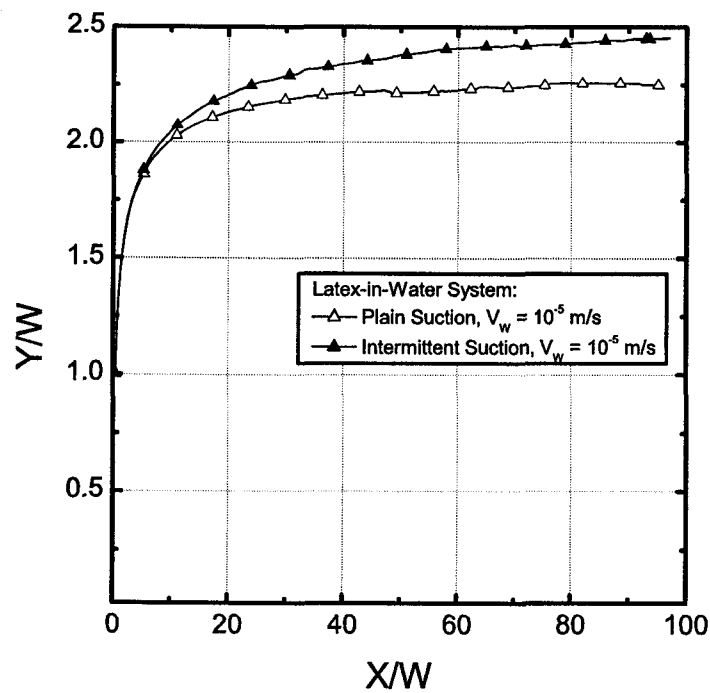
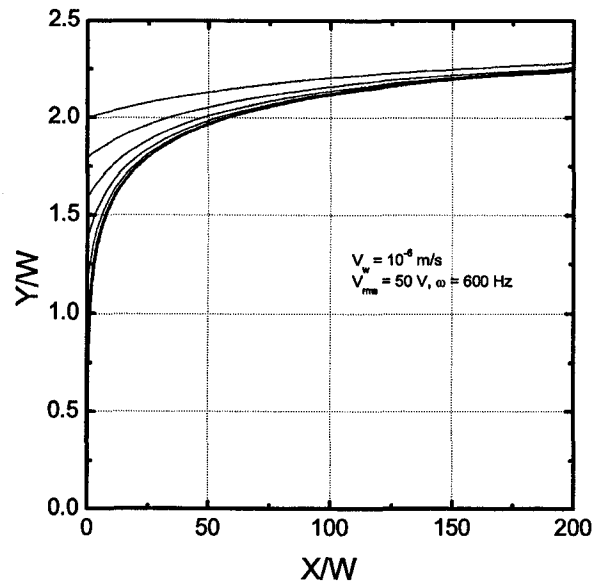
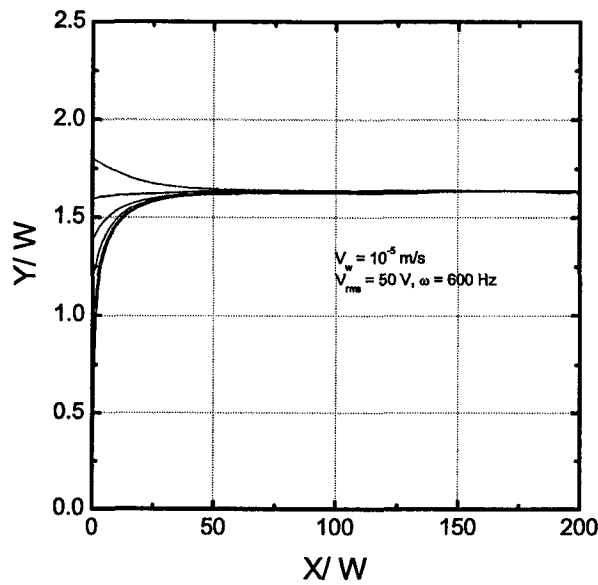


Figure 5.1: Trajectory of a particle in latex-in-water system under negative DEP, with uniform and intermittent wall suction. Both axes are nondimensionalized with respect to electrode width (W). The average crossflow velocity and maximum wall suction values are 10^{-3} m/s and 10^{-5} m/s, respectively. All other parameters are same as in table A1.



(a)



(b)

Figure 5.2: Trajectory of particles in latex-in-water system, released from different heights over the membrane surface. Both axes are nondimensionalized with respect to electrode width (W). (a) Uniform wall suction, $V_W = 10^{-6}$ m/s and average cross flow velocity is 10^{-3} m/s. (b) Uniform wall suction, $V_W = 10^{-5}$ m/s and average cross flow velocity is 10^{-3} m/s. All other parameters are given in table A1.

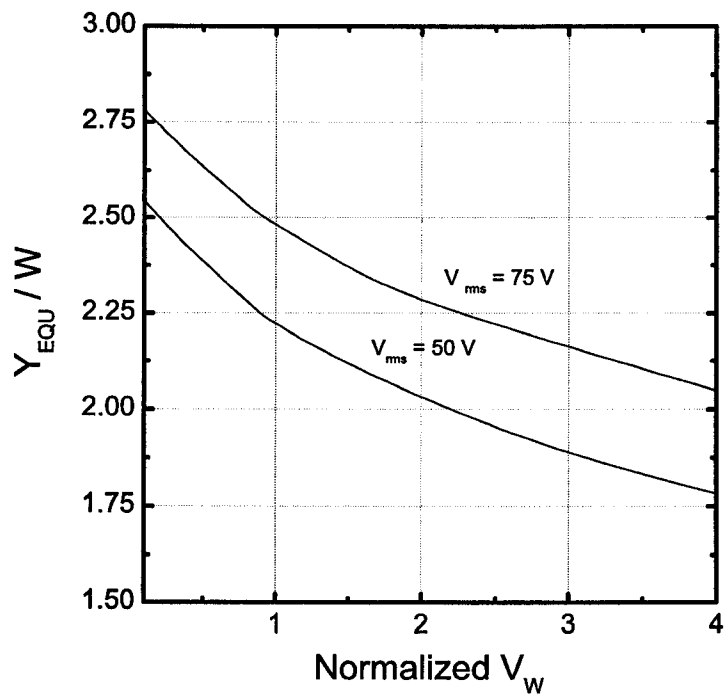


Figure 5.3: Effect of wall suction and applied voltage on equilibrium height attained by particles in the negative DEP force field. The horizontal and vertical axes are scaled with respect to wall suction, $V_w = 10^{-5} \text{ m/s}$ and electrode width (W), respectively. Uniform wall suction is considered in this case. All other parameters are same as in table A1.

Chapter 6

Experimental Observation

The dielectrophoretic membrane separation technique described in the previous chapters has significant potential as an effective separation technology in the oil industry. The theoretical studies performed in this work also predict successful fouling prevention in typical membrane filtration systems by employing DEP. However, the effectiveness of this technique and the accuracy of the theoretical model can be validated only through rigorous experimental work.

In this chapter, we describe a simple proof-of-concept experiment to assess the effectiveness of DEP forces in transporting colloidal entities in a crossflow field. The entire concept of dielectrophoretic membrane filtration hinges on the idea of embedding microelectrodes on the membrane surface. Even though recent advancements in microfabrication technology can produce micron size electrodes, it is not yet feasible to integrate these electrodes on a polymeric membrane surface. However, these microelectrode arrays can be manufactured on different types of surfaces, such as silicon wafer or glass substrate. Based on this, we developed a crossflow filtration cell analogue, where the membrane is replaced by an impermeable glass substrate coated with an electrode array. Experiments with this type of cell can potentially indicate the applicability of DEP in either attracting or repelling colloidal entities toward or away from the electrode bearing wall, respectively. Considerable amount of work needs to be done in order to find a manufacturing methodology to embed small scale

electrodes on the conventional membrane surface and to make this technology suitable for industrial scale applications.

6.1 Experimental Setup

6.1.1 Crossflow channel

The experimental setup consists of a cross flow channel, formed by two parallel glass slides. The bottom wall of the channel contains an array of microelectrodes connected to an external power supply unit (Wavetek, model 182A). The microelectrodes were manufactured on a glass substrate, using the microfabrication facility at the University of Alberta. The top wall is a simple microscope slide with two through holes drilled at the ends of the cell to provide flow inlet and outlet to the channel. The two slides were attached together, with a separation of 1 mm in between, to form a narrow channel. To maintain the separation and seal in the channel, a thin rectangular gasket of uniform thickness was glued to the inner surfaces of the two glass slides (along the edge of the two slides). This channel is assumed to be a close approximation of parallel-plate channels as discussed in the earlier chapters. The flow in the channel was maintained by connecting the inlet and outlet of the channel to a syringe pump through Tygon tubing (≈ 0.25 mm ID), to setup a closed system. The syringe pump (KDS120 push-pull syringe pump from Fisher Scientific) used with this system is capable of supplying a wide range of flow rates and can accommodate two syringes up to 10 ml size. The test cell was positioned under a microscope to observe the flow of various suspensions under an imposed electric field. A camera connected to the microscope allows the capture of real time video images of the events taking place inside the channel. Figure 6.1 shows the different components of the experimental setup.

6.1.2 Water-in-Heptane emulsion

The emulsion sample used in this experiment was prepared from deionized water (Millipore) and n-heptane (HPLC). The emulsion was stabilized by adding an emulsifier (Sorbitan monooleate, Span 80 from Fluka). Two different compositions of the sample were used, in both cases the total mass of the sample was 7 gm. In the first sample, the mass ratios of DI water, Span 80 and heptane were 5.10%, 0.54% and 94.36%, respectively. The mass ratios of DI water, Span 80 and heptane in the second composition were 4.96%, 2.25% and 92.78%, respectively. The masses of the components were measured by an analytical balance with a precision of 0.0001 gm. The emulsions were produced by applying vortex mixing for a duration of 3 minutes. The mean size of the water droplets suspended in the emulsion were around 10 μm . The samples were prepared by Dr. Geza Szabo and collected from Chemical and Materials Engineering department, University of Alberta.

6.2 Electrode Array Fabrication

A range of microfabrication techniques exists for the construction of electrode structures, but the principal method employed is that of photolithography. Photolithography uses an equivalent of photographic negative (photomask or mask) to expose a light-sensitive surface to produce a required pattern. The basic steps involved in the photolithographic process is summarized in Figure 6.2.

The interdigitated electrode array used in this experiment was fabricated at the NanoFab fabrication facility, University of Alberta. The array has a span of 5 cm with 300 parallel electrodes. The electrode width and the gap between two consecutive electrodes are both 50 μm . The consecutive parallel electrodes are alternatively connected to two different busbars that carry the electrical signal to the electrodes. At the end of the two busbars are two bonding pads for electrical connections to external power signal generator.

6.2.1 Mask preparation

The first step of the microfabrication process is to create a design of the electrode array which will be suitable for the standard substrates. The design of the array was completed using a commercial design software, L-Edit from Tanner Research, Inc., available at the NanoFab. The design output was in gds II format. The design was optimized for maximum utilization of the substrate area, therefore, two similar electrode arrays separated by a distance, were drawn on the design.

The electrode design was then transferred to the pattern generator (Heidelberg model DWL 200). Pattern was written on a 12.7 cm (5 in) square glass blank, with thin layers of chrome and photoresist on it. During the pattern generation, light or electron beam source exposes the resist. When the resist is developed and the chrome is etched away from the exposed areas, the desired pattern of the electrode array is left on the mask. The electrode structure on the mask is visible as thin lines of chrome.

6.2.2 Photolithography

The next step in the process is to transfer the pattern on the mask to a substrate. In this case, the intended electrode structure on the substrate (device) was similar to the chrome pattern on the mask. This type of mask transfer is known as *positive process*. The chrome-gold substrate (Figure 6.2a) used in this experiment was available from the NanoFab facility. The thin chrome layer improves the adherence of the gold layer (≈ 250 nm) to the glass substrate. The substrate was coated with a 1 μm thick layer of positive photoresist (HPR-504) by spin coating (Figure 6.2b). After the spin coating, the substrate was baked in the oven for 30 minutes at a temperature of 150° C.

The substrate with the layer of photoresist was mounted on a mask aligner (AB-M Contact Mask Aligner), to transfer the pattern from the mask to the substrate. The mask and the substrate need to be aligned perfectly for the accurate transfer of the design. Then the substrate was exposed for about 4

seconds and removed from the mask aligner (Figure 6.2c). The exposed substrate was treated with developer solution to remove the exposed photoresist. (Figure 6.2d and e)

To obtain the desired electrode structure on the glass substrate, the substrate was then etched with gold and chrome etch. Metals from the exposed areas were removed by this process and bare glass surface was left behind (Figure 6.2f). The substrate was then cleaned with IPO (iso propyl alcohol) and acetone to remove the residual photoresist. The glass substrate at this stage contained only the array of gold electrodes; with average electrode height of 300 nm (Figure 6.2g). The glass substrate was cut into two halves, to obtain two sets of identical electrode array. To make the array surface insulated, each electrode array was spin coated with very thin (400 nm) layer of PMMA (polymethyl methacrylate). Figure 6.3 shows a complete interdigitated electrode array ready to be connected to the experimental setup. A photograph of the final product is shown in Figure 6.3

6.3 Experimental Procedure

The experimental setup described in section 6.1 has been used to observe the behavior of water-in-heptane emulsion. This system is supposed to mimic the behavior of the system modelled in chapter 4. Furthermore, experimental study of this emulsion is possible under an optical microscope because of its transparency.

For each run of the experiment, 10 ml of the sample emulsion was dispensed from a syringe in the channel. Since the syringe pump was connected to a closed system, the emulsion gradually filled the channel and the collection syringe. Thus, a crossflow was developed inside the channel. The flow rate was set to 45 ml/hr to provide a low average crossflow velocity (10^{-3} m/s), restricted by low Reynolds number. The channel was first cleaned and then flushed with the emulsion to avoid contamination.

To observe the effect of the non-uniform electric field on the emulsion, the channel was placed on a microscope stage. The video camera attached to the microscope transferred the images from the microscope to a computer screen. The microscope objective was focused at the electrode plane, since depending on the nature of the DEP force, concentration of target species should either increase or diminish near the electrode plane. The electrode array at the bottom wall of the channel was connected to an external signal generator, to supply about 40 V at a frequency of 4 MHz. The signal generator was actuated when a fully developed flow was established inside the channel.

6.4 Observation

The standard electrical properties of the water droplets in the emulsion indicate that the water droplets have higher polarizations than the continuous medium (heptane). Therefore, at the frequency of the supplied voltage, the emulsion is expected to experience positive dielectrophoretic force.

The water droplets are clearly distinguishable under the microscope. The droplets were seen as spheres floating in the medium. Under typical crossflow condition, the water droplets at different heights over the electrode plane are carried away with the crossflow, at different velocities. The concentration of water droplets near the electrode plane was visibly low due to negligible influence of gravity. After the electrodes were actuated by the ac voltage, the water droplets near the electrode plane demonstrated a determined movement toward the electrode plane. As the droplets approached the surface, they moved toward the electrode edges where the electric field gradient was maximum. Interestingly, close to the electrode plane, the droplets coalesced to form larger shapes and then settled on the bottom wall. Figure 6.4 shows three images captured through the video camera at three sequential time frames. These images show the qualitative behavior of the water droplets inside the channel under DEP force. In Figure 6.4a, the water droplets can be seen floating by the

electrode array and surrounded by surfactant. After only 0.2 sec, the droplet accumulation near the surface is visible. The droplets are clearly attracted toward the electrode edges and are adhering to the surface. Figure 6.4c shows larger droplets at the same locations on the electrode array after 1 sec. The time scale of these images corroborate the simulation results for trajectory analysis in chapter 4, where it was suggested that dielectrophoresis is an expeditious process.

The concentration of water droplets near the electrode plane increased significantly under the action of positive DEP force. This is indicative of the potential of DEP force in separating components from a mixture. However, the DEP force field did not affect the droplets far away from the electrode plane which was anticipated from the model predictions. The observations made during this experiment are in agreement with the theoretical prediction.

In this experiment, it was assumed that there was no free charges in the emulsion flowing through the filtration cell. However, some of the observations recorded during the experiment were similar to the characteristics of charged entities in an alternating electric field. It was observed that at low frequencies, some of the microscopic droplets near the electrode edges demonstrated an oscillatory motion about their mean position, similar to the behavior of charged particles in an ac electric field. The droplets continuously moved back and forth near the electrode edges. Therefore, it is possible that the water droplets suspended in the water-in-oil emulsion acquired surface charges. Furthermore, the effect of modification of local electric field distribution around the droplets were also observed during the experiment. As described in chapter 2, the distortion of the local electric field around two polarized droplets in close proximity gave rise to dipole-dipole interaction, which resulted in the formation of long strings of droplets. This is commonly known as *pearl chaining*.

6.5 Relation to Model Prediction

The experimental observations in this experiment were only qualitative in nature. The objective of this experiment was to study the DEP effect in a system that closely resembles the model discussed in chapter 4. As mentioned before, the membrane filtration component of the model is not present in this setup and an appropriate experimental setup is necessary to quantify the collection efficiency of the proposed dielectrophoretic membrane filtration system. However, the qualitative observations made in this experiment support the simulation results. For instance, the water droplets with higher polarizations were seen to experience an attractive force inside the channel and were pulled towards the regions of highest field gradient even in the presence of a tangential flow. These observations are similar to the simulation results obtained for impermeable wall channel. The effect of higher applied voltage was also noticed during the experiment.

6.6 Summary

A simple experiment was performed to explore the influence of DEP force on water-in-oil emulsion. Microfabrication of an interdigitated planar electrode array and fabrication of a crossflow filtration cell analogue have been discussed in this chapter. The experimental observations indicate that attractive (positive) DEP forces are significant enough to preferentially attract water droplets from the emulsion, even in the presence of a tangential flow. The droplets tend to coalesce as they impinge on the electrodes and form larger pools of water. As long as the voltage is maintained on the electrodes, the droplets remain attached to the electrode, with higher concentration near the electrode edges. These observations are in qualitative conformity with the theoretical results obtained in chapter 4.

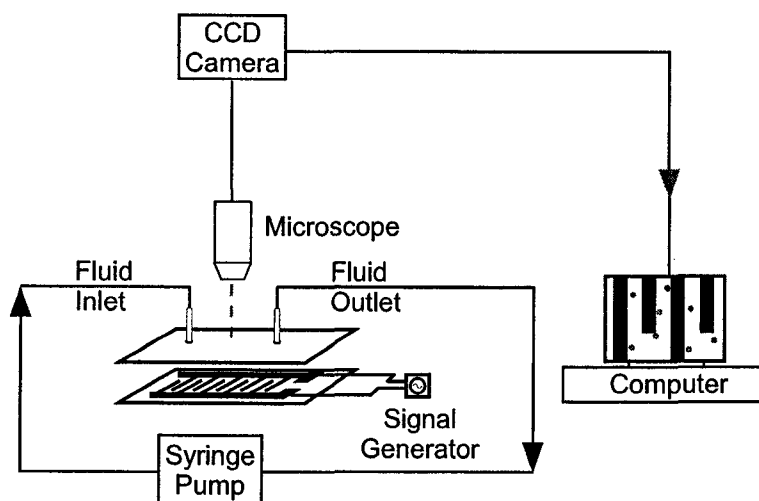


Figure 6.1: Schematic representation of the experimental setup, showing different components of the system.

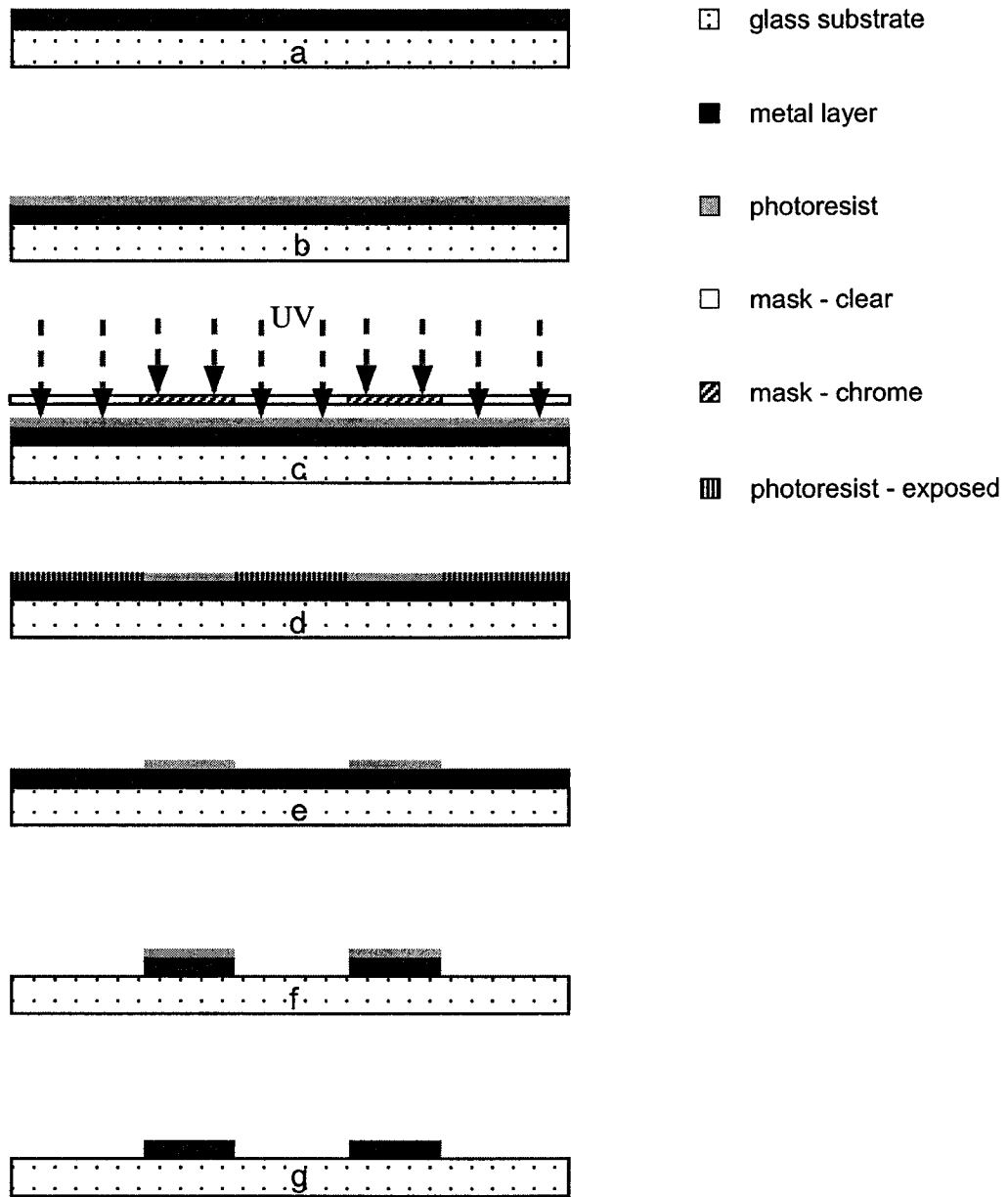


Figure 6.2: Steps involved in microfabrication of the interdigitated electrode array.

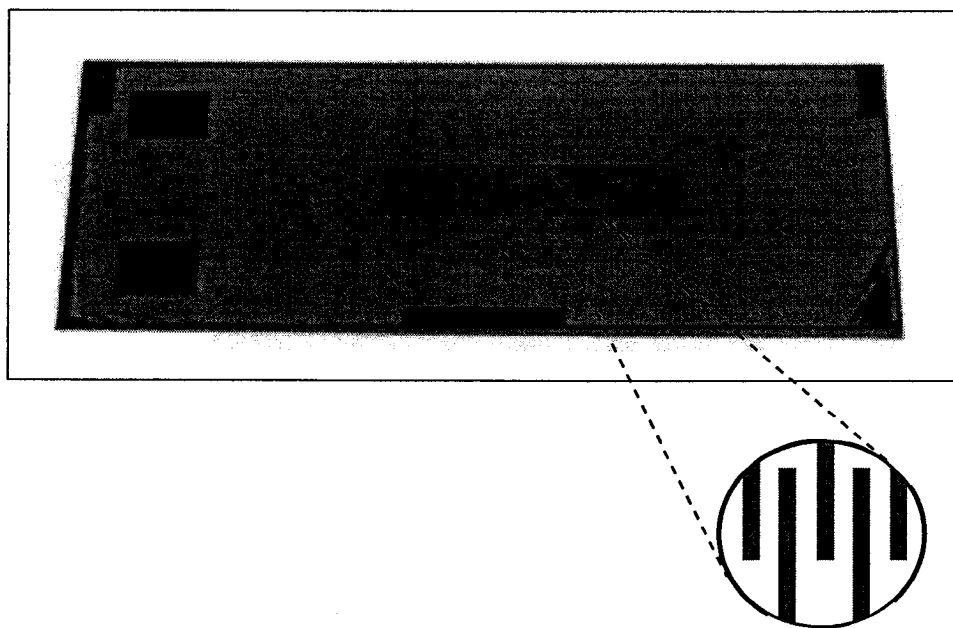


Figure 6.3: Image of the microfabricated electrode array with a closeup view of the parallel electrodes.



(a)



(b)



(c)

Figure 6.4: Video images of water droplet movement inside the crossflow channel. The water droplets are subjected to positive DEP force. The three images correspond to three sequential time frames, $t = 0, 0.2$ and 1 sec.

Chapter 7

Conclusion and Future Work

7.1 Concluding Remarks

A novel technique based on simultaneous ac dielectrophoresis on a parallel electrode array and membrane filtration is proposed in this work. Based on the literature review, a number of publications were found to use dielectrophoresis for manipulation, separation and characterization of microscale bodies and biological entities. However, the potential of coupling dielectrophoresis with membrane filtration to enhance the separation process seems to be unexplored. Through this work, it has been demonstrated that a coupled separation process can be highly efficient for removal of water droplets from water-in-oil emulsion. At the same time, such a separation process can lead to an effective means for preventing membrane fouling.

The major conclusions drawn from the study of transport of colloidal entities in a crossflow membrane filtration system, under the influence of dielectrophoretic forces, are summarized below:

1. The DEP force produced inside the coupled dielectrophoretic membrane filtration system, is a microscale phenomenon and is remarkably efficient in removing trace amounts of water droplets from a dilute water-in-decane emulsion.
2. The frequency dependent nature of DEP force can be utilized, to create

repulsive DEP force inside the filtration system in order to prevent fouling of the membrane by deposition of colloidal entities.

3. Analytical solution of the electric field distribution is available for simple electrode geometry only. However, the numerical approach described here can be expanded to account for any arbitrary shape of the electrodes in the array, to provide a realistic estimation of the DEP force.
4. The fluid flow during the crossflow membrane separation process can significantly alter particle trajectories in the absence of other forces. However, the influence of hydrodynamic forces diminish due to the overpowering effect of the DEP forces, when incorporated in the system.
5. The model assumption of uniform wall suction on the membrane containing an array of electrodes, is not realistic. To address this, the flow field in presence of intermittent suction was also modelled. However, it has been shown that the uniform wall suction assumption is simple to implement and produces remarkably accurate particle trajectories under attractive DEP forces.
6. The simulation results could not be compared against any standard result, since current study is the first of this kind. The overall concept was qualitatively examined through a small scale experiment. The behavior of the water droplets in a water-in-heptane emulsion was observed in an impermeable wall channel. The predictions from the model were supported by the experimental observations.

7.2 Future Work

The study reported here should be regarded as the initial step of a thorough investigation. Here, the concept of dielectrophoretic membrane filtration is explored in a simplistic manner, to evaluate the potential such a technology. Considerable number of simplifications have been imposed on the model developed

in this study. However, the simplifications may not be justified if a generalized framework is to be developed. Some of the significant recommendations are listed below:

1. At the core of the development of a coupled separation process is the idea of embedded microelectrodes which is used to create the dielectrophoretic force field inside the membrane filtration system. However, during the current study, available microfabrication techniques could not produce a long stretch of membrane surface embedded with microscale electrodes. Rigorous experimental studies should be undertaken to determine a feasible means of integrating the electrode array on the porous membrane surface.
2. The dielectrophoretic force generated by parallel electrode array is considered in this study because of the uncomplicated nature of the parallel electrode geometry. Moreover, analytical solution is available for the interdigitated electrode geometry which facilitated the validation of the numerical formulation. The generalized numerical scheme discussed in this study can be employed to evaluate DEP forces produced by more complicated electrode geometries.
3. The particle transport model developed here is based on a single particle trajectory analysis and the colloidal entities were assumed to be non-interacting and non-Brownian. This model is sufficient to study dilute systems with micron sized particles. However, a concentration based model would be more appropriate and relevant to real world applications. Furthermore, this model does not account for the diffusive flux in the filtration process, which can be significant in some cases. Therefore, a model should be developed using convection-diffusion equation.
4. The electrothermal effects were neglected during the analysis of the fluid flow inside the channel. Electric field induced fluid motion can play a sig-

nificant role in many large scale operations. Therefore, the model should be modified to account for the effect of electric field on the flowing medium.

5. The electric field distribution around the suspended particles are modified due to the presence of the particles. The modified local electric fields often trigger particle-particle interaction; which was seen during the experimental observations. This phenomena can be important in the separation process and the model should be general enough to consider interparticle interactions. It should also be noted that the basic theory of dielectrophoresis used in this work is based on dipole approximation; which holds in the majority of cases. However, under certain circumstances, a more rigorous formulation considering higher order terms (multipoles), may be necessary.
6. Finally, extensive experimental investigation is necessary to explore the potential of this novel technique and it's scalability to commercially viable applications.

Bibliography

- Abidor, I. G. and A. E. Sowers (1992). Kinetics and mechanism of cell-membrane electrofusion. *Biophysical Journal* **61**(6), 1557–1569.
- Bakewell, D. J. and H. Morgan (2001). Measuring the frequency dependent polarizability of colloidal particles from dielectrophoretic collection data. *Ieee Transactions on Dielectrics and Electrical Insulation* **8**(3), 566–571.
- Blanpain-Avet, P., N. Doubrovine, C. Lafforgue and M. Lalande (1999). The effect of oscillatory flow on crossflow microfiltration of beer in a tubular mineral membrane system - membrane fouling resistance decrease and energetic considerations. *Journal of Membrane Science* **152**(2), 151–174.
- Broussous, L., J. C. Ruiz, A. Larbot and L. Cot (1998). Stamped ceramic porous tubes for tangential filtration. *Separation and Purification Technology* **14**(1-3), 53–57.
- Carroll, T., N. A. Booker and J. Meier-Haack (2002). Polyelectrolyte-grafted microfiltration membranes to control fouling by natural organic matter in drinking water. *Journal of Membrane Science* **203**(1-2), 3–13.
- Castellanos, A. (1998). *Electrohydrodynamics*. Springer, New York.
- Clague, D. S. and E. K. Wheeler (2001). Dielectrophoretic manipulation of macromolecules: The electric field. *Physical Review E* **64**02(2), art. no.-026605.
- Cui, L., T. Zhang and H. Morgan (2002). Optical particle detection integrated in a dielectrophoretic lab-on-a-chip. *Journal of Micromechanics and Microengineering* **12**(1), 7–12.

- Durr, M., J. Kentsch, T. Müller, T. Schnelle and M. Stelzle (2003). Microdevices for manipulation and accumulation of micro- and nanoparticles by dielectrophoresis. *Electrophoresis* **24**(4), 722–731.
- Dussaud, A. D., B. Khusid and A. Acrivos (2000). Particle segregation in suspensions subject to high-gradient ac electric fields. *Journal of Applied Physics* **88**(9), 5463–5473.
- Eaton, P.E. (2000). Hydrolysis of metal salts in synthetic crude oil. In: *AIChE Spring Conference*. Vol. 61c. Houston TX.
- Elimelech, M., X. Jia, J. Gregory and R. Williams (1995). *Particle Deposition and Aggregation: Measurement, Modelling and Simulation*. Butterworth-Heinemann.
- Eow, J. S., M. Ghadiri, A. O. Sharif and T. J. Williams (2001). Electrostatic enhancement of coalescence of water droplets in oil: a review of the current understanding. *Chemical Engineering Journal* **84**(3), 173–619.
- Fuhr, G. and S. G. Shirley (1995). Cell handling and characterization using micron and submicron electrode arrays - state-of-the-art and perspectives of semiconductor microtools. *Journal of Micromechanics and Microengineering* **5**(2), 77–85.
- Fuhr, G., H. Glasser, T. Müller and T. Schnelle (1994). Cell manipulation and cultivation under ac electric-field influence in highly conductive culture media. *Biochimica Et Biophysica Acta-General Subjects* **1201**(3), 353–360.
- Fuhr, G., R. Hagedorn, T. Müller, W. Benecke, B. Wagner and J. Gimsa (1991). Asynchronous traveling-wave induced linear motion of living cells. *Studia Biophysica* **140**(2), 79–102.
- Gascoyne, P. R. C. and J. Vykoukal (2002). Particle separation by dielectrophoresis. *Electrophoresis* **23**(13), 1973–1983.
- Gascoyne, P. R. C., J. Noshari, F. F. Becker and R. Pethig (1994). Use of dielectrophoretic collection spectra for characterizing differences between normal and cancerous cells. *Ieee Transactions on Industry Applications* **30**(4), 829–834.

- Gascoyne, P. R. C., R. Pethig, J. P. H. Burt and F. F. Becker (1993). Membrane-changes accompanying the induced-differentiation of friend murine erythroleukemia-cells studied by dielectrophoresis. *Biochimica Et Biophysica Acta* **1149**(1), 119–126.
- Gascoyne, P. R. C., Y. Huang, R. Pethig, J. Vykoukal and F. F. Becker (1992). Dielectrophoretic separation of mammalian-cells studied by computerized image-analysis. *Measurement Science and Technology* **3**(5), 439–445.
- Gonzalez, A., A. Ramos, N. G. Green, A. Castellanos and H. Morgan (2000). Fluid flow induced by nonuniform ac electric fields in electrolytes on micro-electrodes. ii. a linear double-layer analysis. *Physical Review E* **61**(4), 4019–4028.
- Grebenyuk, V. D., R. D. Chebotareva, S. Peters and V. Linkov (1998). Surface modification of anion-exchange electro dialysis membranes to enhance anti-fouling characteristics. *Desalination* **115**(3), 313–329.
- Green, N. G., A. Ramos, A. Gonzalez, H. Morgan and A. Castellanos (2000a). Fluid flow induced by nonuniform ac electric fields in electrolytes on micro-electrodes. i. experimental measurements. *Physical Review E* **61**(4), 4011–4018.
- Green, N. G., A. Ramos, A. Gonzalez, H. Morgan and A. Castellanos (2002a). Fluid flow induced by nonuniform ac electric fields in electrolytes on micro-electrodes. iii. observation of streamlines and numerical simulation. *Physical Review E*.
- Green, N. G., A. Ramos and H. Morgan (2000b). Ac electrokinetics: a survey of sub-micrometre particle dynamics. *Journal of Physics D-Applied Physics* **33**(6), 632–641.
- Green, N. G., A. Ramos and H. Morgan (2002b). Numerical solution of the dielectrophoretic and travelling wave forces for interdigitated electrode arrays using the finite element method. *Journal of Electrostatics* **56**(2), 235–254.
- Green, N. G. and H. Morgan (1997). Dielectrophoretic separation of nanoparticles. *Journal of Physics D-Applied Physics* **30**(11), L41–L44.

- Green, N. G. and H. Morgan (1998). Separation of submicrometre particles using a combination of dielectrophoretic and electrohydrodynamic forces. *Journal of Physics D-Applied Physics* **31**(7), L25–L30.
- Green, N. G., H. Morgan and J. J. Milner (1997). Manipulation and trapping of sub-micron bioparticles using dielectrophoresis. *Journal of Biochemical and Biophysical Methods* **35**(2), 89–102.
- Hadzismajlovic, D. E. and C. D. Bertram (1998). Flux enhancement in laminar crossflow microfiltration using a collapsible-tube pulsation generator. *Journal of Membrane Science* **142**(2), 173–189.
- Hagedorn, R., G. Fuhr, T. Muller and J. Gimsa (1992). Traveling-wave dielectrophoresis of microparticles. *Electrophoresis* **13**(1-2), 49–54.
- Hatschek, E. and P. C. L. Thorne (1923). Metal sols in non-dissociating liquids. i. nickel in toluene and benzene. *Proceedings of the Royal Society of London* **103**(721), 276–284.
- Heida, T., W. L. C. Rutten and E. Marani (2002). Understanding dielectrophoretic trapping of neuronal cells: modelling electric field, electrode-liquid interface and fluid flow. *Journal of Physics D-Applied Physics* **35**(13), 1592–1602.
- Hiemenz, P. C. (1986). *Principles of Colloid and Surface Chemistry*. Marcel Dekker. New York.
- Holmes, D., N. G. Green and H. Morgan (2003). Microdevices for dielectrophoretic flow-through cell separation. *Ieee Engineering in Medicine and Biology Magazine* **22**(6), 85–90.
- Hong, A. C., A. G. Fane and R. P. Burford (2002). The effects of intermittent permeate flow and crossflow on membrane coalescence of oil-in-water emulsions. *Desalination* **144**(1-3), 185–191.
- Huang, Y. and R. Pethig (1991). Electrode design for negative dielectrophoresis. *Measurement Science and Technology* **2**(12), 1142–1146.
- Huang, Y., J. M. Yang, P. J. Hopkins, S. Kassegne, M. Tirado, A. H. Forster and H. Reese (2003). Separation of simulants of biological warfare agents from

- blood by a miniaturized dielectrophoresis device. *Biomedical Microdevices* **5**(3), 217–225.
- Hughes, M. P. (2000). Ac electrokinetics: applications for nanotechnology. *Nanotechnology* **11**(2), 124–132.
- Hughes, M. P. (2002). *Nanoelectromechanics in Engineering and Biology*. CRC Press. New York.
- Hughes, M. P., H. Morgan and F. J. Rixon (2001). Dielectrophoretic manipulation and characterization of herpes simplex virus-1 capsids. *European Biophysics Journal with Biophysics Letters* **30**(4), 268–272.
- Hughes, M. P., H. Morgan, F. J. Rixon, J. P. H. Burt and R. Pethig (1998). Manipulation of herpes simplex virus type 1 by dielectrophoresis. *Biochimica Et Biophysica Acta-General Subjects* **1425**(1), 119–126.
- Johansson, J., H. K. Yasuda and R. K. Bajpai (1998). Fouling and protein adsorption - effect of low-temperature plasma treatment of membrane surfaces. *Applied Biochemistry and Biotechnology* **70-2**, 747–763.
- Jones, T. B. (1985). Multipole corrections to dielectrophoretic force. *Ieee Transactions on Industry Applications* **21**(4), 930–934.
- Jones, T. B. (1995). *Electromechanics of Particles*. Cambridge Univ. Press. Cambridge.
- Kaler, K. V. I. S. and T. B. Jones (1990). Dielectrophoretic spectra of single cells determined by feedback-controlled levitation. *Biophysical Journal* **57**(2), 173–182.
- Kleinstreuer, C. and M.S. Paller (1983). Laminar dilute suspension flow in plate and frame ultrafiltration units. *AIChE J.* **29**(4), 529–533.
- Kuberkar, V., P. Czekaj and R. Davis (1998). Flux enhancement for membrane filtration of bacterial suspensions using high-frequency backpulsing. *Biotechnology and Bioengineering* **60**(1), 77–87.
- Langevin, P. (1908). A theory of brownian motion. *C. R. Acad. Sci.* **146**, 530–533.

- Lee, H. J., S. H. Moon and S. P. Tsai (2002). Effects of pulsed electric fields on membrane fouling in electro dialysis of nacl solution containing humate. *Separation and Purification Technology* **27**(2), 89–95.
- Maartens, A., P. Swart and E. P. Jacobs (1998). Enzymatic cleaning of ultrafiltration membranes fouled in wool-scouring effluent. *Water SA* **24**(1), 71–76.
- Mallubhotla, H., S. Hoffmann, M. Schmidt, J. Vente and G. Belfort (1998). Flux enhancement during dean vortex tubular membrane nanofiltration - 10 - design, construction, and system characterization. *Journal of Membrane Science* **141**(2), 183–195.
- Markx, G. H. and R. Pethig (1995). Dielectrophoretic separation of cells - continuous separation. *Biotechnology and Bioengineering* **45**(4), 337–343.
- Markx, G. H., J. Rousselet and R. Pethig (1997a). Dep-fff: Field-flow fractionation using non-uniform electric fields. *Journal of Liquid Chromatography and Related Technologies* **20**(16-17), 2857–2872.
- Markx, G. H., R. Pethig and J. Rousselet (1997b). The dielectrophoretic levitation of latex beads, with reference to field-flow fractionation. *Journal of Physics D-Applied Physics* **30**(17), 2470–2477.
- Markx, G. H., Y. Huang, X. F. Zhou and R. Pethig (1994). Dielectrophoretic characterization and separation of microorganisms. *Microbiology-Uk* **140**, 585–591.
- Masliyah, J. (1994). *Electrokinetic Transport Phenomena*. Alberta Oil Sands Technology and Research Authority.
- Mikulasek, P., J. Cakl and Z. Petras (1997). Ceramic cross-flow microfiltration in the presence of inserts. *Collection of Czechoslovak Chemical Communications* **62**(12), 1879–1887.
- Morgan, H., A. G. Izquierdo, D. Bakewell, N. G. Green and A. Ramos (2001a). The dielectrophoretic and travelling wave forces generated by interdigitated electrode arrays: analytical solution using fourier series. *Journal of Physics D-Applied Physics* **34**(10), 1553–1561.

- Morgan, H., A. G. Izquierdo, D. Bakewell, N. G. Green and A. Ramos (2001b). The dielectrophoretic and travelling wave forces generated by interdigitated electrode arrays: analytical solution using fourier series (vol 34, pg 1553, 2001). *Journal of Physics D-Applied Physics* **34**(17), 2708–2708.
- Morgan, H. and N. G. Green (1997). Dielectrophoretic manipulation of rod-shaped viral particles. *Journal of Electrostatics* **42**(3), 279–293.
- Morgan, H. and N. G. Green (2002). *AC Electrokinesis: colloids and nanoparticles*. Research Studies Press Ltd.
- Morgan, H., M. P. Hughes and N. G. Green (1999). Separation of submicron bioparticles by dielectrophoresis. *Biophysical Journal* **77**(1), 516–525.
- Mulder, M. (1996). *Basic Principles of Membrane Technology*. Kluwer Academic.
- Otaki, M., S. Takizawa and S. Ohgaki (1998). Control and modeling of membrane fouling due to microorganism growth by uv pretreatment. *Water Science and Technology* **38**(4-5), 405–412.
- Pethig, R., Y. Huang, X. B. Wang and J. P. H. Burt (1992). Positive and negative dielectrophoretic collection of colloidal particles using interdigitated castellated microelectrodes. *Journal of Physics D-Applied Physics* **25**(5), 881–888.
- Pohl, H. A. (1951). The motion and precipitation of suspensoids in divergent electric fields. *Journal of Applied Physics* **22**(7), 869–871.
- Pohl, H. A. (1978). *Dielectrophoresis*. Cambridge Univ. Press. Cambridge.
- Ramos, A., H. Morgan, N. G. Green and A. Castellanos (1998). Ac electrokinetics: a review of forces in microelectrode structures. *Journal of Physics D-Applied Physics* **31**(18), 2338–2353.
- Russel, W. B., Saville D. A. and W. R. Schowalter (1995). *Colloidal Dispersions*. Cambridge University Press.
- Shapiro, M., A. L. Shalom and I. J. Lin (1985). Dielectric flocculation of non-diffusive particles in a nonconducting fluid and a uniform electric field. *Journal of Applied Physics* **58**(2), 1028–1031.

- Suehiro, J., G. B. Zhou, M. Imamura and M. Hara (2003). Dielectrophoretic filter for separation and recovery of biological cells in water. *Ieee Transactions on Industry Applications* **39**(5), 1514–1521.
- Tritton, D. J. (1988). *Physical Fluid Dynamics*. Oxford University Press.
- Visvanathan, C. and R. Benaim (1989). Application of an electric-field for the reduction of particle and colloidal membrane fouling in cross-flow microfiltration. *Separation Science and Technology* **24**(5-6), 383–398.
- Vonzumbusch, P., W. Kulcke and G. Brunner (1998). Use of alternating electrical fields as anti-fouling strategy in ultrafiltration of biological suspensions - introduction of a new experimental procedure for crossflow filtration. *Journal of Membrane Science* **142**(1), 75–86.
- Wallace, D., B. Kadatz, R. Tipman and S. Snaychuk (2001). Conard extraction fundamentals and process affected water workshop.
- Wang, X. B., Y. Huang, J. P. H. Burt, G. H. Markx and R. Pethig (1993). Selective dielectrophoretic confinement of bioparticles in potential-energy wells. *Journal of Physics D-Applied Physics* **26**(8), 1278–1285.
- Wang, X. B., Y. Huang, P. R. C. Gascoyne, F. F. Becker, R. Holzel and R. Pethig (1994). Changes in friend murine erythroleukemia cell-membranes during induced-differentiation determined by electrorotation. *Biochimica Et Biophysica Acta-Biomembranes* **1193**(2), 330–344.
- Wang, X. J., X. B. Wang and P. R. C. Gascoyne (1997). General expressions for dielectrophoretic force and electrorotational torque derived using the maxwell stress tensor method. *Journal of Electrostatics* **39**(4), 277–295.
- Wang, X. J., X. B. Wang, F. F. Becker and P. R. C. Gascoyne (1996). A theoretical method of electrical field analysis for dielectrophoretic electrode arrays using green's theorem. *Journal of Physics D-Applied Physics* **29**(6), 1649–1660.
- Washizu, M. and T. B. Jones (1994). Multipolar dielectrophoretic force calculation. *Journal of Electrostatics* **33**(2), 187–198.

- Weigert, T., J. Altmann and S. Ripperger (1999). Crossflow electrofiltration in pilot scale. *Journal of Membrane Science* **159**(1-2), 253–262.
- Xu, Y., T. Dabros, H. Hamza and W. Shefantook (1999). Destabilization of water in bitumen emulsion by washing with water. *Petroleum Science and Technology* **17**(9-10), 1051–1070.
- Yang, G. C. C., T. Y. Yang and S. H. Tsai (2002). A preliminary study on electrically enhanced crossflow microfiltration of cmp (chemical-mechanical polishing) wastewater. *Water Science and Technology* **46**(11-12), 171–176.
- Yang, J., Y. Huang, X. B. Wang, F. F. Becker and P. R. C. Gascoyne (1999). Cell separation on microfabricated electrodes using dielectrophoretic/gravitational field flow fractionation. *Analytical Chemistry* **71**(5), 911–918.
- Zienkiewicz, O. C., Taylor R. L. (2000). *The Finite Element Method*. McGraw-Hill. London.
- Zimmermann, U. and J. Vienken (1982). Electric field-induced cell-to-cell fusion. *Journal of Membrane Biology* **67**(3), 165–182.

Appendix A

Table 1: Physical and chemical properties of latex-in-water system

Property	Value
Physical Properties	
Particle radius	1-2 μ m
Density of Water	1000 kg/m ³
Sp. gravity of latex	\approx 1
Viscosity of water	1.0×10^{-3} N.s/m ²
Temperature	298 K
Boltzmann constant	1.38×10^{-23} J/K
Electrical Properties	
Electrode width	50 μ m
Electrode pitch	100 μ m
RMS voltage	50 - 75 V
Frequency	10 - 600 Hz
Conductivity of Water	5.0×10^{-8} S/m
Relative Permittivity of Water	78-80
Conductivity of latex	1.0×10^{-7} S/m
Relative Permittivity of latex	2 - 3
Channel dimensions	
Channel length	10 mm
Channel height	0.1 - 2 mm
Volumetric Flow Rate	1 - 6 ml/min
Suction Velocity	1×10^{-6} 6×10^{-5} m/s

Table 2: Physical and chemical properties of water-in-decane system

Property	Value
Physical Properties	
Droplet radius	1-2 μ m
Density of Water	1000 kg/m ³
Sp. gravity of decane	\approx 1
Viscosity of Decane	1.0×10^{-3} N.s/m ²
Temperature	298 K
Boltzmann constant	1.38×10^{-23} J/K
Electrical Properties	
Electrode width	20 - 75 μ m
Electrode pitch	100 μ m
RMS voltage	50 - 250 V
Frequency	600 - 2000 Hz
Conductivity of Water	5.0×10^{-8} S/m
Relative Permittivity of Water	78-80
Conductivity of Decane	1.0×10^{-10} S/m
Relative Permittivity of Decane	5 - 6
Channel dimensions	
Channel length	10 mm
Channel height	0.1 - 2 mm
Volumetric Flow Rate	1 - 6 ml/min
Suction Velocity	1×10^{-6} 6×10^{-5} m/s